Harlov, D. E., Dunkley, D. J., Hansen, E. C., Ishwar-Kumar, C., Samuel, V., Hokada, T. (2022): Zircon as a Recorder of Trace Element Changes during High-Grade Metamorphism of Neoarchean Lower Crust, Shevaroy Block, Eastern Dharwar Craton, India. - Journal of Petrology, 63, 5, 1-44.

https://doi.org/10.1093/petrology/egac036

Zircon as a recorder of trace element changes during high-grade metamorphism of Neoarchean lower crust, Shevaroy Block, Eastern Dharwar Craton, India

DANIEL E. HARLOV[1,2,3*], DANIEL J. DUNKLEY[4], EDWARD C. HANSEN[5], C. ISHWAR-KUMAR[6], VINOD SAMUEL[7], and TOMOKAZU HOKADA[8]

[1]Deutches GeoForschungsZentrum GFZ, Telegrafenberg, D-14473 Potsdam, Germany

[2]Department of Geology, University of Johannesburg P.O. Box 524, Auckland Park, 2006 South Africa

[3]Faculty of Earth Resources, China University of Geosciences, 430074 Wuhan, China

[4]Central Geophysical Observatory, Osiedle PAN 1, 05622 Belsk Duzy, Poland

[5]Department of Geology, Hope College, Holland, Michigan 49422-9000, USA

[6]Department of Earth Sciences, Indian Institute of Technology Kanpur, Kanpur 208016, India

[7]Department of Earth System Sciences, Yonsei University, Seoul 03722, Republic of Korea

[8]National Institute of Polar Research (NIPR), 3-10 Midori-cho, Tachikawa-shi, Tokyo-to, 190-8518 Japan

*Corresponding author. Email: dharlov@gfz-potsdam.de

ABSTRACT

Systematic changes in whole-rock chemistry, mineralogy, mineral textures, and mineral chemistry, are seen along a ca. 95 km traverse of late Archean granitoid orthogneisses in the Shevaroy Block, Eastern Dharwar Craton, southern India. The traverse passes from amphibolite-grade gneisses in the north to granulite-grade rocks (charnockite) in the south. Changes include whole-rock depletion of

Rb, Cs, Th, and U in the granulite grade rocks as relative to the amphibolite grade gneisses, and oxidation trends regionally from highly oxidized granulite-facies rocks near the magnetite-hematite buffer to relatively reduced amphibolite-facies rocks below the fayalite-magnetite-quartz. Rare earth elements show limited mobility and are hosted a variety of minerals whose presence is dependent on the metamorphic grade ranging from titanite and allanite in the amphibolite-facies rocks to monazite in the vicinity of the orthopyroxene-in isograd to apatite in the granulite-facies charnockite.

Cathodoluminesence (CL) and back scattered electron (BSE) sub-grain imaging and Sensitive High-Resolution Ion MicroProbe (SHRIMP) analysis of zircon from 29 samples of dioritic, tonalitic, and granitic orthogneiss from the traverse reveals magmatic zircon cores that record the emplacement of the granitoid protoliths mostly about 2580 to 2550 Ma, along with a few older mid to late Archean tonalites. Protolith zircon was modified during metamorphism by overgrowth and/or replacement. Relative to igneous cores, U-enriched metamorphic zircon, dominant in the amphibolite-grade gneisses, formed at ca. 2530 Ma, predating retrograde titanite growth at ca. 2500 Ma. Uranium-depleted mantles grew on zircon between 2530 and 2500 Ma in granulite-grade samples south of the orthopyroxene-in isograd. In some of these samples, the U-depleted metamorphic zircon is preceded by mantles of U-undepleted zircon, indicating a progression of metamorphic zircon growth with increasing depleted compositions between 2530 and 2500 Ma .

With increasing metamorphic grade (from amphibolite to granulite) and oxidation state, allanite and monazite disappear from the assemblage and zircon became depleted in U and Th. Whole-rock U-Th compositions became decoupled from relict magmatic zircon compositions, reflecting the development of U-depleted magmatic zircon and indicating that whole-rock chemical differences along the traverse were produced during metamorphism, rather than just reflecting differences in dioritic vs. granitic protoliths. Although *in situ* anatexis and melt extraction may have played a role, whole-rock and zircon depletion of trace elements can be explained by the action of externally-derived, oxidizing, low-H_2O activity hypersaline fluids migrating up through the mid to lower crust. Fluids and element migration during metamorphism may be the end result of subduction related processes that cumulated in the collision and concatenation of island arcs and continental blocks. These tectonic processes assembled the Dharwar Craton at the end of the Archean.

Keywords: zircon, U-Th-Pb dating, SHRIMP, charnockite, granulite, amphibolite, Shevaroy Block, Dharwar Craton, southern India

INTRODUCTION

During high-grade metamorphism the geochemical signals associated with the genesis and subsequent geochemical history of the protolith are altered as a result of metamorphic and/or tectonic processes. Many minerals are incapable of at least partially preserving some record of these initial geochemical processes. One exception to this rule is zircon. With the advent of sub-30 micron scale analytical techniques involving Sensitive High-Resolution Ion MicroProbe (SHRIMP) and laser ablation inductively coupled plasma mass spectrometry (LA-ICPMS), the role of zircon as a recorder of geochemical and physical processes has become increasingly important in igneous and metamorphic petrology over the last 30 years (Davis *et al.*, 2003; Ireland & Williams, 2003; Kosler & Sylvester, 2003; Aranovich *et al.*, 2020). These techniques allow for analytical measurements of sub-grain areas in zircon grains, which have been used for the dating of geological events as well as for recording the geochemistry of fluids and melts associated with these events. They have also inspired a series of experiments, which have focused on zircon-fluid interaction where grains have been partly or totally metasomatised over a wide range of temperatures at pressures reflecting both upper crustal (Geisler *et al.*, 2007) and lower crustal conditions (Harlov & Dunkley, 2010).

In metamorphic rocks, zircon grains are remarkably robust at preserving information regarding the protolith in their cores, whilst their rims record the changes undergone by the host rock, as well as dating the metamorphic events that induce such changes (e.g. Konopasek *et al.*, 2014; Brandt *et al.*, 2014; Liu *et al.*, 2016; Stipska *et al.*, 2016; Raith *et al.*, 2016). This puts zircon in contrast to other geochronometers, such as fluorapatite, monazite, and xenotime, which are considerably more susceptible to metasomatic alteration, and as such are less likely to preserve protolith compositions (Harlov, 2011, 2015; Williams *et al.*, 2011). In many cases, accessory minerals can be viewed as purely metamorphic minerals, whereas zircons are often affected by multiple igneous and/or metamorphic events, while at the same time preserving chemical information regarding the protolith in which they originated. However, zircon can also record metamorphic processes through regrowth or recrystallization. Such zircon, whether it occurs as overgrowths on remnants of igneous zircon or replacement of pre-existing grains, will yield isotopic signatures (e.g. in U and Pb) that enable dating of metamorphic processes. It also records, through changes in composition, two aspects of change in rocks during metamorphism; a) changes in mineral assemblage at differing grades, as well as b) changes in the bulk composition of the host rock.

In the current study, zircon grain separates from 29 samples collected over an approximately 100 km long amphibolite- to granulite-grade traverse from the Shevaroy Block, southern India, have been chemically characterized and dated using SHRIMP-II analysis. This investigation builds upon a series of past studies involving the same samples begun by Hansen *et al.* (1995), which was later followed by investigations into sulfide-oxide relationships (Harlov *et al.*, 1997; Harlov, 2000; Harlov & Hansen, 2005), and a study of biotite, amphibole, fluorapatite, monazite, titanite, and allanite mineral chemistry and whole-rock chemistry as a function of increasing metamorphic grade (Hansen *et al.*, 2002; Hansen & Harlov, 2007). This study aims to compare the differences in composition between pre-existing and metamorphic zircon in samples of granitoid gneiss and charnockite subjected to amphibolite to granulite-grade metamorphism. Here, the first goal is to characterize the zircon grains from this sample set with respect to their textures as revealed by cathodoluminesence (CL) imaging. The second goal is to differentiate between the geochemistry and age of zircon present in the protoliths before metamorphism, (usually preserved in the cores of grains), versus that produced during high-temperature metamorphism, as preserved in the rims of the grains. Combining this information with the results and conclusions obtained from past studies allows us to construct a more comprehensive geochemical portrait of these rocks with regard to their transformation from protolith granitoids into gneisses, reveal and date the role that low H_2O activity fluids could have played during amphibolite- to granulite-grade metamorphism, as well as speculate on the origins of these fluids.

GEOLOGICAL BACKGROUND

Dharwar Craton

The Archean Dharwar Craton makes up a large segment of central and southern India. It is composed of a mosaic of crustal micro-blocks of varying ages separated from each other by deep crustal shear/suture zones (e.g., Drury & Holt, 1980; Drury *et al.*, 1984; Chadwick *et al.,* 2000; Ghosh *et al.*, 2004; Chardon *et al.*, 2008; Dey, 2013; Pecaut *et al.*, 2013; Collins *et al.*, 2014; Glorie *et al.*, 2014; Mohan *et al.*, 2014; Maibam *et al.*, 2016; Jayananda *et al.*, 2006, 2015, 2018, 2020). The Dharwar Craton mainly consists of tonalitic-trondhjemitic-granodioritic (TTG) gneisses, volcano-sedimentary greenstone belts, and a number of voluminous potassic and calc-alkaline granitoid intrusions (including the Closepet granite) that are mostly Neoarchean in age, (Fig. 1; Friend & Nutman, 1991; Jayananda *et al.*, 2000; Gireesh *et al.*, 2012; Mohan *et al.*, 2014). The northern part of the Dharwar Craton is mainly characterized by greenschist-grade schists and granitoid bodies with a NNW-SSE to N-S structural trend and sinistral shear zones formed by late Archean NE-SW crustal shortening (Chadwick *et al.*, 2000; Ishwar-Kumar *et al.*, 2013). The southern part is characterised by predominantly N-S to NE-SW structural trends (Chardon *et al.*, 2008; Peucat *et al.*, 2013) and is bound by amphibolite to granulite-grade gneisses along the southern margin (Drury & Holt, 1980; Drury *et al.*, 1984; Ghosh *et al.,* 2004; Peucat *et al.,* 2013). Fermor (1936) was the first to divide the northern greenschist to amphibolite-facies rocks of the

Dharwar Craton from the southern, orthopyroxene-bearing granulite-grade rocks via an orthopyroxene-in isograd termed the Fermor line. This line is still invoked as the northern margin of the Southern Granulite Terrane; however, this designation confuses high-grade rocks produced at the end of the Archean in the Dharwar Craton, and those produced by unrelated events in the late Proterozoic Pandyan Mobile Belt (Ramakrishnan, 1988). More recently, the Dharwar Craton has been divided into Western, Central, and Eastern provinces (Jayananda *et al.*, 2013, 2018). The Western Dharwar Craton is separated from the Central Dharwar Craton by a mylonite zone along the eastern margin of the Chitradurga schist belt (e.g., Swami Nath & Ramakrishnan, 1981; Chadwick *et al.*, 2000; Chardon *et al.*, 2008, 2011; Hokada *et al.,* 2013; Jayananda *et al.*, 2006, 2013, 2015; Tushipokla & Jayananda, 2013; Lancaster *et al.*, 2014; Sreehari and Toyoshima, 2020), whereas the Kolar suture zone separates the Central Dharwar Craton from the Eastern Dharwar Craton (Krogstad *et al.*, 1989; Jayananda *et al.*, 2013; Manikyamba *et al.*, 2015; Hazarika *et al.*, 2015; Yang and Santosh, 2015). Published geochronological results and Nd model ages indicate a magmatic age range for the Western Dharwar Craton of 3400 to 2900 Ma (e.g., Peucat *et al.*, 1993; Jayananda *et al.*, 2000, 2015, 2018; Bhaskar Rao *et al.*, 2003; Dey, 2013; Mohan *et al.*, 2014; Maibam *et al.*, 2016); a magmatic age range of 3400 to 2500 Ma for the Central Dharwar Craton (e.g., Peucat *et al.,* 2013; Ratheesh-Kumar *et al.,* 2016); and a magmatic age range of mostly between 2700 and 2500 Ma for the Eastern Dharwar Craton (Radhakrishna & Naqvi, 1986; Rogers & Giral, 1997; Clark *et al.*, 2009; Gireesh *et al.*, 2012; Glorie *et al.*, 2014; Maibam *et al.*, 2016; Jayananda *et al.*, 2018, 2020).

The southern granulite-grade parts of the Dharwar Craton are divided by faults and ductile shear zones into a set of tectonic blocks (Chardon *et al.*, 2008), which are dominated by charnockites (orthopyroxene-bearing TTG gneisses), and separated from each other by shear/suture zones (Drury & Holt, 1980; Drury *et al.*, 1984; Ghosh *et al.*, 2004; Chardon *et al.*, 2008; Peucat *et al.*, 2013; Ishwar-Kumar *et al.*, 2013; Collins *et al.,* 2014) (Fig. 1). They are sometimes given other names or else several of these blocks are grouped into one block (e.g. the Salem Block of Glorie *et* *al.*, (2014), which consists of the Shevaroy, Kolli, and Madras Blocks in Figure 1). Following the designations outlined by Ishwar-Kumar *et al.* (2013) (Fig. 1) these blocks have been defined as the Coorg Block (Chetty *et al.,* 2012; Ishwar-Kumar *et al.*, 2013, 2016; Santosh *et al.*, 2015); the Nilgiri Block (Raith *et al.*, 1999; Samuel *et al.*, 2014, 2019), the Biligiri Rangan Block (Peucat *et al.*, 2013; Ratheesh-Kumar *et al.*, 2016, 2020); the Shevaroy Block (Li *et al.*, 2018; Thanooja *et al.*, 2021a); the Kolli Block (also known as Namakkal Block) (George and Sajeev, 2015; Behera *et al.*, 2019; Gou *et al.*, 2022); and the Madras Block (Rameshwar Rao *et al.,* 1991a,b; Braun & Kriegsman, 2003) (Fig. 1). The charnockite in these blocks form a band of hilly terrains, which transect southern India from the west to the east coast (Fig. 1). The southern margin of the Dharwar Craton is separated from the Madurai Block by the Palghat-Cauvery shear zone (Drury & Holt, 1980; Drury *et al.*, 1984; Plavsa *et al.*, 2012, 2014; Santosh *et al.*, 2009, 2017).

Shevaroy Block

The Shevaroy Block is located in the Eastern Dharwar Craton. It is bound to the south by the Salem-Attur shear zone (SASZ) and along the eastern and western margins by the Mettur-Kolar shear zone (MKSZ) and Nallamalai (NSZ) shear zones, respectively (Drury & Holt, 1980; Ishwar-Kumar *et al.*, 2013; Li *et al.*, 2018; Figs. 1 & 2; Electronic Supplementary Appendix 1a,b). The NNE-SSW trending southern Mettur-Kolar shear zone (Krogstad *et al.*, 1989; Yang & Santosh, 2015; Rathesh-Kumar *et al*., 2016) separates the Shevaroy Block from the Biligiri Rangan Block to the west, and joins the Salem-Attur shear zone in the south (Figs. 1 & 2). The NE-SW trending Nallamalai shear zone (Li *et al.*, 2018; Thanooja *et al.*, 2021a) separates the Shevaroy Block from the Madras Block in the east. The E-W trending Salem-Attur shear zone, which continues from Bhavani to Attur through Salem, separates the Shevaroy and Madras Blocks from the Kolli (Namakkal) Block in the south (Drury *et al.*, 1984; Ishwar-Kumar *et al.*, 2013, 2016; Li *et al.*, 2018; Thanooja *et al.*, 2021a,b). The Shevaroy Block is characterised by NE-SW trending structural lineaments, which in places swings around the hinges of regional folds. The region is intruded by several dolerite dykes, which are mostly perpendicular to the major structural trend of the Block (Fig. 2a).

In general, the Shevaroy Block is dominated by intermediate to felsic quartzo-feldspathic, metamorphosed gneisses with a coarse granoblastic texture, which belong to a set of late Archean tonalite-trondhjemite-granodiorite (TTG) gneisses typical of the southern Dharwar Craton (Condie *et al.*, 1982; Rameshwar Rao *et al.*, 1991a; Jayananda *et al.*, 2012; Peucat *et al.*, 2013; Glorie *et al.*, 2014; Jayananda *et al.*, 2018; Peng *et al.*, 2019) (Fig. 2a). The granodioritic to tonalitic gneisses commonly contain mafic layers and lenses, which occasionally form larger (outcrop scale) bodies. Younger, ultramafic rocks are present in the central and south-eastern part of the Shevaroy Block (Geological Survey of India, 2005). Numerous small granitic plutons occur in the northern half of the Shevaroy Block and are concentrated in the vicinity of the orthopyroxene-in isograd (Hansen *et al.*, 1995; Fig. 2a). Several Neoproterozoic syenite intrusive bodies occur in the northeastern and southwestern part of the Shevaroy Block (Glorie *et al.*, 2014). Metasedimentary rocks make up a minor component of the block overall.

Based on U-Pb isotopic dating of zircon, the primary episode of metamorphism resulting in the gneisses and granulites of the Shevaroy Block occurred at ca. 2500 Ma, similar to age estimates in the adjacent Blocks (Glorie *et al.*, 2014). A compilation of all dated locations in the Shevaroy Block up to the present along with the relevant references (Electronic Supplementary Appendix 1b) is plotted in Figure 2a. Precise estimates for peak zircon growth during metamorphism mostly fall between 2550 and 2500 Ma (Glorie *et al.*, 2014), with slightly younger estimates (e.g., ca. 2480 Ma), obtained by Clark *et al.* (2009) in a quarry of massive charnockite 50 km north of Salem in the Shevaroy massif (Fig. 2a). A similar RB-Sr whole-rock isochron age of 2476 ± 115 Ma was obtained by Spooner & Fairbairn (1970) for granulites from the Salem area. Relatively low-U overgrowths on higher-U cores in zircon from most dated samples were interpreted by Clark *et al.* (2009) and Glorie *et al.* (2014) to represent growth during metamorphism and magmatism, respectively. Many cores with ca. 2550 Ma ages were attributed by these authors to the emplacement of granitoid protoliths immediately before and during metamorphism, with the latter causing a widespread anatexis, which resulted in the granulites. Glorie *et al.* (2014) also suggested that these protoliths represented newly generated crust, on the basis of chondritic to supra-chrondritic ε_{Hf} values (ε_{Hf} = ^{176}Hf/^{177}Hf normalized to chondritic values) for the zircon cores. A lesser component of juvenile ca. 2700 Ma granitoid protoliths was also recognised.

Harlov & Hansen (2005) divided the Shevaroy Block along a north-south traverse into 3 metamorphic zones. The Northern Amphibolite-Facies Zone (NAF) occurs north of the first appearance of orthopyroxene in the quartzo-feldspathic gneisses (Table 1; Fig. 2b; Electronic Supplementary Appendix 1). The grey gneisses in this zone include leucocratic bands, mafic and calcsilicate enclaves, and granitic and granitic pegmatitic pods and veins. They contain biotite ± hornblende, with clinopyroxene appearing a few kilometres north of the orthopyroxene-in isograd.

The Central Granulite-Facies Zone (CGF) begins at the orthopyroxene-in isograd in the quartzo-feldspathic gneisses (Table 1; Fig. 2b; Electronic Supplementary Appendix 1). The most abundant rock in this area is dark grey, quartzo-feldspathic gneiss. In this northern half of the CGF, clinopyroxene is the most abundant pyroxene although many samples contain subordinate amounts of orthopyroxene. Biotite is more abundant than either clinopyroxene or orthopyroxene. Hornblende is found in some samples. Going southwards, biotite and clinopyroxene becomes less abundant and orthopyroxene becomes more abundant (Harlov & Hansen, 2005; Hansen & Harlov, 2007). The gneisses are typically characterised by a compositional banding and a mineral foliation largely defined by an alignment of elongated quartz grains and Fe-Mg-bearing minerals. Isoclinal folds are seen in places. In some outcrops, particularly in the north of the CGF, zones with higher strain (shear zones) are present and contain a foliation that cuts across the main foliation. Lensoidal mafic enclaves, containing hornblende, clinopyroxene, and orthopyroxene, were observed in most outcrops. Some small outcrops consist almost entirely of mafic rock. Coarser-grained, quartzo-feldspathic patches and veins, sometimes containing orthopyroxene and clinopyroxene, occur within the mafic rocks in these outcrops.

Pink granite, both as compositional bands and in veins and patches that cut across foliation, is abundant in the northern half of the CGF, which compliments the numerous small granitic plutons seen in the area (Fig. 2). The granitic compositional bands often pinch and swell along their length. The amount of granite varies from outcrop to outcrop. In a few cases the discordant granite veins and patches are so abundant that the gneiss begins to lose its structural coherency. Some small outcrops consist entirely or almost entirely of granite, which is in places porphyroclastic with a mineral foliation. Clinopyroxene, and to a lesser extent orthopyroxene, is visible in some of the granite veins and patches within the gneiss but biotite is typically more abundant. In both the gneisses and in the granite biotite, clinopyroxene, and orthopyroxene tend to occur together, sometimes with hornblende, in either mafic bands or mafic patches. Orthopyroxene and clinopyroxene are often in direct contact with biotite and hornblende as well as with quartz and feldspar. Rims of biotite or amphibole completely surrounding orthopyroxene or clinopyroxene are rare but do occur. Granitic leucosomes were observed less frequently in the southern half of the CGF where the rocks began to resemble those in the Shevaroy Hills massif.

The Southern Granulite Facies Zone (SGF) consists of the Shevaroy Hills massif (Table 1; Fig. 2; Electronic Supplementary Appendix 1). The most common rocks encountered here are a felsic to intermediate dark orthopyroxene-bearing gneiss. In addition to quartz, feldspar, oxides (magnetite and hemo-ilmenite), and sulfides (pyrite and pyrrhotite) a subset of samples contained garnet (Harlov *et al.*, 1997; Harlov & Hansen, 2005; Hansen & Harlov, 2007). Rare Ti-rich biotite, partly as a secondary reaction product after orthopyroxene, is observed in most samples and rare Ti-rich amphibole in only a scattering of samples. Mineral foliation and banding are ubiquitous. The amount of apparent strain, as expressed in the degree of stretching and flattening in the feldspars and quartz, is variable with some approaching a mylonitic fabric. A mineral lineation within the plane of the foliation was noted in a few places and may be more common than our observations indicate. Isoclinal folds with axial planes parallel to the gneissic foliation were observed in several outcrops. Coarser-grained feldspar, quartz, and orthopyroxene-bearing veins or patches as well as quartz veins were observed in some outcrops. These veins are most often concordant with the foliation but occasionally cut across it. Most contacts between orthopyroxene and quartz and feldspar are sharp in both the finer grained quartzo-feldspathic gneisses and the coarser grained veins within them. Hydrous ferromagnesian silicates (such as biotite, hornblende, or chlorite) at the margins of the orthopyroxene or clinopyroxene grains are rare. Continuous rims of biotite and/or amphibole are not observed. In the SGF and CGF, the majority of the quartz grains in contact with plagioclase are rimmed by micro-veins of K-feldspar (Hansen *et al.*, 1995; Harlov *et al.*, 1998; Hansen & Harlov, 2007). Replacement antiperthite (Griffin, 1969) occurs sporadically in a scattering of plagioclase grains. These feldspar micro-textures are not seen in the NAF.

The second most common rock type encountered in the SGF (10 – 15%) is mafic granulite. These rocks contain clinopyroxene and plagioclase +/- orthopyroxene +/- garnet. Intermediate to felsic orthopyroxene-bearing rocks are typically mixed with the mafic granulites in variable proportions. At one end of the scale, the mafic granulite can occur as a few submeter, lensoidal enclaves within quartzo-feldspathic, orthopyroxene-bearing gneisses. At the other extreme, outcrops of mafic granulite contain minor amounts of quartzo-feldspathic, orthopyroxene-bearing veins and patches. Usually the orthopyroxene in these patches is in direct contact with quartz or feldspar with no intervening hydrous ferromagnesian silicates.

Two other relatively minor rock types (< 1%) were observed as enclaves and partially disrupted bands within several outcrops. The more abundant of these is a garnet- and biotite-rich gneiss, which typically contains small scattered orthopyroxene and clinopyroxene grains. Together biotite and garnet typically make up over 50 modal percent of these rocks with feldspar making up the bulk of the remaining minerals. Sapphirine was found in one example. The nature of the protolith of these aluminous rocks is not clear although they may be either metasediments or highly altered igneous rocks. The least abundant of the minor rock types (a couple of small outcrops) is a two-pyroxene ultramafic rock (websterite) with hornblende rich patches. Lastly, a few discordant coarser-grained granite patches are observed in gneisses at the southern margin of the SGF.

Pressure and temperature estimation across the Shevaroy Block traverse

Utilizing garnet-orthopyroxene Fe-Mg exchange thermometry and garnet-orthopyroxene-plagioclase barometry, Hansen *et al* (1995) determined internally consistent mean pressures and temperatures of 830 ± 50 MPa and 810 ± 70 °C for the SGF. Utilizing this same regional pressure Harlov *et al.* (1997) obtained a mean garnet-orthopyroxene temperature of 740 ± 50 °C and a mean QUIlP two pyroxene temperature of 750 ± 50 °C for the SGF (cf. Anderson *et al.*, 1993).

Rameshwar Rao *et al.* (1991b) obtained mean temperatures and pressures of 775 ± 30 °C and 800 ± 150 MPa for the CGF from a variety of geothermometers and geobarometers. Assuming a regional pressure of 600 MPa, Harlov *et al.* (2005) estimated a similar mean temperature of 780 ± 25 °C using the QUIlP two-pyroxene geothermometer (Anderson *et al.*, 1993) for a series of samples across the entire CGF and saw little evidence of any regional temperature variation. In the vicinity of the orthopyroxene-in isograd and clinopyroxene-rich zone, Rameshwar Rao *et al.* (1991b), using a variety of geothermometers and geobarometers, estimated a temperature and pressure of 730 ± 40 °C and 550 ± 150 MPa.

Hansen *et al.* (1995) obtained pressures of 300 to 470 MPa for the NAF utilizing an Al-in-hornblende geobarometer and estimated temperatures of around 700 °C. Hansen *et al.* (1995) concluded that the Shevaroy Block represents a north tilting unbroken cross section of approximately 12 to 15 kilometres thick, lower, late Archean continental crust truncated by erosion with paleodepths of 12 to 15 km for the NAF and 24 to 30 km for the SGF.

OXIDE, SULFIDE, AND ACCESSORY MINERALS ALONG THE SHEVAROY BLOCK TRAVERSE

Changes in oxidation states and accessory mineral abundances, mineralogy, and mineral chemistry along the Shevaroy Block traverse have been described and interpreted by Harlov *et al.* (1997), Harlov & Hansen (2005), and Hansen & Harlov (2007) as a function of both changing oxidation and sulfidation states as well as REE mobility. In each of these studies, these changes have been ascribed to the presence of hypersaline fluids during metamorphism with an evolving SO_2/H_2S component, which resulted in an evolving oxygen fugacity and sulfur fugacity, and an evolving H_2O activity.

Oxide-sulfide mineralogy and petrology

Across the whole of the Shevaroy Block traverse the oxides and sulfides show distinct mineralogical, petrological, and geochemical trends (Table 1; Harlov *et al.*, 1997; Harlov & Hansen, 2005). Ilmenite occurs primarily as hemo-ilmenite (up to 55 mole% hematite) in the SGF and in the southern half of the CGF and more commonly as ilmenite with either a minor or non-visible hematite component in the northern CGF (Table 1; Fig. 2; Fig. A2-1a in Electronic Supplementary Appendix 2). Utilizing the assemblage clinopyroxene-orthopyroxene-magnetite-hemo-ilmenite, estimated temperature-$\log_{10}fO_2$ arrays in the SGF and CGF result in internally self-consistent temperature-$\log_{10}fO_2$ arrays ranging from 660 °C/$\log_{10}fO_2$ = -16 bar to 820 °C/$\log_{10}fO_2$ = -11.5 bar. Orthopyroxene in the SGF has a high Mg/(Mg + Fe) ratio (0.5–0.7), reflecting the high oxidation state, and which decreases with a decreasing oxidation state (Harlov *et al.*, 1997). Oxidation rims of magnetite + quartz occur along orthopyroxene, clinopyroxene, and amphibole grain boundaries (Table 1; Figs A2-1c,d in Electronic Supplementary Appendix 2), which Harlov *et al.*, (1997) and Harlov & Hansen (2005) attributed to the release of O_2 along grain boundaries by the partial reduction of hematite lamellae in ilmenite to magnetite (Table 1; Fig. A2-1b in Electronic Supplementary Appendix 2) during post-peak metamorphic uplift and cooling in the SGF and CGF.

In the most oxidized granulite samples from the SGF (X_{Hm}^{Ilm} > 0.4), abundant pyrite is the dominant sulfide and pyrrhotite is absent (Harlov *et al.*, 1997). Pyrite grains in these samples are generally rimmed by magnetite, which represent partial retrograde oxidation of the pyrite during post peak metamorphic uplift and cooling (Table 1; Figs. A2-2a,b in Electronic Supplementary Appendix 2; see above and also Harlov *et al.*, 1997; Harlov & Hansen, 2005). Moderately oxidized samples (0.1 < X_{Hm}^{Ilm} < 0.4) have abundant co-existing pyrrhotite, pyrite, and magnetite (Table 1; Fig. A2-2c in Electronic Supplementary Appendix 2). The most reduced granulite samples have abundant pyrrhotite as the dominant sulfide with little or no pyrite and no coexisting magnetite. In the CGF pyrrhotite is absent while pyrite, often associated with or rimmed by magnetite in the southern half of the CGF, is widespread throughout decreasing in abundance going from south to north (Harlov & Hansen, 2005).

In the NAF, pyrite and magnetite are very rare (Table 1). Modal amounts of ilmenite are lower than in SGF or CGF samples. Ilmenite does not have a hematite component and is commonly partially consumed by titanite along the grain rims (Fig. A2-3h in Electronic Supplementary Appendix 2; Harlov & Hansen, 2005). There is a total lack of magnetite oxidation rims along amphibole and clinopyroxene grain boundaries. The prevalent mineral assemblages suggest that the oxygen fugacity during amphibolite-facies metamorphism was probably at or below FMQ.

Apatite-monazite-titanite-allanite petrology and geochemistry

The REE-bearing minerals show a distinct progression in mineral type going from the southern to the northern end of the traverse (Table 1; Fig. 2; Fig. A3 in Electronic Supplementary Appendix 2; Hansen & Harlov, 2007). In the SGF and CGF, 80 % of all fluorapatite grains contain inclusions and/or small rim grains of Th-poor monazite (Table 1; Fig. A3a-d in Electronic Supplementary Appendix 2). Apatite-fluid experiments (e.g. Harlov *et al.*, 2002, 2005; Harlov & Förster, 2003) have demonstrated that these inclusions and rim grains originate from the fluorapatite via a fluid-activated, coupled dissolution-reprecipitation reaction (Putnis, 2009). Subsequent re-integration of the monazite inclusions and rim grains back into the fluorapatite indicate that the original fluorapatite grains had REE contents ranging from 2 to 4 wt% (Hansen & Harlov, 2007). Discrete grains of monazite, allanite, and titanite are absent.

Approaching the orthopyroxene-in isograd, discrete, isolated Th-enriched monazite grains, not associated with fluorapatite, appear with variable patchiness (Table 1; Figs. A3e,f in Electronic

Supplementary Appendix 2; also see fig. 13 in Hansen & Harlov, 2007). This variable patchiness is due to variations in the Th, U, Si, Ca, and REE content within the monazite grain (see discussion in Hansen & Harlov, (2007) and Harlov *et al.*, (2011)). These are found principally in the clinopyroxene-rich zone straddling the orthopyroxene-in isograd (Table 1; Fig. A3e,f in Electronic Supplementary Appendix 2). Some monazite grains are rimmed by post-peak metamorphic allanite (Fig. A3g in Electronic Supplementary Appendix 2).

In the NAF, the principal REE-bearing minerals are (Y-REE)-enriched (1 – 2 REE_2O_3 wt%) titanite, which commonly rims ilmenite (Table 1; Fig. A3h in Electronic Supplementary Appendix 2), and less commonly, allanite, which occurs either as discrete grains or rimming monazite grains in the clinopyroxene-rich zone (Table 1; Fig. A3g in Electronic Supplementary Appendix 2; Hansen & Harlov, 2007). Typically, the fluorapatite grains contain no monazite inclusions, with a few exceptions in several samples from the southern half of the NAF in the clinopyroxene-rich zone.

There is little evidence of REE depletion, more specifically LREE depletion, across the length of the Shevaroy Block traverse (see Hansen & Harlov, 2007 their fig. 3e) but rather the redistribution of the REE between various mineral phases as a function of P-T, which suggests that partitioning of the REE favoured a specific mineral (fluorapatite, monazite, zircon, titanite, or allanite) as a function of metamorphic grade, i.e. P-T, as opposed to whole-rock chemistry or whatever fluids and/or melts that may have been present.

ANALYTICAL TECHNIQUE

Twenty nine samples were chosen for zircon geochronology and zircon (Y+REE) trace element measurement. The samples are spaced along a traverse extending from five kilometres north of Krishnagiri southwards for 95 km, ending at the southern margin of the Shevaroy Hills along the Salem-Attur shear zone (Table 1; Fig. 2). These samples were chosen from the original 50 covered in Hansen & Harlov (2007) along with the addition of 8 new samples selected to cover gaps in the original sample distribution across the traverse due to the lack of additional material for some of the original samples covered in Hansen & Harlov (2007). Overall, samples were selected with regard to their major-element, whole-rock compositions, which range from granodioritic to tonalitic (Hansen *et al.*, 1995), as well as with regard to their positions along the traverse. Sample numbers, numbering 1 through 29, are associated with the sample labels in Table 1 and successive tables, in Figure 2 and successive figures, as well as in the appendices. Sample 1 corresponds to the northernmost sample in the NAF and Sample 29 corresponds to the southernmost sample in the SGF. These sample numbers, as opposed to sample labels, are often referred to in the text and figures for the sake of brevity.

Analytical technique including whole-rock analysis and SHRIMP analysis of zircon and titanite are contained in Electronic Supplementary Appendix 3. Whole rock trace element data is contained in Table 2. A selection of the zircon age data for all 29 samples is contained in Table 3. The full data set is contained in Electronic Supplementary Appendix 4. A representative collection of zircon CL images, which show the analysis points, is contained in Electronic Supplementary Appendix 5. A selection of the zircon SHRIMP REE data for all 29 samples is contained in Table 3. The full data set is contained in Electronic Supplementary Appendix 6. Titanite age data for 3 samples from the NAF are contained in Table 4.

WHOLE-ROCK GEOCHEMISTRY

When plotted on a normative feldspar plot (O'Connor, 1965), samples from the SGF and CGF utilized in this study plot mostly in the tonalite and granodiorite field, whereas samples from the NAF plot in the granite field along the granite-granodiorite and granite-quartz monzonite boundary (Fig. 3; cf. Electronic Supplementary Appendix 7a). This plot reflects what is seen in a normative feldspar plot for a larger set of samples from the same traverse contained in Hansen *et al.* (1995) (their figure 8).

Major element whole-rock analysis for 50 samples along the traverse (cf. Hansen & Harlov, 2007, their fig. 2) indicate that there are no obvious systematic trends in Fe/(Fe + Mg), TiO_2, MnO, K_2O, CaO, and SiO_2 (see also Table 1, Electronic Supplementary Appendix 7a, & Figs. 4a,b).

The changes in mineral assemblages and abundances are roughly paralleled by changes in the abundances of some LIL trace elements, the REE, and the actinides (Rameshwar Rao *et al.*, 1991a; Hansen *et al.*, 1995; Hansen & Harlov, 2007, their fig. 3) (Tables 1 & 2; Fig. 4). Most intermediate and felsic gneisses in the NAF and northern CGF have moderate to high Rb (8–107 ppm), Th (0.4–27 ppm), and U (0.1–1.5 ppm) concentrations and K/Rb ratios below 500 (Rameshwar Rao *et al.*, 1991a; Hansen *et al.*, 1995, 2002; Table 2; Fig. 4c,e,f). Low concentrations of Rb (< 30 ppm), U (< 0.3 ppm), and Th (< 3 ppm) and high K/Rb ratios (> 500 ppm) become common in the southern orthopyroxene-rich portion of the area, i.e. SGF and the southern half of the CGF (Table 2; Fig. 4). Hansen *et al.* (2002) found that samples, containing very low, whole-rock concentrations of Rb and high K/Rb ratios, are characterised by both relatively low abundances of biotite and low concentrations of Rb in biotite.

Total REE concentrations show greater variability with somewhat higher average values in the NAF and CGF (Fig. 4d; cf. Hansen & Harlov, 2007, their fig. 4). However, these regional trends are relatively weak. The average chondrite-normalized REE patterns for the three metamorphic zones show enrichment in LREE. Whereas the patterns from the NAF and CGF are parallel, the pattern from the SGF is less LREE-enriched and more HREE enriched relative to the NAF and CGF (cf. Hansen & Harlov, 2007, their fig. 4).

PSEUDO-SECTION MODELLING

In order to construct pseudo-sections for three typical TTG samples from the Shevaroy traverse (93 F3 O1, 93 F9 I1, and 93 F9 F8), H_2O activities were first estimated for these samples from the equilibrium: 3 orthopyroxene + K-feldspar + H_2O = biotite + 3 quartz utilizing the mineral chemical data for these samples taken from Harlov *et al.* (1997, 1998), Harlov & Hansen (2005), and Hansen

& Harlov (2007). Estimation of H_2O activities was done per the thermodynamic data and model outlined in Aranovich & Newton (1998) and Berman *et al.* (2007). Utilizing this data and equilibrium resulted in H_2O activities of 0.24 for 93 F3 O1; 0.18 for 93 F9 I1; and 0.21 for 93 F9 F8. For an H_2O-CO_2 system, this would correspond to an X_{H2O} value of around 0.1 to 0.14 for the regional high-grade P-T conditions characteristic of the Shevaroy Massif (800 °C and 800 MPa) (Aranovich & Newton, 1999). In the case of hypersaline fluids at pressures above 400 to 500 MPa, the H_2O activity is approximately equal to X_{H2O} squared (Aranovich & Newton, 1996, 1997). Hence the H_2O activity values in a hypersaline system would correspond approximately to X_{H2O} values of 0.4 to 0.35. The presence of CO_2 during the granulite-facies metamorphism of these rocks is implied due to the presence of numerous, primary high-grade CO_2-rich fluid inclusions preferentially trapped in the charnockites from the CGF and SGF (Manjari, 1993; Santosh & Tsunogae, 2003; Sourabh Bhattacharya, private communication), which is a common feature in both metamorphic and igneous charnockites world-wide (Satish-Kumar, 2005; van den Kerkhof *et al.*, 2014). Hence for a hypersaline system, a minor CO_2 component must be included.

Temperature-pressure pseudo-section plots (700 – 1000 °C; 200 – 1200 MPa) were calculated for the three TTG samples from the high-grade Shevaroy massif (93 F3 O1, 93 F9 I1, and 93 F9 F8), utilizing the whole rock data in Electronic Supplementary Appendix 7a, converted to mole percents in Electronic Supplementary Appendix 7b, were created using the Holland & Powell (2011) mineral chemical database (hp11ver.dat) implemented in the PerpleX (version 6.7.9) software of Connolly (2005). Two sets of pseudo sections were calculated; one for an NaCl-bearing hypersaline fluid with a minor CO_2 component (X_{H2O} = 0.4 and 0.5) and one for an H_2O-CO_2 system (X_{H2O} = 0.1 and 0.2). The pseudo-section in Figure 5a was calculated for 93 F9 F8 using the H_2O-CO_2-NaCl fluid model of Aranovich *et al.* (2010) for X_{CO2} = 0.1, X_{NaCl} = 0.4, and X_{H2O} = 0.5. For comparison, a second pseudo-section in Figure 5b was calculated for 93 F9 F8 using the H_2O-CO_2 fluid model of Holland & Powell (1991, 1998) for an X_{CO2} of 0.8 and X_{H2O} of 0.2. Similarly, for the same sample, pseudo-sections were calculated for X_{NaCl} = 0.5, X_{CO2} = 0.1, and X_{H2O} = 0.4 in

Figure 5c and for X_{CO2} = 0.9 and X_{H2O} = 0.1 in Figure 5d. A series of H_2O-CO_2-NaCl and H_2O-CO_2 pseudo-section plots over a broad range of X_{H2O} for all three samples utilizing the Aranovich *et al.* (2010) H_2O-CO_2-NaCl fluid model and the Holland & Powell (1991, 1998) H_2O-CO_2 fluid model, respectively, can be found in Electronic Supplementary Appendix 7c.

The following mineral solution models were used in the modelling of the pseudo-sections: clinopyroxene (Green et al., 2016); garnet (White *et al.*, 2014); orthopyroxene (White *et al.*, 2014); plagioclase and K- feldspar (Holland & Powell, 2003); biotite (White *et al.*, 2014); amphibole (Green *et al.*, 2016); and magnetite (White *et al.*, 2002). The solution model for partial melts was taken from Green *et al.* (2016). The Andersen & Lindsley (1988) solid solution model for ilmenite coexisting with magnetite was used for ilmenite. The O_2 value for each sample was estimated using the 2 FeO + O = Fe_2O_3 equilibrium with the FeO/Fe_2O_3 ratios given in Electronic Supplementary Appendix 7b.

ZIRCON PETROGRAPHY

In zircons from high-grade metamorphic gneisses of the CGF and SGF preservation is almost invariably partial, with remnants of pre-metamorphic zircon encased in the cores of zircon crystals grown during metamorphism. Consequently, the interpretation of geochronological and compositional data from sub-grain analysis of zircon crystals, such as that enabled by the ion microprobe, requires the careful characterisation of the analysed zircon domains into xenocrystic, igneous, detrital, and metamorphic types. For each sample in this study, external and internal zircon morphologies, and associations with adjacent mineral phases, were examined in detail. Polished grain mounts typically hosted 50 to 400 grains per sample for which high-resolution reflected, BSE, and CL imaging was captured. Polished thin sections containing zircon from each sample were also examined by optical, BSE, and CL imaging.

In this section, zircon is described according to the position of each sample within the NAF, CGF, and SGF. For brevity, zircon descriptions are organised according to the interpretation of their internal morphologies via the representative images provided in Figures 6, 7, and 8. In addition to Electronic Supplementary Appendix 5, a large set of additional supporting BSE and CL figures, showing zircon features and their relation to the surrounding mineralogy and petrography in polished rock thin sections for each sample, are contained in Electronic Supplementary Appendix 8. Compositional variation is described in terms of CL brightness, which is typically antithetical to BSE brightness, i.e. CL-bright matches BSE-dark, and vice versa.

Northern Amphibolite Facies Zone (NAF)

Samples 1 through 7 are of grey TTG gneiss from the NAF zone (Table 1; Figs. 2 & 6; Electronic Supplementary Appendices 5 & 8). In all of these samples, the majority of zircon grains separated for analysis are elongate with prisms dominant over terminal bipyramids. Most of the surfaces, however, are not smooth and euhedral; instead, prism faces are slightly irregular and edges and corners are rounded. Internally, almost all grains are dominated by cores with regular faceted growth zoning and gradational to oscillatory compositional zoning (Figs. 6a,b), typical of growth in a fractionating magma. Elongate inclusions of apatite are common in zircon cores, as is commonly observed in zircon grown in granitic magmas (Corfu *et al.*, 2003). Growth zoning in these cores is typically truncated by mantles and rims of zircon that lack planar growth zoning. In samples 1 through 4, the rims tend to be CL-dark compared to the cores, and have gradational or no clear compositional zoning (Figs. 6a,b,c,g). Where variation is observed, it typically involves a decrease in CL brightness towards the edges of grains. This is also present in the few grains that lack distinct cores (Fig. 6c).

CL-dark rims and mantles are also found in zircon grains from samples 5 through 7 (Electronic Supplementary Appendix 8). In these samples additional rims of moderate to CL-bright zircon are also present (Figs. 6d,e,f). These rims tend to show rounded and irregular growth zoning, and where best developed around zircon terminations, sector zoning is also observed (Figs. 6d,f). The interfaces of this generation of zircon rim with cores tend to be smooth and rounded, and appear to truncate both of the generations of CL-dark zircon (Figs. 6e,f). Both CL-bright and -dark rims are typical of zircon grown during high-grade metamorphism (Corfu *et al.*, 2003). The discordant relationship between generations of differing composition indicates a growth hiatus between these generations. Modification of pre-existing zircon is also demonstrated by disruption of zoning within cores due to irregular patches of CL-dark and CL-light zircon (Fig. 6f), which is attributed to recrystallization during metamorphism.

Within polished thin sections, mineral assemblages are predominantly granoblastic, and zircon grains have edges that show polygonal growth relationships with other phases including ilmenite, apatite, amphibole, and clinopyroxene. In samples 1 through 4, grains with CL-dark rims are intergrown with, and partially or totally enclosed within, metamorphic quartz, plagioclase, biotite, amphibole, and apatite (e.g. Fig. 6h). Titanite, where present as rims around ilmenite, is in places truncated by zircon grains (Fig. 6g), consistent with growth after CL-dark zircon was formed. In samples 5 and 7, where zircon is enclosed within phases such as ilmenite or apatite, CL-bright rims are less developed or absent, whereas they are well developed adjacent to quartz or feldspar (Fig. 6h).

Central Granulite Facies Zone (CGF)

Samples 8 through 20 are from TTG ortho- and clinopyroxene-bearing orthogneisses located within the CGF zone (Table 1; Figs. 2 & 7; Electronic Supplementary Appendices 5 & 8). Zircon morphologies are more diverse in this section of the traverse. In most samples they have predominantly elongate prismatic forms with rounded terminations, whereas some samples, especially towards the south end of the CGF (samples 16, 18, 19, and 20), tend to have squat, equant, and irregular morphologies. Most samples have some mixture of these types.

Internally, almost all zircon from all samples contain cores with concentric faceted growth zones, showing gradational to oscillatory variations in CL brightness (Figs. 7a,b; Electronic Supplementary Appendices 5 & 8). Zircon grains with relatively unzoned, CL-dark cores are also common in some samples (samples 12, 13, and 16 through 20; Fig. 7c). Apatite inclusions are frequently present in cores (Figs. 7d,e). Small irregular patches of slightly more CL-bright zircon are commonly observed along faceted zones and around inclusions (Figs. 7d,g,h), possibly indicating recrystallization and/or multiple stages of zircon dissolution and regrowth within the cores. In a few grains, distinct stages of faceted zircon growth can be identified in BSE and CL images, with irregular interfaces truncating growth zones between stages (Fig. 7h). As with similar zircon cores in grains from NAF zone samples, these are interpreted as zircon grown in magma. Assuming that the protoliths of the granulite-facies samples from the CGF are igneous, it is probable that most of these zircon cores represent growth in a granitic melt. However, it is also likely that some are xenocrystic, especially where multiple generations of igneous zircon can be identified in grains, such as in Figure 7h.

In most grains in samples from the CGF zone, magmatic growth-zoning in zircon cores is truncated by mantles of zircon with a similar BSE and CL brightness, but lacking in clear planar or oscillatory growth zones (Figs. 7a,b,c; Electronic Supplementary Appendices 5 & 8). These correspond in appearance with the cores or main features of other grains in some samples (Figs. 7e,f). Compositional zoning in these mantles tends to be gradational, concentric, and simple planar to rounded; sector-zoning is also common (Fig. 7e). In appearance, these are similar to the rims of zircon in samples from the NAF zone, although a decrease in CL brightness from core to rim is less pronounced. Accordingly, this generation of zircon is also interpreted as having grown during high-grade metamorphism.

Almost all of the zircon grains in samples from the CGF zone have relatively moderate to CL-dark cores and mantles, and, whether interpreted as igneous or metamorphic zircon, are enclosed in rims of CL-bright zircon (Electronic Supplementary Appendices 5 & 8). Where best developed, usually on the terminations of elongated grains (Figs. 7a,b), these rims are externally faceted or rounded, and have internal growth zoning with simple faceted or rounded surfaces, as well as uncommon sector zoning. The interfaces of CL-bright rims with zircon cores and mantles are either planar to rounded (Figs. 7c,d) or embayed (Figs. 7e,f,g,h). In both cases, zoning in the cores/mantles are typically truncated. Truncated growth zones are also found within the CL-bright rims (Figs. 7a,e,h) that imply multiple stages of zircon growth and dissolution. These CL-bright rims are interpreted as zircon growth during metamorphism, but as a discrete stage of growth from moderate to CL-dark mantles and rims grown during metamorphism.

In polished thin sections, zircon grains with mantles and rims of both moderate to CL-dark metamorphic zircon and CL-bright metamorphic zircon are found with polygonal growth margins against other phases in granoblastic assemblages, such as quartz, plagioclase, amphibole, ilmenite, apatite, and pyroxene (Figs. 7g,h; Electronic Supplementary Appendix 8). Well-developed CL-bright zircon rims are found in textural equilibrium with amphibole, either on grain boundaries or as inclusions (Fig. 7g). These paragenetic relationships support the interpretation of zircon rim growth during high-grade metamorphism.

Southern Granulite Facies Zone (SGF)

Samples 21 through 29 are from TTG orthopyroxene-bearing gneisses from the SGF zone (Table 1; Figs. 2 & 8; Electronic Supplementary Appendices 5 & 8). The samples were selected as higher-grade equivalents of the felsic orthogneiss elsewhere on the traverse. However, the presence of detrital zircon cores suggests that the possibility of metasedimentary protoliths cannot be completely ruled out. This is especially true for sample 22, which is garnet-bearing, and thus may have had a peraluminous granitoid or metasediment protolith.

Zircon grains from these samples are essentially similar to those from samples in the CGF zone, especially samples 18 through 20 (Fig. 8f). Grains from samples 21, 24, and 25 are predominantly prismatic with rounded terminations, although highly elongate grains are rare; grains from the remaining samples are mostly squat to equant and irregular, and subhedral to anhedral (Fig. 8; Electronic Supplementary Appendices 5 & 8). All of the samples yielded some zircon grains with planar to oscillatory-zoned cores (Figs. 8a,b,c,e), identical to those interpreted as igneous zircon in previous samples. The growth zoning in these cores is truncated by mantles and rims of later grown zircon, and the truncated interface is often marked by thin, patchy replacement with relatively CL-bright zircon (Figs. 8a,c,e,h). In samples 23, 27, 28, and 29, these cores form a minor part of almost all zircon grains (Electronic Supplementary Appendices 5 & 8).

In all samples, mantles of Cl-moderate to CL-dark intensity are found that have overgrown cores of igneous zircon (Figs. 8a,b,c,e,h; Electronic Supplementary Appendices 5 & 8). This generation of zircon lacks the strong planar or oscillatory zoning characteristic of igneous cores; instead, gradated, simple concentric, and sector zoning is typical. In many grains from some samples (especially 23, 24, 28, and 29), this is the predominant form of zircon (e.g. Figs. 8d,h). As with similar mantles and cores observed in zircon from the CGF zone samples, this generation of zircon is interpreted as having grown during high-grade metamorphism.

In all samples from the SGF zone, most zircon grains have rims of CL-bright intensity (Electronic Supplementary Appendices 5 & 8). The thickness of these rims relative to mantles and cores of relatively CL-dark intensity varies within and between samples from very thin (Figs. 8a,d) to thick (Figs. 8b,c,e), and a few large grains in some samples consist entirely of CL-bright zircon (Fig. 8c). In separates from samples 21, 23, 27, and 28, most grains are predominantly composed of CL-bright zircon. On prismatic grains, CL-bright rim growth is most developed on rounded terminations (Fig. 8e). Interfaces of CL-bright rims with mantles and cores of CL-moderate to CL-bright zircon are rounded and embayed, truncating growth zoning in the latter (Figs. 8b,c,h,i). Internal compositional zoning, as indicated by variations in BSE and CL brightness, tends to be weak or absent, but where present includes simple, rounded, planar, sector (Fig. 8f), and fir-tree (Fig. 8g) growth zoning. The latter textures imply rapid growth in an environment with a good Zr supply (Corfu *et al.*, 2003). The relationship of CL-bright rims with CL-dark mantles and cores is attributed to a distinct generation of zircon growth under high-grade metamorphic conditions.

In polished thin sections, CL-dark and CL-bright generations of mantles and rims have similar relationships to metamorphic assemblages as observed in samples from the CGF zone (Electronic

Supplementary Appendix 8). However, zircon grains in samples from the SGF zone tend to be larger with greater development of CL-bright rims, especially within and adjacent to felsic phases such as quartz, plagioclase, and K-feldspar (e.g. Fig. 8g). Where zircon grains are found in association with mafic phases such as ilmenite, amphibole, clinopyroxene, and orthopyroxene, CL-dark mantles may be well-developed, but CL-bright rims tend to be thin, especially where zircon grains occur as inclusions in Ti-rich amphibole (Fig. 8h) and orthopyroxene (Fig. 8i). However, such thin rims are always present in such inclusions, suggesting that CL-bright zircon growth is synchronous with orthopyroxene and amphibole growth.

In summary, all samples from north to south along the traverse contain zircon grains that preserve, to varying degrees, cores of magmatic zircon, which formed either in the igneous protoliths of the gneisses, or are present as xenocrystic or detrital materials (Table 1; Figs. 2, 6–8; Electronic Supplementary Appendices 5 & 8). These cores have been partially dissolved and overgrown by multiple generations of zircon that grew during high-grade metamorphism. In the northern-most samples of the amphibolite-grade felsic orthogneiss (NAF), the rims of the metamorphic zircon tend to have a lower CL signal than the protolith zircon. Further south along the traverse (CGF and SGF), two generations of metamorphic zircon are observed in samples of felsic pyroxene granulite (or charnockite), which consist of overgrowths of moderate to CL-dark zircon subsequently overgrown by rims of CL-bright metamorphic zircon. There is generally, from north to south, a decrease in the proportion of protolith zircon and an increase in the proportion of both generations of metamorphic zircon. Although not as systematic, the relative amount of CL-moderate to CL-dark metamorphic zircon compared to CL-bright metamorphic zircon decreases as a function of increasing metamorphic grade from the CGF into the SGF zone.

GEOCHRONOLOGY

In this section, a summarised version of ion microprobe geochronology for zircon and titanite is provided. Analytical results for zircon are presented with examples in Table 3 and in full in

Electronic Supplementary Appendix 4. Analytical results for titanite are provided in Table 4. A detailed, sample by sample presentation of SHRIMP-II age and U-Th data is provided in Electronic Supplementary Appendix 9. Spot $^{207}Pb/^{206}Pb$ ages, U contents, and Th/U values are also provided on zircon CL images, with representative examples in Figs. 6 through 8; and on CL images for each sample in Electronic Supplementary Appendix 5 to show relationships between spot ages and internal textures. Age data for all 29 samples, along with calculated ages for each type of zircon, and inset plots with Th/U and U contents, are provided in Figure 9.

In order to obtain age estimates for the timing of zircon growth, statistical analysis was applied to pooled ^{204}Pb-corrected $^{207}Pb/^{206}Pb$ ages for each growth type as identified from CL observations. All weighted mean ages with 95% confidence errors are provided on Tera-Wasserburg concordia plots in Figure 9, along with Th and U inset plots for each analysis. Weighted means were obtained for pooled $^{207}Pb/^{206}Pb$ ages with a > 0.05 probability of equivalence. Where outliers were identified and excluded from pooled analysis, data are noted in the form 'n/m data', signifying that 'n' data were selected for the weighted mean age from 'm' data. Generally, $^{207}Pb/^{206}Pb$ age outliers for each growth type are attributed to isotopic disturbance during metamorphism or recent weathering, or to analytical spots that overlap older and younger zircon components. Where data are too scattered to define a weighted mean age, a range of $^{207}Pb/^{206}Pb$ ages is presented instead (e.g. Figs 9(25) & 9(26)). Weighted mean $^{207}Pb/^{206}Pb$ age estimates for generations of zircon and titanite growth, where calculated, are summarised in Table 5 and plotted along the Shevaroy Block traverse in Figure 10. The majority of the twenty-nine samples analysed yielded magmatic zircon ages between ca. 2591 Ma and 2540 Ma. Samples 16, 19, 21, and 28 yielded zircon ages that are scattered but consistent with magmatism within the same (late Neoarchean) period (Fig. 9). There is no systematic variation between protolith age and position along the N-S traverse. Older pooled and intercept ages from samples 6, 14, 17 (ca. 2700 Ma), and 15 (ca. 3360 Ma) (Fig. 9) represent older TTG granitoid protoliths, although a xenocrystic origin from source rocks of late Archean anatexis and magmatism cannot be completely ruled out.

Around half of the 23 samples with 2600 to 2550 Ma magmatic protoliths contain xenocrystic zircons, indicating a substantial amount of crustal reworking in this period. Three samples (22, 25, and 26) (Fig. 9) have zircon cores with scattered ages consistent with sedimentary protoliths. Core ages scatter downwards to overlap post-2600 Ma magmatic and metamorphic ages, consistent with deposition immediately before metamorphism. However, the possible disturbance of these age data by metamorphism makes this a tentative interpretation.

Zircon mantles and rims can be generally distinguished between those that contain more U than the magmatic grain cores (hereafter called U-enriched); those with comparable U (U-undepleted), and those with less U than grain cores (U-depleted). This is most clearly demonstrated in the Th/U vs. U plots for each sample provided with the Concordia plots in Figure 9. Uranium-enriched rims are found in samples 1 – 4 from the NAF zone (Figs. 6 & 9(1)–9(4)), with weighted mean ages varying between 2548 Ma and 2515 Ma (Fig. 10). Further south, only sample 13 yielded U-enriched zircon as mantles with a weighted mean age of 2539 Ma (Fig 9(13)). Other samples contain zircon with a few U-enriched mantles and patches, but without consistent ages. The majority of samples in the CGF and SGF zones yielded distinct U-undepleted cores and mantles with overgrowth relationships to the magmatic cores and a lack of oscillatory zoning commonly observed in fractionating magmas (Figs. 7, 8 & 9). Of these samples, seven yielded weighted mean ages for U-undepleted zircon between 2548 Ma and 2532 Ma (Fig. 9), with a seven sample weighted mean that scatters slightly beyond equivalence (2542.1 ± 4.0 Ma, MSWD = 2.0) (Fig. 10). Both U-enriched and U-depleted generations of zircon growth are attributed to metamorphism, mostly at ca. 2540 Ma.

A U-depleted generation of zircon growth, present as rims on U-undepleted metamorphic zircon and magmatic zircon cores, is present in almost all samples from the CGF and SGF zones of the traverse. Weighted mean ages were obtained for most samples with U-depleted zircon that range between ca. 2534 Ma and 2495 Ma (Table 5; Figs. 9 & 10; Electronic Supplementary Appendix 4). The mean ages are non-equivalent, but together provide a robust weighted mean age of 2511.3 ± 5.1

Ma. Although there is no systematic variation in mean ages for U-depleted zircon along the traverse, most from samples in the northern half of the traverse are older than most in the southern half (Fig. 10). Eleven samples from the northern half (5, 7, and 9–17; Figs. 9 & 10) yield a weighted mean age of 2519.4 ± 5.4 Ma (n = 11, MSWD = 2.6), whereas eleven samples from the southern half of the traverse (18–29; Figs. 9 & 10), excluding sample 26, yield a weighted mean age of 2503.9 ± 4.8 Ma (n = 11, MSWD = 1.6) (Tables 3 & 5; Figs. 9 & 10). Both estimates are in turn significantly younger than the mean age of U-undepleted zircon. As in the case of U-undepleted rims, the U-depleted zircon is attributed to growth or modification during metamorphism. The progression in mean ages between U-undepleted zircon at ca. 2540 Ma, through U-depleted zircon at ca. 2519 Ma, to U-depleted zircon in the southern part of the traverse at ca. 2504 Ma (Fig. 10), demonstrates that metamorphic zircon was produced over a 40 million year window, with increasing depletion of U from zircon over that time interval. The significance of this, and of the scatter between ages in each type of zircon growth, will be discussed below.

Titanite from three samples (2, 4, 5) (Table 4; Fig. 9) from the NAF zone of the Shevaroy traverse was identified in grain separate mounts as fragments up to 200 microns across. Under CL imaging, they lack internal compositional variations that would be visible in BSE images. Results for SHRIMP dating of titanite are presented on Tera-Wasserburg concordia plots in Figures 9(2), 9(4), and 9(5) along with the zircon results. Most of the scatter in the U-Pb ratios, visible in the concordia plots, is attributed to imprecision in the estimation of common Pb contents from ^{204}Pb, which has little effect on ^{207}Pb/^{206}Pb ages beyond a reduction in precision. Analyses that have low precision are poor in U, however this does not affect the validity of the measurement. Weighted mean ^{207}Pb/^{206}Pb ages were obtained of ca. 2496 Ma, ca. 2502 Ma, and ca. 2501 Ma for samples 2, 4, and 5, respectively (Figs. 9(2), 9(4), & 9(5)). These ages are slightly yet consistently younger than those for metamorphic zircon growth in the same samples. Since titanite rims overgrow ilmenite that co-exists with zircon in a granoblastic fabric (see Electronic Supplementary Appendix 2; Fig. A3(h)), the titanite ages may indicate the timing of this reaction; alternatively, they may represent closure temperatures (Fig. 6g), through cooling after amphibolite-grade metamorphism in the NAF.

ZIRCON GEOCHEMISTRY

The division of zircon growth into magmatic and metamorphic generations (the latter with U-enriched, U-undepleted, and U-depleted types) allows for geochemical comparisons to be made between these generations across all samples (Table 3; Figs 11 & 12; Electronic Supplementary Appendices 4 & 6). It is important to note here that the definition of 'enriched', 'undepleted', and 'depleted' here is between zircon in individual grains and the magmatic cores of those grains, rather than between zircon as a whole in all samples. Such variation has been demonstrated at the grain level in the CL images of zircon grains (Figs. 6 – 8; Electronic Supplementary Appendices 5 & 8), and on the sample level in the Concordia and Th-U plots in Figure 9. Since there is commonly significant variation in U between magmatic cores in a single sample, as well as between samples, it should not be taken for granted that broader systematic variations are present. In order to relate the chemical changes seen in metamorphic zircon to those observed between samples of differing metamorphic grade along the traverse, a broader view is required.

In Figure 11, the zircon and whole rock U and Th content, and U/Th ratio are plotted along the sample traverse in order to investigate variations in trace element geochemistry with metamorphic grade. In the whole-rock U and Th content, there is a decreasing trend from the NAF to the CGF zones, which flattens out between the CGF and SGF zones (Figs. 4e,f). These trends are not present in magmatic zircon, which shows no systematic variation along the traverse. Although there are differences between the U and Th contents in each of the generations of metamorphic zircon (i.e. U-enriched, U-undepleted, and U-depleted), there are no systematic trends within each type (Fig. 11). This is reflected in the lack of trends in Th/U values along the traverse for each generation of zircon. Assuming that zircon is the main host for U and Th in the samples, which do not contain free monazite grains, the depletion trend in whole-rock U and Th along the traverse reflects an increase in the proportion of U-depleted zircon from north to south (Figs. 4e, 4f, & 11).

For a total of 760 age analyses, U and Th data are plotted by generation in Figure 12a. All data from magmatic zircon > 2600 Ma are grouped along with xenocrystic and possible detrital zircon data. The magmatic zircon with ages < 2600 Ma (mostly ca. 2550 Ma) has scattered compositions, with U between 50 and 2000 ppm and Th/U values between 0.003 and 3. Within the 67% contour or 2/3 of the data (shaded areas), U varies between 100 and 1000 ppm U, with Th/U values between 0.2 and 2. Analyses of U-enriched metamorphic zircon (from samples 1 – 4 of the NAF zone; Figs. 9(1) – 9(4)) scatter between 200 and 4000 ppm U, with Th/U values between 0.002 and 0.7, but are concentrated within the 67% contour between 300 and 2000 ppm U, with Th/U values between 0.04 and 0.3. Compared with magmatic zircon, U-enriched metamorphic zircon has mostly lower Th/U values. However, the difference is not consistent within or between samples, and there is no coupled depletion of Th with U enrichment.

Analyses of U-undepleted metamorphic zircon from the CGF and SGF (including sample 13; Fig. 9(13)) have U values between 100 and 3000 ppm U, with Th/U values between 0.01 and 2, but are concentrated within the 67% contour between 100 and 800 ppm U, with Th/U values between 0.1 and 2 (Fig. 12a). Most analyses overlap in both the U and Th content with magmatic zircon. This is in contrast with U-depleted metamorphic zircon, which varies between 5 and 300 ppm U, (with Th/U values between 0.1 and 8), and is concentrated within the 67% contour between 20 and 200 ppm U, with Th/U values between 0.6 and 5 (Fig. 12a). Most U-depleted metamorphic zircon analyses have higher Th/U values than magmatic and U-undepleted metamorphic zircon. Although U depletion is consistent, Th depletion is highly variable within and between samples.

In terms of REE content, differences between magmatic zircon and the different types of metamorphic zircon are clearly distinguishable. Plotting Yb vs. U shows overlapping fields (Fig. 12b); however although the U-enriched has a similar range in Yb content for magmatic zircon from the same sample, U-undepleted and U-depleted zircon are variably lower. This variability can also be seen in the REE spider plots (Figs. 12c,d,e). In general, U enriched metamorphic zircon (Fig. 12c) is more variable than what is seen for igneous zircon. In contrast, the HREE content in U-undepleted (Fig. 12d) and U-depleted (Fig. 12e) metamorphic zircon tends towards lower concentrations compared to the magmatic zircon, being more pronounced in the U-depleted zircon.

DISCUSSION

Zircon as a recorder of geochemical change

If the response of pre-existing zircon to different metamorphic conditions in the north and south of the traverse can be observed (Figs. 6–9), then the same may be true for zircon with early and late stages of metamorphic growth, especially in the higher-grade samples. At the same time, depletion in whole-rock trace elements, such as Rb, Cs, U, and Th (Fig. 4), could be seen as a proxy for the changes that occurred during metamorphism.

In general, direct evidence for such changes in the granulite-facies rocks from the CGF and SGF, especially during prograde or peak metamorphism, is typically scant. This is due to the relatively efficient formation of mineral parageneses, especially where aids to recrystallization and mineral growth, such as strain, fluids, and high-temperature diffusion, operate. Zircon, as a resistant yet chemically reactive accessory phase, commonly preserves domains within grains unaffected by high-temperature metamorphism, along with domains grown or modified during metamorphism. Such domains can usually be distinguished by a combination of textural observations of internal structures (delineated by changes in chemical composition), chemical signatures (especially in U and Th contents), and measurement of radiogenic isotopes (to distinguish generations of zircon formation over time). As such, zircon provides another proxy for charting chemical changes during metamorphism, and is often the only mineral to possess domains that unequivocally preserve chemical signatures from protoliths. Such a proxy is innately a partial one, as zircon concentrates elements that typically occur in only trace amounts, and shares these elements with a variety of accessory minerals that also concentrate them, along with major phases that accommodate small amounts of trace elements.

Pre-metamorphic zircon chemistry

The cores of zircon grains, present in the protoliths, were identified by differences in age (older than ca. 2540 Ma) and by the presence of oscillatory zoning, a feature characteristic of zircon growth in granitoid magmas where the supply of trace elements to growing crystal faces undergoes sudden and repeated changes due to magma viscosity, mixing, and fractional crystallisation (Hoskin & Schaltegger, 2003). Beyond the interpretation that this type of zircon is pre-metamorphic, there is an inherent ambiguity in relating these domains to protolith chemistry. In the case of felsic TTG orthogneisses, they may have grown with the crystallisation of the magmatic protolith. However, it is also possible that such zircon is xenocrystic, having been inherited from the source rocks of crustally-derived magmas or from the assimilation of country rock.

In the Shevaroy Block, most samples contained zircon with cores that preserve igneous growth zoning, with weighted mean ages that represent the timing of the crystallisation of magmatic protoliths (Fig. 9). Of these, nineteen samples have protolith ages younger than 2600 Ma (Table 3; Figs. 9 & 10), indicating a widespread TTG magmatism after 2600 Ma. The presence of older crust is also demonstrated by samples 6, 14, 15, and 17, in which the zircon cores indicate magmatism between ca. 2700 and 3400 Ma (Table 3; Figs. 9 & 10).

Since the magmatic zircon domains are pre-metamorphic, they provide information about the chemistry of the magmatic protoliths not available from other minerals or from whole-rock chemistry. The high variability of trace element contents reflects both the differing origins of the magmas and the changes that occurred as granitic magmas evolved during crystallisation. In some samples, there are positive correlations between trace element contents, such as Th and U in samples 2 and 27 (Table 3; Fig. 9), which may be attributed to growth in a fractionally crystallising magma. In other samples, such correlations are not apparent, probably due to a more complex interplay between the evolving magma and other significant hosts of Th and U, such as monazite, allanite, and titanite. Although the majority of data from magmatic zircon have Th/U values above 0.2 (Table 3; Figs. 9 & 12a), there are numerous exceptions that demonstrate that this value alone is a weak criterion for distinguishing between magmatic and metamorphic zircon. The lack of systematic depletion in actinides in zircon between samples contrasts with that seen in whole rock chemistry along the traverse (Fig. 4; see also Hansen & Harlov, (2007) their figs. 2, 3, & 4). Consequently, this can be taken as indicating that such depletion was not inherent to the protoliths, but instead is a product of metamorphism.

Zircon chemistry during metamorphism

Zircon mantles, rims, and neoblastic grains, formed during metamorphism, were identified by the relative lack of features commonly ascribed to zircon growing in fractionally crystallising TTG magmas, in particular euhedral, oscillatory growth zones. This does not exclude the possibility that such zircon could have grown in the presence of a melt, which is attested to by migmatitic textures seen in the NAF (see field descriptions above; Fig. 2). The spread in age data between ca. 2540 and 2500 Ma (Figs. 9 & 10) suggests that metamorphism began shortly after the emplacement of TTG protoliths at ca. 2550 Ma, and progressed over a period not shorter than 40 m.y.. The presence of titanite in samples from the NAF with ages that average at ca. 2500 Ma (Figs. 9 & 10), and are therefore younger than metamorphic zircon in the same samples, indicates that cooling from peak metamorphic temperatures was occurring by this time. These titanite ages, however, overlap ages of zircon growth in higher-grade granulites further south (e.g. Clark et al. 2009) indicating that peak metamorphism and cooling was not synchronous over the region. The important factor here is the chemical difference between this late-grown zircon and older metamorphic zircon, as it allows us to track chemical changes in the granulites from protolith to metamorphic product as a function of time.

In most samples from the NAF, as well as in zircon mantles from sample 13 in the CGF, metamorphic zircon is enriched in U relative to the magmatic cores (Table 3; Figs. 9, 11, & 12a). The presence of other actinide and REE-bearing metamorphic phases at the transition between the CGF and NAF and in the NAF gneisses, especially monazite, allanite, and titanite, implies that exchange of U and Th between these phases played a role in changing the zircon chemistry (cf. Table 1).

With the exception of sample 13 (Figs. 7c & 9(13)), metamorphic zircon in granulite-grade rocks from the CGF and SGF does not show U enrichment; instead, many samples have mantles of metamorphic zircon that are undepleted in U relative to the cores of each sample, and all have rims that overgrow and replace magmatic zircon with varying degrees of U depletion. The degree of depletion generally increases outwards, indicating changes in the availability of U as zircon grew, either continuously or intermittently. Since these samples from the CGF and SGF generally lack monazite (cf. Table 1), except as minute inclusions in apatite, it is likely that the growth of U depleted zircon occurred after the breakdown of any pre-existing monazite in the protoliths. Ages from U-undepleted metamorphic zircon are significantly older than from most U-depleted zircon, which demonstrates that metamorphism has progressed over a ca. 40 m.y. period (Table 3; Fig. 10). Depletion in U and, less systematically, Th (Figs. 10 & 11), corresponds to similar depletions in whole-rock chemistry (Figs. 4e,f), so that zircon records the loss of these elements from the host rocks over the period of high-grade metamorphism.

These changes are reflected in the element ratios, so that U-depleted metamorphic zircon tends to have higher Th/U values than the U-undepleted metamorphic and magmatic zircon (Fig. 12a). This is consistent with the observed disappearance of monazite, allanite, and titanite from the mineral assemblage in the granulite-facies rocks below the clinopyroxene-rich transition zone (orthopyroxene-in isograd) (Hansen & Harlov, 2007; see above), as these phases partition Th more strongly than U relative to zircon. Whole-rock normalised values of Th/U from magmatic, U-undepleted metamorphic, and U-depleted metamorphic zircon broadly overlap (Fig. 12a,b). It has been widely assumed that metamorphic zircon has significantly lower Th/U values (generally < 0.2) than magmatic zircon (e.g. Hoskin & Schaltegger, 2003; Yakymchuk *et al.*, 2018). However, this study is another example of how this is not always the case. It is possible for a single sample of granulite-facies rock (e.g., sample 13; Figs. 7c & 9(13)) to exhibit both increases and decreases of the Th/U ratio in metamorphic zircon relative to protolith zircon, depending on the changes that metamorphism causes to the chemistry of the rock.

During granulite- and amphibolite-facies metamorphism along the traverse, the zircon encountered either felsic melts or high-grade fluids, or a mixture of both, along mineral grain boundaries. Whatever the case, the H_2O activity of these melts and/or fluids during granulite-grade metamorphism must have been low enough such that orthopyroxene was a stable phase whereas in the amphibolite-grade rocks the H_2O activity and temperature were outside the orthopyroxene stability field. In order to ascertain the most likely fluid and/or melt scenario occurring during the metamorphism of this cross-section of lower late Archean crust that best fits the zircon data and previous studies of the oxide, sulfide, silicate, and accessory minerals in these rocks (Harlov *et al.*, 1997, 1998; Harlov & Hansen, 2005; Hansen & Harlov, 2007), it is necessary to first explore what field observations coupled with the mineralogy of these samples can tell us.

Regional metamorphism along the traverse: partial melting vs. solid state dehydration

Whereas the granulites of the CGF do show evidence of partial melting, especially with the production of small granite plutons scattered throughout the clinopyroxene zone straddling the orthopyroxene-in isograd (Fig. 2), in the higher grade SGF the uniformly dark colour in most outcrops obscures the contrast between rock types and makes it hard to identify migmatitic structures. However coarser grained veins and patches in quartzo-feldspathic gneisses and quartzo-feldspathic veins and patches within mafic granulites could be interpreted as partial melts. If anatexis, in a system closed to everything except melt migration, was the main process of dehydration in this terrain, then orthopyroxene and clinopyroxene would be the solid product of peritectic melting reactions of biotite or amphibole in which the water ended up in the melt. During the crystallization of these melts the peritectic reactions should run in reverse and the pyroxenes should revert back at least partially to amphibole or biotite. One way to prevent this would be to separate the melt from the residual solids. However, the orthopyroxene +/- clinopyroxene can sometimes occur in veins and patches (see above), which could be presumed to be crystallized melt. As this melt crystallizes, H_2O from the melt should react with the orthopyroxene or clinopyroxene grain rim forming a continuous reaction rim of biotite or amphibole, respectively, which would protect the interior of the grain from further reaction. Such continuous reaction rims around orthopyroxene and clinopyroxene grain cores do occur in the melt portions of high-grade migmatites (Hansen *et al.*, 2015). However, such reaction rims were not observed around orthopyroxene or clinopyroxene grains in the quartzo-feldspathic veins in the rocks from the SGF. This leaves a key unanswered question: if partial melting in a system closed to everything except melt migration was responsible for the dehydration of the SGF, how was the water removed from the melt in these localized examples? This would lend argument to the proposition that pervasive low H_2O fluids moving along grain boundaries in an open system were responsible for removing the H_2O from the system during granulite-facies metamorphism as opposed to partial melts (see arguments laid out in Newton *et al.* (2014) and Aranovich (2017) and references therein).

A lack of field evidence for the direct removal of H_2O by partial melts, a low estimated H_2O activity of around 0.2, and a lack of biotite and amphibole reaction textures surrounding the pyroxenes all support the presence of H_2O-poor fluids along grain boundaries in the granulite-facies rocks of the SGF and CGF. One of these fluids definitely was CO_2 due to the presence of CO_2-rich fluid inclusions in both these rocks (see above) and in similar high-grade charnockitic rocks (both metamorphic and igneous) world-wide (cf. Touret & Nijland, 2013). However, the high wetting angle of CO_2 makes it incapable of flow along grain boundaries during high grade metamorphism, which leads to it being easily trapped in fluid inclusions (Watson & Brenan, 1987; Brenan & Watson, 1988; Holness & Graham, 1991; Holness, 1992, 1997; Gibert *et al.*, 1998). Hence the presence of CO_2-rich fluid inclusions in metamorphic charnockite from high-grade terrains appears to be due almost entirely to preferential trapping and is not an indication of relative abundance. Per the extant experimental solubility data, CO_2 is also a poor fluid to effect the mass transfer of elements commonly found in silicate, oxide, sulfide, and phosphate minerals in granitoid rocks under high-grade metamorphic conditions (cf. Novgorodov, 1977; Newton & Manning, 2000). Any fluid present would need to be mobile enough to easily flow along grain boundaries without being trapped; be able to effect mass transfer of elements common to silicate, oxide, sulfide, and phosphate minerals; and, in an open system, be both constantly removed and constantly replenished such that it could take away the H_2O, resulting from the conversion of biotites and amphiboles to orthopyroxene and clinopyroxene, out of the system, while at the same time maintain the low H_2O activity necessary to allow orthopyroxene to remain a stable phase.

Hypersaline fluids have been proposed as the most likely fluid to accomplish this function during high-grade metamorphism (cf. Newton *et al.*, 2014; Manning & Aranovich, 2014; Aranovich *et al.*, 2014, 2016; Aranovich, 2017; Manning, 2018). Saline and hypersaline fluids move easily along grain boundaries due to their low wetting angle (Gibert *et al.*, 1998) making them very difficult to trap as fluid inclusions though their rare occurrence as primary fluid inclusions has been documented in a series of granulite-facies, orthopyroxene-bearing TTG rocks (Touret & Nijland, 2013). In addition, due to its large size, only minor amounts of Cl can be incorporated into few common granitoid minerals, such as biotite and apatite, and then only under special conditions (Mi & Pan, 2018). Hence, other than careful fluid inclusion work, evidence for the presence of saline or hypersaline fluids in these rocks is generally hard to document. However, most minerals, including $CaCO_3$ (Newton & Manning, 2002), show at least some solubility if not a relatively high solubility in NaCl and KCl saline and hypersaline fluids under granulite grade P-T conditions (e.g. Newton & Manning, 2000, 2005, 2006, 2007; Shmulovich *et al.*, 2001; Audetat & Keppler, 2005; Antignano & Manning, 2008; Tropper *et al.*, 2011, 2013; Tanis *et al.*, 2016; see summation in Harlov & Aranovich, 2018) indicating that such fluids would be capable of promoting extensive mass transfer.

Aranovich & Newton (1996, 1997, 1998) have experimentally demonstrated that the activity of H_2O in NaCl-bearing saline and hypersaline fluids approaches X_{H2O}^2 at pressures above 400 to 500 MPa over the temperature range of the experiments (600 – 900 °C) implying that even high values of X_{H2O} in saline fluids would still give relatively low H_2O activities under granulite-facies P-T conditions. This particular characteristic of hypersaline fluids at high pressures is reflected in the pseudo-section modelling outlined in Figures 5a and 5c for sample 93 F9 F8 (see also Electronic Supplementary Appendix 7c). Here for estimated biotite-quartz-K-feldspar-orthopyroxene H_2O activities of 0.18 to 0.24, the presence of hypersaline fluids would imply that X_{H2O} = 0.5 to 0.4, which would correspond approximately to X_{NaCl} = 0.5 and X_{CO2} = 0.1 (Fig. 5a), and to X_{NaCl} = 0.4 and X_{CO2} = 0.1 (Fig. 5c), respectively. At 800 MPa, the presence of these fluids extends the solidus to around 900 to 920 °C compared to the solidus (780 – 800 °C) for a saline-absent fluid with the same fraction of CO_2, (cf. Electronic Supplementary Appendix 7c). If fluids consisting only of CO_2-H_2O are taken into account, the low estimated H_2O activities also indicate low X_{H2O} fractions in this system as well of 0.1 to 0.14 (Aranovich & Newton, 1999), which result in solidus temperatures similar to that found for the NaCl-H_2O-CO_2 system (Figs. 5b,d). The higher solidus temperatures estimated for either system at 800 MPa are well above an estimated peak regional temperature of 800 to 850 °C. This implies that no melting should have occurred during granulite-facies metamorphism in those sections of the Shevaroy traverse with pressures above 400 to 500 MPa no matter which of the two fluid systems was present, which agrees with natural observation.

Origins and high-grade metamorphism of the Shevaroy Block

The Shevaroy Block consists of a composite of magmatic components similar in age and whole-rock chemistry to those from the East and Central Dharwar Craton. These include scarce remnants of meso-Archean TTG granitoids, ca. 2700 Ma magmatic rocks, metasediments, and predominantly 2570 to 2550 Ma deformed granitoids (TTG and granitic orthogneisses) (Gireesh *et al.*, 2012). The presence of protoliths as old as ca. 3400 Ma (sample 15; Figs. 7d & 9(15)) suggest an origin for the crustal components of the Shevaroy Block similar to that of the Central Dharwar Craton (Peucat *et al.*, 2013; Glorie *et al.*, 2014; Maibam *et al.*, 2016). It is unclear what proportion of the 2550 Ma TTG granitoids originated from reworked pre-existing crust; however the high number of samples containing xenocrystic zircon (samples 1, 4, 5, 8, 10, 12, 15, 17, 20, 21, 22, 25, & 26; Fig. 9) suggests that a significant portion of these TTG granitoids include older components from the Dharwar Craton.

Dating of the zircon rims indicates that high-grade metamorphism occurred at 2500 Ma some 40 to 50 Ma after granitoid emplacement (Figs. 9 & 10), concurrent with (1) the metasomatic modification of igneous zircon (magmatic, detrital, and xenocrystic) (Figs. 6 – 8; Electronic Supplementary Appendices 5 & 8); (2) the imposition of a high oxidation and sulfidation state on the original protolith (Electronic Supplementary Appendix 2; Harlov *et al.*, 1997; Harlov & Hansen, 2005); (3) the conversion of biotite and amphibole to orthopyroxene and clinopyroxene; (4) the formation of K-feldspar reaction rims and micro-veins along quartz and plagioclase grain boundaries (Harlov et al., 1998; Hansen & Harlov, 2007); and (5) the metasomatic alteration of fluorapatite and monazite coupled with the subsequent production of monazite inclusions in fluorapatite, titanite rims around ilmenite, and allanite rims around monazite and fluorapatite (Hansen & Harlov, 2007).

The most likely origin of the TTG granitoid protoliths in the Shevaroy Block was probably related to a subduction event in an island arc type setting (see Chapter 5 in Arndt (2013)) similar to what has been suggested for the ca. 2500 Ma Nilgiri Massif (Samuel *et al.*, 2019), although plume-type models for tectonothermal activity have also been proposed (Jayananda *et al.*, 2018, and references therein). In such a scenario, devolitisation of sediments, altered oceanic basalt, and hydrated peridotite associated with or making up the subducting oceanic plate, peaks at around 100 km depth. This results in fluids that rise upwards into the overlying mantle wedge where they induce flux melting of peridotite at depths of around 80 km, the end product of which is a volatile-rich, Mg-rich basaltic magma. These volatile-rich magmas rise upwards to pond at the base of the crust where they undergo a complex series of processes including mixing, assimilation of earlier crustal felsic rocks, storage, and homogenisation. This leads to the initial production of evolved felsic magmas, which ascend into the lower crust as TTG granitoid plutons and crystallize, while a residual, denser, ultramafic residue is left behind at the base of the continental crust. Such a picture fits in well with the origins of igneous zircon in rocks from the Shevaroy Block since assimilation of older, pre-existing granitoid crustal material during emplacement of these late Archean plutons would account for the presence of the detrital and xenocrystic zircons.

Continued pulses of volatile-rich, basaltic magma ponding at the base of the continental crust interacting with this ultramafic residue and crystallizing *in situ* could then act as a source of both heat and fluids during granulite-grade metamorphism of the now crystalline TTG granitoids emplaced above them. (Bohlen & Mezger, 1989; Lowenstern, 2000; Manning, 2004; Wallace, 2005; Newton *et al.*, 2014; Zellmer *et al.*, 2015). Age data from the magmatic zircon cores suggest that granitoid emplacement took place between 2591 Ma and 2540 Ma (see above). Within 40 to 50 million years after emplacement and crystallization, these TTG granitoid intrusions were metamorphosed by the rising heat and fluids given off by these crystallizing underplating basaltic magmas. Relatively uniform metamorphic zircon rim ages, whether U-enriched or U-depleted, ranging from 2530 to 2500 Ma, supports this scenario despite whether the zircon had a magmatic, xenocrystic, or detrital origin.

Basaltic underplating at the base of the continental crust (Rudnick & Jackson, 1995) has been conjectured to be one of the principal heat sources responsible for granulite-grade metamorphism as opposed to deep burial (Furlong & Fountain, 1986; O'Reilly *et al.*, 1988; Bergantz, 1989; Bohlen & Mezger, 1989; Parsons *et al.*, 1992; Petford & Gallagher, 2001; Thybo & Artemieva, 2013; Hao *et al.*, 2016). Evidence for a mafic heat/fluid source and associated granulite-facies metamorphism is seen today in the Val Strona traverse located in the Ivrea-Verbano Zone, northern Italy, where it is preserved intact as the Mafic Formation in direct contact with the granulite-facies rocks (Harlov & Förster, 2002a,b). Both rock types have approximately the same age range, though there is still some uncertainty in the exact timing of the two events (Peressini *et al.*, 2007; Guergouz *et al.*, 2018). The volatiles present in the underplating basalts would be subduction-related and consist primarily of H_2O, CO_2, and NaCl-dominated saline fluids with a Ca, K, and S component (Hansteen & Gurenko, 1998; Webster *et al.*, 1999; Alletti *et al.*, 2009; Lesne *et al.*, 2011a,b; Witham *et al.*, 2012; Filiberto *et al.*, 2014; Walters *et al.*, 2019). The source of these fluids would have been from the fore-arc crustal sediments incorporated into the mantle wedge by fore-arc subduction erosion towards the end of arc magmatism. Such a temporal change in the subducted sediment component in a constant mantle source has been reported from present-day Marianas- and Aleutian-type island arc magmas during the waning stages of island arc magmatism (Plank, 2005; Kay *et al.*, 2019). In support of the scenario outlined above, current geophysical studies have indicated that there are areas of the lower crust, especially those associated with subduction zones, which show an anomalously high conductivity that could be ascribed to the presence of high salinity fluids in an interconnected porosity as opposed to partial melts due to the fact that the local geotherms are insufficient for melt production (Unsworth & Rondenay, 2012; Manning, 2018; see also Connolly & Podladchokov, 2012).

Both natural observation of basaltic rocks associated with subduction zones and experiments involving the incorporation of volatiles into basaltic melts under high pressure and temperature indicate that such melts can contain up to ~4 wt% H_2O (Lesne *et al.*, 2011a; Plank *et al.*, 2013), up to 1500 ppm CO_2 (Lesne *et al.*, 2011b), up to 3 to 4 wt% Cl (primarily as NaCl with lesser amounts of KCl and $CaCl_2$) (Webster *et al.*, 1999, 2015; Lesne *et al.*, 2011a; Thomas & Wood, 2022), and up to 2000 to 3000 ppm S (Mathez, 1976; Lesne *et al.*, 2011a). The S would occur in an oxidized form as SO_3 since most of the S would likely have originated from subducted $CaSO_4$-bearing oceanic sediments (Grotzinger & Kasting, 1993). In addition to a high solubility in basaltic melts (Mathez, 1976; O'Neill & Mavrogenes, 2002; Jugo *et al.*, 2005; Metrich *et al.*, 2009; Metrich & Mandeville, 2010; Morizet *et al.*, 2010; de Moor *et al.*, 2013; Plank *et al.*, 2013), $CaSO_4$ has been shown to have a high solubility in saline to hypersaline fluids at high P-T as opposed to CO_2 (Newton & Manning, 2005).

During the crystallization of the underplating basaltic magma, these volatiles would have been expelled as a fluid or fluids and subsequently risen upwards into the lower crust. The H_2O, CO_2, and NaCl content of the underplating basalt implies that the two principal fluids expelled during crystallization would have consisted of a saline to hypersaline fluid dominated by NaCl with an SO_3 component and a very minor CO_2 component and a CO_2-rich fluid with a very minor saline fluid component (Johnson, 1991; Heinrich, 2007; Manning, 2018). The CO_2-rich fluid would preferentially be trapped as fluid inclusions whereas the hypersaline fluid would flow upwards along grain boundaries up the rock column. In addition to helping effect mass transfer, the relatively high heat capacity of the H_2O component in the hypersaline fluid would also allow it to serve as a means of efficient heat transport into the lower crust thereby helping to facilitate granulite-grade metamorphism throughout the lower crust.

Per the evidence contained in the pseudo-section plots in Figure 5 (see also Electronic Supplementary Appendix 7c) and the discussion above, infiltration of low H_2O activity, NaCl-dominated hypersaline fluids with an SO_3 component into the TTG granitoids of the late Archean lower crust would not have caused partial melting but rather would have imposed a fluid-aided *in situ* solid-state conversion of biotite and amphibole into orthopyroxene +/- clinopyroxene at 800 – 850 °C and 800 MPa via the following reactions:

$$K(Fe,Mg)_3AlSi_3O_{10}(OH)_2 + 3\ SiO_2 = 3\ (Fe,Mg)SiO_3 + KAlSi_3O_8 + H_2O \qquad (1)$$

and

$$(Na, K)Ca_2(Fe,Mg)_4Al_3Si_6O_{22}(OH)_2 + 4\ SiO_2 \qquad (2)$$

$$= Ca(Fe,Mg)Si_2O_6 + 3\ (Fe,Mg)SiO_3 + CaAl_2Si_2O_8 + (Na,K)AlSi_3O_8 + H_2O.$$

The SO_3 component in this fluid could have facilitated the formation of the extensive pyrite and pyrrhotite, seen in the SGF and CGF, from pre-existing magnetite via the following reactions:

$$6\ SO_{3,aq} + Fe_3O_4 = 3\ FeS_2 + 11O_2 \qquad (3a)$$

and

$$(3+X)\ SO_{3,aq} + Fe_3O_4 = (3+X)\ Fe_{(1-X)}S + 13/2\ O_2. \qquad (3b)$$

Similar generalized reactions could be written for Fe-Mg silicate minerals present in the original amphibolite-facies rock where the Fe-Mg silicate mineral becomes more Mg-rich as Fe is taken up by the pyrite or pyrrhotite and O_2 is released as a part of this process:

$$6X\ SO_{3,aq} + Fe^{\text{Fe-Mg silicate}} = 3X\ FeS_2 + (1-3X)\ Fe^{\text{Fe-Mg silicate}} + 9\ XO_2 \qquad (4a)$$

and

$$(3+X)\ SO_{3,aq} + Fe^{\text{Fe-Mg silicates}} = (3+X)\ Fe_{(1-X)}S + (1-3X)\ Fe^{\text{Fe-Mg silicate}} + 9X/2\ O_2 \qquad (4b)$$

(Harlov *et al.*, 1997; Harlov & Hansen, 2005).

The O_2 produced by reactions (3) and (4) could have then have served to oxidize the ilmenite to hemo-ilmenite by removing Fe from the Fe-Mg silicate minerals or:

$$FeTiO_3 + O_2 + (X_{Fe})^{\text{Fe-Mg silicate}}$$

$$= (XFe_2O_3 + (1-X)FeTiO_3)^{\text{hemo-ilmenite}} + X_{Ti}\ (\text{in fluid}) + (1-X_{Fe})^{\text{Fe-Mg silicate}} \qquad (5)$$

The excess Ti would have primarily gone into the remaining biotite and amphibole helping to stabilize both minerals against conversion to orthopyroxene and clinopyroxene via Reactions (1) and (2) (cf. Henry *et al.*, 2005; Harlov *et al.*, 2006; Hansen & Harlov, 2007). Increasing oxidation would then be characterized by a decreasing Fe (= $Fe_{total}/(Fe_{total} + Mg)$) content in the Fe-Mg silicates, which is exactly what occurs along the Shevaroy Block traverse as the Fe content in the Fe-Mg minerals shows a distinct decrease with increasing oxygen fugacity and metamorphic grade going from the NAF to the CGF (cf. Harlov *et al.*, 1997, their fig. 9; Hansen & Harlov, 2007, their figs. 6 & 7).

The high oxidation state (near the magnetite-hematite buffer) of the granulite-facies rocks from the SGF and CGF would imply that the oxidation state of U would be as U^{6+}. This would explain the subsequent strong depletion in U both with respect to the whole-rock chemistry (Fig. 3f) and the metamorphic zircon grain rims (Figs. 7, 8, & 9). In such a scenario, U would have been strongly partitioned from the zircon grain rim into the sulphate-bearing, hypersaline grain boundary fluids as UO_2Cl_2 (Bali *et al.*, 2011) and subsequently removed from the system as the fluid migrated upwards to lower P-T. The relative immobility of Th^{4+} in the same oxidized fluids (Bali *et al.*, 2011) could have been alleviated by complexing with the SO_3 component in fluid as $Th(SO_4)_2$, which has experimentally been demonstrated to be highly mobile in sulphate-bearing aqueous fluids at least at lower temperatures and pressures (Nisbet *et al.*, 2019). However, the actual partitioning behaviour of either actinide between zircon and saline and/or sulphate-bearing fluids under high-grade oxidizing conditions is so far unknown, though Harlov *et al.* (2011) has demonstrated that Th^{4+} is relatively mobile under high P-T conditions (1000 MPa; 900 °C), at least on the mm scale, in monazite metasomatism experiments involving alkali-bearing, high pH fluids incorporating $Na_2Si_2O_5$, NaOH, or KOH.

The relative lack of U and Th depletion in the amphibolite-facies rocks of the NAF, compared with the granulite-grade SGF and CGF (Table 2; Figs. 4e,f), coupled with the low oxidation state, paucity of pyrite or pyrrhotite, and zircon metamorphic grain rims enriched in U relative to the cores (Figs. 6 & 9; Table 3; Electronic Supplementary Appendix 4), support the idea that under such relatively reducing conditions, S would have taken the form of H_2S (Harlov & Hansen, 2005). Uranium and Th would presumably have come out of solution as U^{4+} and Th^{4+}, and could have been partitioned in their relative trace amounts into the metamorphic zircon grain rims, the allanite, or newly formed titanite reaction rims around ilmenite.

Lastly, the haplogranite-saline fluid melting experiments of Aranovich *et al.* (2013, 2014, 2016) and Aranovich (2017) have demonstrated that at granulite-faces P-T, the presence of hypersaline fluids (H_2O activity approximately equal the $X_{H2O}{}^2$) will increase the melting temperature of granitoid rocks by around 100 °C (cf. Fig. 5), at mid-crustal pressures of and above 400 to 500 MPa. Upon ascending to lower pressures below 500 MPa, these same hypersaline fluids, perhaps now enriched in H_2O due to breakdown of biotite and amphiboles to pyroxenes at higher pressures, will revert to the H_2O activity being approximately equal to X_{H2O}, and inevitably cause this same granitoid rock to melt if the temperature is above the normal granite melting temperature for that X_{H2O} (cf. Newton *et al.*, 2019). Though not yet dated, but assuming that they have same Neoarchean age as the metamorphism, this could explain the presence of the numerous granitoid lenses and plutons seen straddling the orthopyroxene-in isograd in the clinopyroxene-rich region going from granulite to amphibolite grade along the Shevaroy Block traverse (Fig. 2) as well the bands, veins, and patches of pink granite seen in the northern CGF and southern NAF. If correct, the presence of these granitoid plutons and other melt features could be seen as another piece of evidence for the existence of these hypersaline fluids as they traveled through the mid-crust.

The role of zircon geochemistry and geochronology in helping to further elucidate and support speculations regarding the origins and chemical evolution of this traverse of lower late Archean crust, as outlined in previous studies (oxide, sulfide, phosphate, and silicate minerals), cannot be underestimated (Hansen *et al.*, 1995; Harlov *et al.*, 1997; Harlov, 2000; Hansen *et al.*, 2002; Harlov & Hansen, 2005; Hansen & Harlov, 2007). Through comparing the original magmatic zircon to that grown during a 40 My period of metamorphism, the depletion of elements such as U and Th in the metamorphic zircon reflects similar changes in bulk rock chemistry. Zircon provides significant information concerning the geochemistry of the original granitoid protolith as well as the changing geochemistry of the protolith during granulite-grade and amphibolite-grade metamorphism. Zircon is the only mineral that preserves the chemical information before, during, and after the metamorphic event, and as such represents a robust recorder that can be used to help both time the genesis of the lower crust as well as elucidate the subsequent metamorphic and metasomatic geochemical and physical processes that transformed it.

ACKNOWLEDGEMENTS

Special thanks to Prof. Kazuyuki Shiraishi for making available the analytical facilities of the National Institute of Polar Research available. Daniel Harlov was supported by an Invitational Fellowship for Research in Japan from the Japan Society for the Promotion of Science (or JSPS Invitational Fellowships for Research in Japan). Leonid Aranovich is thanked for performing the biotite-quartz-orthopyroxene-K-feldspar H_2O activity calculations. We thank Jamie Connolly for helping to confirm the results from the pseudo-section modelling using Perplex. This research was also supported by 2017R1A6A1A07015374 (Multidisciplinary study for assessment of large earth-quake potentials in the Korean Peninsula) through the National Research Foundation of Korea (NRF) funded by the Ministry of Science and ICT, Korea to Vinod Samuel.

The data underlying this article are available in the article and in its online supplementary material.

REFERENCES

Alletti, M., Baker, D.R., Scaillet, B., Aiuppa, A., Moretti, R. & Ottolini, L. (2009). Chlorine partitioning between a basaltic melt and H_2O-CO_2 fluids at Mount Etna. *Chemical Geology* **263**, 37–50.

Andersen, D.J. & Lindsley, D. (1988). Internally consistent solution models for Fe-Mg-Mn-Ti oxides: Fe-Ti oxides. *American Mineralogist* **73**, 714–726.

Andersen, D.J., Lindsley, D.H. & Davidson, P.M. (1993). QUIlF: A Pascal program to assess equilibria among Fe-Mg-Mn-Ti oxides, pyroxenes, olivine, and quartz. *Computers and Geosciences* **19**, 1333–1350.

Antignano, A. & Manning, C.E. (2008). Fluorapatite solubility in H_2O and H_2O–NaCl at 700 to 900 °C and 0.7 to 2.0 GPa. *Chemical Geology* **251**, 112–119.

Aranovich, L.Ya. (2017). The role of brines in high-temperature metamorphism and granitization. *Petrology* **25**, 486–497.

Aranovich, L.Ya. & Newton, R.C. (1996). H_2O activity in concentrated NaCl solutions at high pressures and temperatures measured by the brucite-periclase equilibrium. *Contributions to Mineralogy and Petrology* **125**, 200–212.

Aranovich, L.Ya. & Newton, R.C. (1997). H_2O activity in concentrated KCl solutions at high pressures and temperatures measured by the brucite-periclase equilibrium. *Contributions to Mineralogy and Petrology* **127**, 261–271.

Aranovich, L.Ya. & Newton, R.C. (1998). Reversed determination of the reaction: phlogopite + quartz = enstatite + potassium feldspar + H_2O in the ranges 750–875 °C and 2–12 kbar at low H_2O activity with concentrated KCl solutions. *American Mineralogist* **83**, 193–204.

Aranovich, L.Y. & Newton, R.C. (1999). Experimental determination of CO_2-H_2O activity-composition relations at 600–1000 °C and 6–14 kbar by reversed decarbonation and dehydration reactions. *American Mineralogist* **84**, 1319–1332.

Aranovich, L.Ya., Zakirov, I. V., Sretenskaya, N. G. & Gerya, T. V. (2010). Ternary system H_2O–CO_2–NaCl at high P–T parameters: an empirical mixing model. *Geochemistry International* **48**, 446–455.

Aranovich, L.Ya., Newton, R.C. & Manning, C.E. (2013). Brine-assisted anatexis: Experimental melting in the system haplogranite–H_2O–NaCl–KCl at deep-crustal conditions. *Earth and Planetary Science Letters* **374**, 111–120.

Aranovich, L.Ya., Makhluf, A.R., Manning, C.E. & Newton, C.E. (2014). Dehydration melting and the relationship between granites and granulites. *Precambrian Research* **253**, 26–37.

Aranovich, L.Ya. Makhluf, A.R., Manning, C.E. & Newton, C.E. (2016). Fluids, Melting, Granulites and Granites: A Controversy – Reply to the Commentary of J.D. Clemens, I.S. Buick, and G. Stevens. *Precambrian Research* **278**, 400–404.

Aranovich, L.Ya., Bortnikov, N.S. & Borisov, A.A. (2020). Ocean zircon as a petrogenetic indicator. *Russian Geology and Geophysics* **61**, 559–570.

Arndt, N.T. (2013). Formation and evolution of the continental crust. *Geochemical Perspectives* **2**, **no. 3**, 405–533.

Audetat, A. & Keppler, H. (2005). Solubility of rutile in subduction zone fluids, as determined by experiments in the hydrothermal diamond anvil cell. *Earth and Planetary Science Letters* **232**, 393–402.

Bali, E., Audetat, A. & Keppler, H. (2011). The mobility of U and Th in subduction zone fluids: an indicator of oxygen fugacity and fluid salinity. *Contributions to Mineralogy and Petrology* **161**, 597–613.

Behera, B.M., Waele, B.D., Thirukumaran, V., Sundaralingam, K., Narayanan, S., Sivalingam, B. & Biswal., T.K. (2019). Kinematics, strain pattern and geochronology of the Salem-Attur shear zone: Tectonic implications for the multiple sheared Salem-Namakkal blocks of the Southern Granulite terrane, India. *Precambrian Research* **324**, 32–61.

Bergantz, G.W. (1989). Underplating and partial melting: implications for melt generation and extraction. *Science* **245**, 1093–1095.

Berman, R.G., Aranovich, L.Ya., Rancourt, D.G. & Mercier, P.H.J. (2007). Reversed phase equilibrium constraints on the stability of Mg-Fe-Al biotite. *American Mineralogist* **92**, 139–150.

Bhaskar Rao, Y.J., Janardhan, A.S., Vijaya Kumar, T., Narayana, B.L., Dayal, A.M., Taylor, P.N. & Chetty, T.R.K. (2003). Sm-Nd model ages and Rb-Sr isotopic systematics of charnockites and gneisses across the Cauvery Shear Zone, Southern India: Implications for the Archean-Neoproterozoic Terrane Boundary in the Southern Granulite Terrain. In: M. Ramakrishnan (ed), *Tectonics of Southern Granulite Terrain: Kuppam-Palani Geotransect*. *Memoir – Geological Society of India* **50**, 297

Bohlen, S.R. & Mezger, K. (1989). Origin of granulite terranes and the formation of the lowermost continental crust. *Science* **244**, 326–329.

Brandt, S., Raith, M.M., Schenk, V., Sengupta, P., Srikantappa, C. & Gerdes, A. (2014). Crustal evolution of the Southern Granulite Terrane, south India: New geochronological and geochemical data for felsicorthogneisses and granites. *Precambrian Research* **246**, 91–122.

Braun, I. & Kriegsman, L.M. (2003). Proterozoic crustal evolution of southernmost India and Sri

Lanka in Proterozoic East Gondwana: Supercontinent assembly and breakup. In: M. Yoshida, B.F. Windley, S. Dasgupta (eds), *Geological Society of London, Special Publications* **206**, 169–202.

Brenan, J.M. & Watson, E.B. (1988). Fluids in the lithosphere, 2. Experimental constraints on CO_2 transport in dunite and quartzite at elevated p-T conditions with implications for mantle and crustal decarbonation processes. *Earth and Planetary Science Letters* **91**, 141–158.

Chadwick, B., Vasudev, V.N. & Hegde, G.V. (2000). The Dharwar Craton, southern India, interpreted as the result of Late Archaean oblique convergence. *Precambrian Research* **99**, 91–111.

Chardon, D., Jayananda, M., Chetty, T.R.K. & Peucat, J.J. (2008). Precambrian continental strain and shear zone patterns: South Indian case. *Journal of Geophysical Research* **113**, B08402, DOI: 10.1029/2007JB005299.

Chardon, D., Jayananda, M. & Peucat, J-J. (2011). Lateral constrictional flow of hot orogenic crust: insights from the Neoarchean of south India, geological and geophysical implications for orogenic plateaux. *Geochemistry Geophysics Geosystems* **12**, Q02005. doi:10.1029/2010GC003398

Chetty, T.R.K., Mohanty, D.P. & Yellappa, T. (2012). Mapping of shear zones in the Western Ghats, south-western part of Dharwar craton. *Journal of the Geological Society of India* **79**, 151–154.

Clark, C., Collins, A.S., Timms, N.E., Kinny, P.D., Chetty, T.R.K. & Santosh, M. (2009). SHRIMP U–Pb age constraints on magmatism and high-grade metamorphism in the Salem Block, southern India. *Gondwana Research* **16**, 27–36.

Collins, A.S., Clark, C. & Plavsa, D. (2014). Peninsula India in Gondwana: the tectonothermal evolution of the Southern Granulite Terrane and its Gondwanan counterparts. *Gondwana Research* **25**, 190–203.

Condie, K.C., Allen, P. & Narayana, B.L. (1982). Geochemistry of the Archean low- to high-grade transition zone, southern India. *Contributions to Mineralogy and Petrology* **81**, 157–167.

Connolly, J.A.D. (2005). Computation of phase equilibria by linear programming: a tool for geodynamic modelling and its application to subduction zone decarbonation. *Earth and Planetary Science Letters* **236**, 524–541.

Connolly, J.A.D. & Podladchokov, Y.Y. (2012). A hydromechanical model for lower crustal fluid flow. In: Harlov, D. & Austrheim, H. (eds) *Metasomatism and the Chemical Transformation of Rock: The Role of Fluids in Terrestrial and Extraterrestrial Processes*, Springer, Heidelberg, 599–658.

Corfu, F., Hanchar, J.M., Hoskin, P.W.O. & Kinny, P. (2003). Atlas of zircon textures. In: Hanchar, J.M. & Hoskin, P.W.O. (eds) *Zircon: Reviews in Mineralogy and Geochemistry*, vol. **53**, Washington DC: Mineralogical Society of America, pp. 469–500.

Davis, D.W., Williams, I.S. & Krogh, T.E. (2003). Historical development of zircon geochronology. In: Hanchar, J.M. & Hoskin, P.W.O. (eds) *Zircon: Reviews in Mineralogy and Geochemistry*, **53**, Washington DC: Mineralogical Society of America, pp. 145–182.

de Moor, J.M., Fisher, T.P., Sharp, Z.D., King, P.L., Wilke, M., Botcharnikov, R.E., Cottrel, E., Zelenski, M., Marty, B., Klimm, K., Rivard, C., Ayalew, D., Ramirez, C. & Kelly, K.A. (2013). Sulfur degassing at Erta Ale (Ethiopia) and Masaya (Nicaragua) volcanoes: Implications for degassing processes and oxygen fugacities of basaltic systems. *Geochemistry, Geophysics, Geosystems* **14**, doi: 10.1002/ggge.20255.

Dey, S. (2013). Evolution of Archaean crust in the Dharwar Craton: the Nd isotope record. *Precambrian Research* **227**, 227–246.

Drury, S.A. & Holt, R.W. (1980). The tectonic framework of the South Indian Craton: a reconnaissance involving Landsat imagery. *Tectonophysics* **65**, T1–T15.

Drury, S.A., Harris, N.B.W., Holt, R.W., Reeves-Smith, G.J. & Wightman, R.T. (1984). Precambrian tectonics and crustal evolution in south India. *Journal of Geology* **92**, 3–20.

Dulski, P. (2001). Reference materials for geochemical studies: new analytical data by ICP-MS and critical discussion of reference values. *Geostandards Newsletter* **25**, 87–125.

Fermor, L.L. (1936). An attempt at the correlation of the ancient schistose formations of Peninsular India. *Geological Survey of India Memoirs* **70**, 1–52.

Filiberto, J., Dasgupta, R., Gross, J. & Treiman, A.H. (2014). Effect of chlorine on near-liquidus phase equilibria of an Fe-Mg-rich tholeiitic basalt. *Contributions to Mineralogy and Petrology* **168**, 1027.

Friend, C.R.L. & Nutman, A.P. (1991). SHRIMP U-Pb geochronology of the Closepet granite and Peninsular gneisses, Karnataka, south India. *Journal of the Geological Society of India* **38**, 357–368.

Furlong, K.P. & Fountain, D.M. (1986). Continental crustal underplating: thermal considerations and seismic-petrologic consequences. *Journal of Geophysical Research* **91B**, 8285–8294.

Geisler, T., Schaltegger, U. & Tomaschek, F. (2007). Re-equilibration of zircon in aqueous fluids and melts. *Elements* **3**, 43–50.

Geological Survey of India (1993). Geological map of India, 1: 500000, Hyderabad.

Geological Survey of India (2001). District Resource map -Dharmapuri district, Tamil Nadu, 1:250000, Hyderabad.

Geological Survey of India (2005). District Resource map-Salem district, Tamil Nadu, 1:250000, Hyderabad.

George, P.M. & Sajeev K. (2015). Crustal evolution of the Kolli-Massif, southern India. *Journal of the Indian Institute of Science* **95**, 187–201.

Ghosh, J.G., de Wit, M.J. & Zartman, R.E. (2004). Age and tectonic evolution of Neoproterozoic ductile shear zones in the Southern Granulite terrane of India, with implications for Gondwana studies. *Tectonics* **23**, TC3006, DOI: 1029/2002TC001444.

Gibert, F., Guillaume, D. & Laporte, D. (1998). Importance of fluid immiscibility in the H_2O-NaCl-CO_2 system and selective CO_2 entrapment in granulites: experimental phase diagram at 5–7 kbar, 900 °C and wetting textures. *European Journal of Mineralogy* **10**, 1109–1123.

Gireesh, R.V., Sekhamo, K. & Jayananda, M. (2012). Anatomy of 2.57–2.52 Ga granitoid plutons in the eastern Dharwar Craton, southern India: Implications for magma chamber processes and crustal evolution. *Episodes* **35**, 398–413.

Glorie, S., de Grave, J., Singh, T., Payne, J. L. & Collins, A.S. (2014). Crustal root of the Eastern Dharwar Craton: Zircon U–Pb age and Lu–Hf isotopic evolution of the East Salem Block, southeast India. *Precambrian Research* **249**, 229–246.

Gou, L.-L., Zhai, M.-G., Zhang, C.-L., George, P.M., Lu, J.-S., Zhao, Y., Ao, W.-H., Hu, Y.-H., Zi, J.-W. & Zhou, F. (2022). Ultra-high temperature metamorphism and isobaric cooling of Neoarchean ultramafic-mafic granulites in the southern granulite terrain, India: Phase equilibrium modelling and SHRIMP zircon U–Pb dating. *Journal of Metamorphic Geology* **40**, https://doi.org/10.1111/jmg.12654.

Green, E.C.R., White, R.W., Diener, J.F.A., Powell, R., Holland, T.J.B. & Palin, R.M. (2016). Activity-composition relations for the calculation of partial melting equilibria for metabasic rocks. *Journal of Metamorphic Geology* **34**, 845–869.

Griffin, W.L. (1969). Replacement antiperthite in gneisses of the Babbit-Embarrass area, Minnesota, USA. *Lithos* **2**, 171–186.

Grotzinger, J.P. & Kasting, J.F. (1993). New constraints on Precambrian ocean composition. *Journal of Geology* **101**, 235–243.

Guergouz, C., Martin, L., Vanderhaeghe, O., Thebaud, N. & Fiorentini, M. (2018). Zircon and monazite petrochronologic record of prolonged amphibolite to granulite facies metamorphism in the Ivrea-Verbano and Strona-Ceneri Zones, NW Italy. *Lithos* **308-309**, 1–18.

Hansen, E.C., Newton, R.C., Janardhan, A.S. & Lindenberg, S. (1995). Differentiation of late Archean crust in the eastern Dharwar Craton, Krishnagiri-Salem area, south India. *Journal of Geology* **103**, 629–651.

Hansen, E.C., Khurram, A. & Harlov, D.E. (2002). Rb depletion in biotites and whole-rocks across an amphibolite to granulite-facies transition zone, Tamil Nadu, south India. *Lithos* **64**, 29–

47.

Hansen, E.C. & Harlov, D.E. (2007). Whole-rock, phosphate, and silicate compositional trends across an amphibolite- to granulite-facies transition, Tamil Nadu, India. *Journal of Petrology* **48**, 1641–1680.

Hansen, E., Johansson, L., Andersson, J., La Barge, L., Harlov, D., Möller, C. & Vincent, S. (2015). Partial melting in amphibolites in a deep section of the Sveconorwegian Orogen, SW Sweden. *Lithos* **236-237**, 27–45.

Hansteen, T.H. & Gurenko, A.A. (1998). Sulfur, chlorine, and fluorine in glass inclusions in olivine and clinopyroxene from basaltic hyaloclastites representing the Gran Canaria shield stage at Sites 953 and 956. *Proceeding of the Ocean Drilling Program, Scientific Results* **157**, 403–410.

Hao, L.-L., Wang, Q., Wyman, D.A., Ou, Q., Dan, W., Jiang, Z.-Q., Wi, F.-Y., Yang, J.-H., Long, X.-P. & Li, J. (2016). Underplating of basaltic magmas and crustal growth in a continental arc: Tibet. *Lithos* **245**, 223–242.

Harlov, D.E. (2000). Apparent pyrrhotite-chalcopyrite solid solutions in charnockites: the Shevaroy Hills Massif, Tamil Nadu, S. India and the Bamble Sector, SE Norway. *Mineralogical Magazine* **64**, 853–865.

Harlov, D.E. (2011). Petrological and experimental application of REE- and actinide-bearing accessory minerals to the study of Precambrian high-grade gneiss terranes. *The Geological Society of America Memoir* **207**, 13–24.

Harlov, D.E. (2015). Fluids and geochronometers: charting and dating mass transfer during metasomatism and metamorphism. *Journal of the Indian Institute of Science* **95**, 109–123.

Harlov, D.E., Newton, R.C., Hansen, E.C. & Janardhan, A.S. (1997). Oxide and sulphide minerals in highly oxidized, Rb-depleted, Archaean granulites of the Shevaroy Hills Massif, South India: Oxidation states and the role of metamorphic fluids. *Journal of Metamorphic Geology* **15**, 701–717.

Harlov, D.E., Hansen, E.C. & Bigler, C. (1998). Petrologic evidence for K-feldspar metasomatism in granulite facies rocks. *Chemical Geology* **151**, 373–386.

Harlov, D.E. & Förster, H.-J. (2002a). High-grade fluid metasomatism on both a local and a regional scale: the Seward Peninsula, Alaska and the Val Strona di Omegna, Ivrea-Verbano Zone, northern Italy. part I: petrography and silicate mineral chemistry. *Journal of Petrology* **43**, 769–799.

Harlov, D.E. & Förster, H.-J. (2002b). High-grade fluid metasomatism on both a local and a regional scale: the Seward Peninsula, Alaska and the Val Strona di Omegna, Ivrea-Verbano Zone, northern Italy. Part II: phosphate mineral chemistry. *Journal of Petrology* **43**, 801–

824.

Harlov, D.E., Förster, H.-J. & Nijland, T.G. (2002). Fluid-induced nucleation of REE-phosphate minerals in apatite: nature and experiment. Part I. chlorapatite. *American Mineralogist* **87**, 245–261.

Harlov, D.E. & Förster, H-J. (2003). Fluid-induced nucleation of (Y+REE)-phosphate minerals within apatite: nature and experiment. Part II. fluorapatite. *American Mineralogist* **88**, 1209–1229.

Harlov, D.E. & Hansen, E.C. (2005). Oxide and sulphide isograds along a late Archean, deep-crustal profile in Tamil Nadu, south India. *Journal of Metamorphic Geology* **23**, 241–259.

Harlov, D.E., Wirth, R. & Forster, H. (2005). An experimental study of dissolution–reprecipitation in fluorapatite: fluid infiltration and the formation of monazite. *Contributions to Mineralogy Petrology* **150**, 268–286.

Harlov, D.E., Johansson, L., van den Kerkhof, A. & Förster, H.-J. (2006). The role of advective fluid flow and diffusion during localized, solid-state dehydration: Söndrum stenhuggeriet, Halmstad, SW Sweden. *Journal of Petrology* **47**, 3–33.

Harlov, D.E. & Dunkley, D. (2010). Experimental high-grade alteration of zircon using alkali- and Ca-bearing solutions: resetting the zircon geochronometer during metasomatism. Abstract V41D-2301 presented at 2010 Fall Meeting, AGU, San Francisco, Calif., 13-17 Dec.

Harlov, D.E., Wirth, R. & Hetherington, C.J. (2011). Fluid-mediated partial alteration in monazite: the role of coupled dissolution–reprecipitation in element redistribution and mass transfer. *Contributions to Mineralogy and Petrology* **162**, 329–348.

Harlov, D. & Aranovich, L. (2018). The role of halogens in terrestrial and extraterrestrial geochemical processes: surface, crust, and mantle. In: Harlov, D. & Aranovich, L. (eds) *The Role of Halogens in Terrestrial and Extraterrestrial Geochemical Processes: Surface, Crust, and Mantle*, Springer, Heidelberg, pp. 1–20.

Hazarika, P., Pruseth, K.L. & Mishra, B. (2015). Neoarchean greenstone metamorphism in the Eastern Dharwar Craton, India: constraints from monazite U-Th-Pb_{total} ages and PT pseudosection calculations. *The Journal of Geology* **123**, 429–461.

Heinrich, W. (2007). Fluid immiscibility in metamorphic rocks. In: Liebscher, A., & Heinrich, C. (eds), *Fluid-Fluid Interactions Reviews in Mineralogy and Geochemistry* **65**, pp. 389–430.

Henry, D.J., Guidotti, C.V. & Thomson, J.A. (2005). The Ti-saturation surface for low-to-medium pressure metapelitic biotites: implications for geothermometry and Ti-substitution mechanisms. *American Mineralogist* **90**, 316–328.

Hokada, T., Horie, K., Satish–Kumar, M., Ueno, Y., Nasheeth, A., Mishima, K. & Shiraishi, K.

(2013). An appraisal of Archaean supracrustal sequences in Chitradurga Schist Belt, Western Dharwar Craton, Southern India. *Precambrian Research* **227**, 99–119.

Holland, T.J.B. & Powell, R.A. (1991). Compensated-Redlich-Kwong (CORK) equation for volumes and fugacities of CO_2 and H_2O in the range 1 bar to 50 kbar and 100–1600 °C. *Contributions to Mineralogy and Petrology* **109**, 265–273.

Holland, T.J.B. & Powell, R. (1998). An internally-consistent thermodynamic dataset for phases of petrological interest. *Journal of Metamorphic Geology* **16**, 309–344.

Holland, T.J.B. & Powell, R. (2003). Activity–composition relations for phases in petrological calculations: an asymmetric multicomponent formulation. *Contributions to Mineralogy and Petrology* **145**, 492–501.

Holland, T.J.B. & Powell, R. (2011). An improved and extended internally consistent thermodynamic dataset for phases of petrological interest, involving a new equation of state for solids. *Journal of Metamorphic Geology* **29**, 333–383.

Holness, M.B. & Graham, C.M. (1991). Equilibrium dihedral angles in the system H_2O-CO_2-NaCl-calcite, and implications for fluid flow during metamorphism. *Contributions to Mineralogy and Petrology* **108**, 368–383.

Holness, M.B. (1992). Equilibrium dihedral angles in the system quartz-CO_2-H_2O-NaCl at 800 °C and 1-15 kbar: the effects of pressure and fluid composition on the permeability of quartzites. *Earth and Planetary Science Letters* **114**, 171–184.

Holness, M.B. (1997). Surface chemical controls on pore-fluid connectivity in texturally equilibrated materials. In: Jamtveit, B. & Yardley, B.W.D. (eds) Fluid Flow and Transport in Rocks. London: Chapman & Hall, pp. 149–169.

Hoskin, P.W.O. & Schaltegger, U. (2003). The composition of zircon and igneous and metamorphic petrogenesis. In: Hanchar, J.M. & Hoskin, P.W.O. (eds) *Zircon: Reviews in Mineralogy & Geochemistry* **53**, Washington DC: Mineralogical Society of America, 27–62.

Ireland, T.R. & Williams, I.S. (2003). Considerations in zircon geochronology by SIMS. In: Hanchar, J.M., & Hoskin, P.W.O. (eds) *Zircon: Reviews in Mineralogy & Geochemistry* **53**, Washington DC: Mineralogical Society of America, 215–242.

Ishwar-Kumar, C., Windley, B.F., Horie, K., Kato, T., Hokada, T., Itaya, T., Yagi, K., Gouzu, C. & Sajeev, K. (2013). A Rodinian suture in western India: New insights on India-Madagascar correlations. *Precambrian Research* **236**, 227–251.

Ishwar-Kumar, C., Santosh, M., Wilde, S.A., Tsunogae, T., Itaya, T., Windley, B.F. & Sajeev, K. (2016). Mesoproterozoic suturing of Archean crustal blocks in western peninsular India: Implications for India-Madagascar correlations. *Lithos* **263**, 143–160.

Jayananda, M., Moyen, J.F., Martin, H., Peucat, J.J., Auvray, B. & Mahabaleswar, B. (2000). Late

Archean (2550-2520 Ma) juvenile magmatism in the Eastern Dharwar Craton, southern India: Constraints from geochronology, Nd-Sr isotopes and whole-rock geochemistry. *Precambrian Research* **99**, 225–254.

Jayananda, M., Chardon, D., Peucat, J.J. & Capdevila, R. (2006). 2.61 Ga potassic granites and crustal reworking in the Western Dharwar Craton, Southern India: Tectonic, geochronologic and geochemical constraints. *Precambrian Research* **150**, 1–26.

Jayananda, M., Banerjee, M., Pant, N.C., Dasgupta, S., Kano, T., Mahesha, N. & Mahabaleswar, B. (2012). 2.62 Ga high-temperature metamorphism in the central part of the Eastern Dharwar Craton: Implications for late Archaean tectonothermal history. *Geological Journal* **47**, 213–236.

Jayananda, M., Peucat, J.J., Chardon, D., Krishna Rao, B., Fanning, C.M. & Corfu, F. (2013). Neoarchean greenstone volcanism and continental growth, Dharwar Craton, southern India: constraints from SIMS U–Pb zircon geochronology and Nd isotopes. *Precambrian Research* DOI: http://dx.doi.org/10.1016/j.precamres.2012.05.002

Jayananda, M., Chardon, D., Peucat, J.-J., Tushipokla & Fanning, C.M. (2015). Paleo- to Mesoarchean TTG accretion and continental growth in the western Dharwar Craton, southern India: constraints from SHRIMP U–Pb zircon geochronology, whole-rock geochemistry and Nd–Sr isotopes. *Precambrian Research* **268**, 295–322.

Jayananda, M., Santosh, M. & Aadhiseshan, K. R. (2018). Formation of Archean (3600–2500 Ma) continental crust in the Dharwar Craton, southern India. *Earth Science Reviews* **181**, 12–42.

Jayananda, M., Aadhiseshan, K.R., Kusiak, M.A., Wilde, S.A., Sekhamo, K., Guitreu, M., Santosh, M. & Gireesh, R.V. (2020). Multi-stage crustal growth and Neoarchean geodynamics in the Eastern Dharwar Craton, southern India. *Gondwana Research* **78**, 228–260.

Johnson, E.L. (1991). Experimentally determined limits for H_2O-CO_2-NaCl immiscibility in granulites. *Geology* **19**, 925–928.

Jugo, P.J., Luth, R.W. & Richards, J.P. (2005). An experimental study of the sulfur content in basaltic melts saturated with immiscible sulfide or sulfate liquids at 1300 °C and 1.0 GPa. *Journal of Petrology* **46**, 783–798.

Kay, S.M., Jicha, B.R., Citron, G.L., Kay, R.W., Tibbetts, A.K. & Rivera, T.A. (2019). The calc-alkaline Hidden Bay and Kagalaska plutons and the construction of the central Aleutian oceanic arc crust. *Journal of Petrology* **60**, 1–47.

Konopasek, J., Pilatova, E., Kosler, J. & Slama, J. (2014). Zircon (re)crystallization during short-lived, high-P granulite facies metamorphism (Eger Complex, NW Bohemian Massif). *Journal of Metamorphic Geology* **32**, 885–902.

Kosler, J. & Sylvester, P.J. (2003). Present trends and the future of zircon geochronology: laser ablation ICPMS. In: Hanchar, J.M. & Hoskin, P.W.O. (eds) *Zircon: Reviews in Mineralogy & Geochemistry* **53**, Washington DC: Mineralogical Society of America, pp. 243–276.

Krogstad, E.J., Balakrishnan, S., Mukhopadhyay, D.K., Rajamani, V. & Hanson, G.N. (1989). Plate tectonics 2.5 Billion Years ago: evidence at Kolar, South India. *Science* **243**, 1337–1340.

Lancaster, P.J., Dey, S., Storey, C.D., Mitra, A. & Bhunia, R.K. (2014). Contrasting crustal evolution processes in the Dharwar Craton: Insights from detrital zircon U–Pb and Hf isotopes. *Gondwana Research* **28**, 1361–1372.

Lesne, P., Kohn, S.C., Blundy, J., Witham, F., Botcharnikov, R.E. & Behrens, H. (2011a). Experimental simulation of closed-system degassing in the system basalt-H_2O-CO_2-S-Cl. *Journal of Petrology* **52**, 1737–1762.

Lesne, P., Scaillet, B., Pichavant, M. & Beny, J.M. (2011b). The carbon dioxide solubility in alkali basalts: an experimental study. *Contributions to Mineralogy and Petrology* **162**, 153–168.

Li, S., Santosh, M., Ganguly, S., Thanooja, P.V., Sajeev, K., Pahari, A. & Manikyamba, C. (2018). Neoarchean microblock amalgamation in southern India: evidence from the Nallamalai Suture Zone. *Precambrian Research*, DOI: 10.1016/j.precamres.2018.05.017

Liu, X., Wang, W.R.Z., Zhao, Y., Liu, J., Chen, H., Cui, Y. & Song, B. (2016). Early Mesoproterozoic arc magmatism followed by early Neoproterozoic granulite facies metamorphism with a near-isobaric cooling path at Mount Brown, Princess Elizabeth Land, East Antarctica. *Precambrian Research* **284**, 30–48.

Lowenstern, J.B. (2000). A review of the contrasting behavior of two magmatic volatiles: chlorine and carbon dioxide. *Journal of Geochemical Exploration* **69**, 287–290.

Maibam, B., Gerdes, A. & Goswami, J.N. (2016). U–Pb and Hf isotope records in detrital and magmatic zircon from eastern and western Dharwar Craton, southern India: evidence for coeval Archaean crustal evolution. *Precambrian Research* **275**, 496–512.

Manikyamba, C., Ganguly, S., Santosh, M., Saha, A., Chatterjee, A. & Khelen, A.C. (2015). Neoarchean arc–juvenile back-arc magmatism in eastern Dharwar Craton, India: geochemical fingerprints from the basalts of Kadiri greenstone belt. *Precambrian Research* **258**, 1–23.

Manjari, K.G. Asha (1993). Fluid inclusion studies in charnockites from Yercaud area, Tamil Nadu. *Journal of Geological Society of India* **41**, 60–66.

Manning, C.E. (2004). The chemistry of subduction-zone fluids. *Earth and Planetary Science Letters* **223**, 1–16.

Manning, C.E. (2018). Fluids of the lower crust: deep is different. *Annual Review of Earth and Planetary Sciences* **46**, 67–97.

Manning, C.E. & Aranovich, L.Y. (2014). Brines at high pressure and temperature: thermodynamic, petrologic and geochemical effects. *Precambrian Research* **253**, 6–16.

Mathez, E.A. (1976). Sulfur solubility and magmatic sulfides in submarine basalt glass. *Journal of Geophysical Research* **81**, 4269–4276.

McDonough, W.F. & Sun S. (1995). The composition of the Earth. *Chemical Geology* **120**, 223–253.

Metrich, N., Berry, A.J., O'Neill, H.St.C. & Susini, J. (2009). The oxidation state of sulfur in synthetic and natural glasses determined by X-ray absorption spectroscopy. *Geochimica et Cosmochimica Acta* **73**, 2382–2399.

Metrich, N. & Mandeville, C.W. (2010). Sulfur in magmas. *Elements* **6**, 81–86.

Mi, J.-X. & Pan, Y. (2018). Halogen-rich minerals: crystal chemistry and geological significances. In: Harlov, D.E. & Aranovich, H. (eds) *The Role of Halogens in Terrestrial and Extraterrestrial Geochemical Processes*, Springer Geochemistry. Berlin Heidelberg: Springer-Verlag, pp. 123–184.

Mohan, M.R., Sarma, D.S., McNaughton, N.J., Fletcher, I.R., Wilde, S.A., Siddiqui, M.A., Rasmussen, B., Krapez, B., Gregory, C.J. & Kamo, S.L. (2014). SHRIMP zircon and titanite U-Pb ages, Lu-Hf isotope signatures and geochemical constraints for ~2.56 Ga granitic magmatism in Western Dharwar Craton, southern India: evidence for short-lived Neoarchean episodic crustal growth? *Precambrian Research* **243**, 197–220.

Morizet, Y., Paris, M., Gaillard, F. & Scaillet, B. (2010). C-O-H fluid solubility in haplobasalt under reducing conditions: an experimental study. *Chemical Geology* **279**, 1–16.

Newton, R.C. & Manning, C.E. (2000). Quartz solubility in H_2O-NaCl and H_2O-CO_2 solutions at deep crust-upper mantle pressures and temperatures: 2–15 kbar and 500–900 °C. *Geochimica et Cosmochimica Acta* **64**, 2993–3005.

Newton, R.C. & Manning, C. (2002). Experimental determination of calcite solubility in H_2O-NaCl solutions at deep crust/upper mantle pressures and temperatures: implications for metasomatic processes in shear zones. *American Mineralogist* **87**, 1401–1409.

Newton, R.C. & Manning, C. (2005). Solubility of anhydrite, $CaSO_4$, in NaCl-H_2O solutions at high pressures and temperatures: applications to fluid-rock interaction. *Journal of Petrology* **46**, 701–716.

Newton, R.C. & Manning, C.E. (2006). Solubilities of corundum, wollastonite and quartz in H_2O–NaCl solutions at 800 °C and 10 kbar: interaction of simple minerals with brines at high pressure and temperature. *Geochimica et Cosmochimica Acta* **70**, 5571–5582.

Newton, R.C. & Manning, C.E. (2007). Solubility of grossular, $Ca_3Al_2Si_3O_{12}$, in H_2O–NaCl solutions at 800 °C and 10 kbar, and the stability of garnet in the system $CaSiO_3$–Al_2O_3–H_2O–NaCl. *Geochimica et Cosmochimica Acta* **71**, 5191–5202.

Newton, R.C., Touret, J.L.R. & Aranovich, L.Y. (2014). Fluids and H_2O activity at the onset of granulite facies metamorphism. *Precambrian Research* **253**, 17–25.

Newton, R.C., Aranovich, L.Ya. & Touret, J.L.R. (2019) Streaming of saline fluids through Archean crust: another view of charnockite-granite relations in southern India. *Lithos* **346-347**, 105157.

Nisbet, H., Migdisov, A.A., Williams-Jones, A.E., Xu, H., van Hinsberg, V. & Roback, R. (2019). Challenging the thorium immobility paradigm. *Scientific Reports* **9**, 17035.

Novgorodov, P.G. (1977). On the solubility of quartz in H_2O + CO_2 and H_2O + NaCl at 700 °C and 1.5 kb pressure. *Geochemistry International* **12**, 191–193.

O'Connor, J.T. (1965). A classification for quartz-rich igneous rocks based on feldspar ratios. *U.S. Geological Survey, Professional Paper* **525-B**, 79–84.

O'Neill, H.St.C. & Mavrogenes, J.A. (2002). The sulfide capacity and the sulfur content at sulfide saturation of silicate melts at 1400 °C and 1 bar. *Journal of Petrology* **43**, 1049–1087.

O'Reilly, S., Griffin, W.L. & Stabel, A. (1988). Evolution of Phanerozoic eastern Australian lithosphere: isotopic evidence for magmatic and tectonic underplating. *Journal of Petrology*, Special Lithosphere Issue, 89–108.

Parsons, T., Sleep, N.H. & Thompson, G.A. (1992). Host rock rheology controls on the emplacement of tabular intrusions: implications for underplating of extending crust. *Tectonics* **11**, 1348–1356.

Peng, P., Qin, Z., Sun, F., Zhou, X., Guo, J., Zhai, M. & Ernst, R.E. (2019). Nature of charnockite and Closepet granite in the Dharwar Craton: implications for the architecture of the Archean crust. *Precambrian Research* **334**, 1-15.

Peressini, G., Quick, J.E., Sinigoi, S., Hofmann, A.W. & Fanning, M. (2007). Duration of a large mafic intrusion and heat transfer in the lower crust: a SHRIMP U-Pb zircon study in the Ivrea-Verbano Zone (Western Alps, Italy). *Journal of Petrology* **48**, 1185–1218.

Petford, N. & Gallagher, K. (2001). Partial melting of mafic (amphibolitic) lower crust by periodic influx of basaltic magma. *Earth and Planetary Science Letters* **193**, 483–499.

Peucat, J.J., Mahabaleswar, B. & Jayananda, M. (1993). Age of younger tonalitic magmatism and granulite metamorphism in the South Indian transition zone (Krishnigiri area); comparison with older Peninsular gneisses from the Gorur-Hassan area. *Journal of Metamorphic Geology* **11**, 879–888.

Peucat, J.J., Jayananda, M., Chardon, D., Capdevila, R., Fanning, C.M. & Paquette, J.L. (2013).

The lower crust of the Dharwar Craton, southern India: patchwork of Archean granulitic domains. *Precambrian Research* **227**, 4–28.

Plank, T. (2005). Constraints from thorium/lanthanum on sediment recycling at subduction zones and the evolution of the continents. *Journal of Petrology* **46**, 921–944.

Plank, T., Kelley, K.A., Zimmer, M.M., Hauri, E.H. & Wallace, P.J. (2013). Why do mafic arc magmas contain ~4 wt% water on average? *Earth and Planetary Science Letters* **364**, 168–179.

Plavsa, D., Collins, A.S., Foden, J.F., Kropinski, L., Santosh, M., Chetty, T.R.K. & Clark, C. (2012). Delineating crustal domains in Peninsular India: Age and chemistry of orthopyroxene-bearing felsic gneisses in the Madurai Block. *Precambrian Research* **198-199**, 77–93.

Plavsa, D., Collins, A.S., Payne, J.L., Foden, J.D., Clark, C. & Santosh, M. (2014). Detrital zircons in basement metasedimentary protoliths unveil the origins of southern India. *Geological Society of America Bulletin* **126**, 791–811.

Putnis, A. (2009). Mineral replacement reactions. *Thermodynamics and Kinetics of Water-Rock Interaction: Reviews in Mineralogy and Geochemistry*. **70**, 87–124.

Radhakrishna, B.P. & Naqvi, S.M. (1986). Precambrian continental crust of India and its evolution. *Journal of Geology* **94**, 145–166.

Raith, M., Srikantappa, C., Köhler, H. & Buhl, D. (1999). The Nilgiri enderbites: Nature and age constraints on protolith formation, high-grade metamorphism and cooling history. *Precambrian Research* **98**, 129–150.

Raith, M.M., Brandt, S., Sengupta, P., Berndt, J., John, T. & Srikantappa, C. (2016). Element mobility and behaviour of zircon during HT metasomatism of ferroan basic granulite at Ayyarmalai, south India: evidence for polyphase Neoarchaean crustal growth and multiple metamorphism in the northeastern Madurai Province. *Journal of Petrology* **57**, 1729–1774.

Ramakrishnan, M. (1988). Tectonic evolution of the Archaean high grade terrain of south India. *Journal of the Geological Society of India* **31**, 118-120.

Rameshwar Rao, D., Narayanana, B.L. & Balaram, V. (1991a). Nature and origin of lower crustal rocks of Dharmapuri area, Tamil Nadu, southern India – a geochemical approach. *Geochemical Journal* **25**, 57–74.

Rameshwar Rao, D., Charan, S.N. & Natarajan, R. (1991b). P-T conditions and geothermal gradient of gneiss-enderbite rocks: Dharmapuri area, Tamil Nadu, India. *Journal of Petrology* **32**, 539–554.

Ratheesh-Kumar, R.T., Santosh, M., Yang, Q., Ishwar-Kumar C., Chen, N. & Sajeev, K. (2016).

Archean tectonics and crustal evolution of the Biligiri Rangan Block, southern India. *Precambrian Research* **275**, 406–428.

Ratheesh-Kumar, R.T., Windley, B.F., Xiao, W.J., Jia, X-L., Mohanty, D.P., & Zeba-Nezrin, F.K. (2020). Early growth of the Indian lithosphere: implications from the assembly of the Dharwar Craton and adjacent granulite blocks, southern India. *Precambrian Research* **336**, 105491.

Rogers, J.J.W. & Giral, R.A. (1997). The Indian shield in greenstone belts. in de Wit, M. & Ashwal, L. (eds), *Oxford Monograph of Geology and Geophysics*, Oxford University Press, New York 35, 620–635.

Rudnick, R.L. & Jackson, I. (1995). Measured and calculated elastic wave speeds in partially equilibrated mafic granulite xenoliths: implications for the properties of an underplated lower continental crust. *Journal of Geophysical Research* **100**, 10211–10218.

Samuel, V.O., Santosh, M., Liu, S., Wang, W. & Sajeev, K. (2014). Neoarchean continental growth through arc magmatism in the Nilgiri Block, southern India. *Precambrian Research* **245**, 146-173.

Samuel, V.O., Harlov, D.E., Kwon, S. & Sajeev, K. (2019). Silicate, oxide, and sulphide trends in neo-Archean rocks from the Nilgiri Block, southern India: the role of fluids during high-grade metamorphism. *Journal of Petrology* **60**, 1027–1062.

Santosh, M. & Tsunogae, T. (2003). Extremely high density pure CO_2 fluid inclusions in a garnet granulite from southern India. *Journal of Geology* **111**, 1–16.

Santosh, M., Maruyama, S. & Sato, K. (2009). Anatomy of a Cambrian suture in Gondwana: Pacific-type orogeny in southern India? *Gondwana Research* **16**, 321–341.

Santosh, M., Yang, Q.Y., Shaji, E., Tsunogae, T., Ram Mohan, M. & Satyanarayanan, M. (2015). An exotic Mesoarchean microcontinent: the Coorg block, southern India. *Gondwana Research* **27**, 165–195.

Santosh, M., Hu, C.-N., He, X.-F., Li, S.S., Tsunogae, T., Shaji, E. & Indu, G. (2017). Neoproterozoic arc magmatism in the southern Madurai Block, India: Subduction, relamination, continental outbuilding, and the growth of Gondwana. *Gondwana Research* **45**, 1–42.

Satish-Kumar, M. (2005). Graphite-bearing CO_2–fluid inclusions in granulites: insights on graphite precipitation and carbon isotope evolution. *Geochimica et Cosmochimica Acta* **69**, 3841–3856.

Shmulovich, K., Graham, C. & Yardley, B. (2001). Quartz, albite, and diopside solubilities in H_2O-NaCl and H_2O-CO_2 fluids at 0.5 – 0.9 GPa. *Contributions to Mineralogy and Petrology* **141**, 95–108.

Spooner, C.M. & Fairbairn H.W. (1970). Strontium[87]/Strontium[86] initial ratios in pyroxene granulite terranes. *Journal of Geophysical Research* **75**, 6706–6713.

Sreehari, L. & Toyoshima, T. (2020). Structural architecture and geological relationships in the southern part of Chitradurga Schist Belt, Dharwar craton, south India. *Journal of Mineralogical and Petrological Sciences.* DOI: 10.2465/jmps.191120

Stipska, P., Powell, R., Hacker, B.R., Holder, R. & Kylander-Clark, A.R.C. (2016). Uncoupled U/Pb and REE response in zircon during the transformation of eclogite to mafic and intermediate granulite (Blansky les, Bohemian Massif). *Journal of Metamorphic Geology* **34**, 551–572.

Swami Nath, J. & Ramakrishnan, M. (1981). Present classification and correlation, in early Precambrian supracrustals of southern Karnataka. In: J. Swami Nath, M. Ramakrishnan (eds), *Memoirs of the Geological Survey of India* **112**, 23–38.

Tanis, E.A., Simon, A.C., Zhang, Y., Chow, P. & Xiao, Y. (2016). Rutile solubility in NaF-NaCl-KCl-bearing aqueous fluids at 0.5-2.79 GPa and 250-650 °C. *Geochimica et Cosmochimica Acta* **177**, 170–181.

Thanooja, P.V., Santosh, M., Li, S., Nandakumar, V., & Ishwar-Kumar, C. (2021a). Neoarchaean crustal evolution along the eastern flank of Nallamalai Shear Zone, southern India. *International Geology Review,* DOI: 10.1080/00206814.2021.2012717

Thanooja, P.V., Williams, I.S., Satish-Kumar, M., Durgalakshmi, Zhai, M.G., Oh, C.W., Windley, B.F. & Sajeev, K. (2021b). Were South India, the North China Craton, and the Korean Peninsula contiguous in a Neoarchaean supercontinent? New geochemical and isotopic constraints. *Lithos* **398-399**, 106294.

Thomas, R.W. & Wood, B.J. (2022). The effect of composition on chlorine solubility and behaviour in silicate melts. *American Mineralogist* **107** (in press)

Thybo, H. & Artemieva, I.M. (2013). Moho and magmatic underplating in continental lithosphere. *Tectonophysics* **609**, 605–619.

Touret, J.L.R. & Nijland, T.G. (2013). Prograde, peak and retrograde metamorphic fluids and associated metasomatism in upper amphibolite to granulite facies transition zones. In: Harlov, D.E. & Austrheim, H. (eds) *Metasomatism and the Chemical Transformation of Rock: The Role of Fluids in Terrestrial and Extraterrestrial Processes*, Springer-Nature, Berlin Heidelberg, 415–469.

Tropper, P., Manning, C.E. & Harlov, D.E. (2011). Solubility of $CePO_4$ monazite and YPO_4 xenotime in H_2O and H_2O–NaCl at 800 °C and 1 GPa: implications for REE and Y transport during high-grade metamorphism. *Chemical Geology* **282**, 58–66.

Tropper, P., Manning, C.E. & Harlov, D.E. (2013). Experimental determination of $CePO_4$ and

YPO_4 solubilities in H_2O–NaF at 800 °C and 1 GPa: implications for rare earth element transport in high-grade metamorphic fluids. *Geofluids* **13**, 372–380.

Tushipokla & Jayananda, M. (2013). Geochemical constraints on komatiite volcanism from Sargur Group Nagamangala greenstone belt, western Dharwar Craton, southern India: implications for Mesoarchean mantle evolution and continental growth. *Geoscience Frontiers* **4**, 321–340.

Unsworth, M. & Rondenay, S. (2012). Mapping the distribution of fluids in the crust and lithospheric mantle utilizing geophysical methods. In: Harlov, D. & Austrheim, H. (eds) *Metasomatism and the Chemical Transformation of Rock: The Role of Fluids in Terrestrial and Extraterrestrial Processes*, Springer-Nature, Berlin Heidelberg, 535–598.

Van den Kerkhof, A., Kronz, A. & Simon, K. (2014). Deciphering fluid inclusions in high-grade rocks. *Geoscience Frontiers* **5**, 683–695.

Wallace, P.J. (2005). Volatiles in subduction zone magmas: concentrations and fluxes based on melt inclusion and volcanic gas data. *Journal of Volcanology and Geothermal Research* **140**, 217–240.

Walters, J.B., Cruz-Uribe, A.M. & Marschall, H.R. (2019). Isotopic compositions of sulfides in exhumed high-pressure terranes: Implications for sulfur cycling in subduction zones. *Geochemistry, Geophysics, Geosystems* **20**, 3347–3374.

Watson, E.B. & Brenan, J.M. (1987). Fluids in the lithosphere. 1. Experimentally determined wetting characteristics of CO_2-H_2O fluids and their implications for fluid transport, host-rock physical properties, and fluid inclusion formation. *Earth and Planetary Science Letters* **85**, 594–615.

Webster, J.D., Kinzler, R.J. & Mathez, E.A. (1999). Chloride and water solubility in basalt and andesite melts and implications for magmatic degassing. *Geochimica et Cosmochimica Acta* **63**, 729–738.

Webster, J.D., Vetere, F., Botcharnikov, R.E., Goldoff, B., McBirney, A. & Doherty, A.L. (2015). Experimental and modeled chlorine solubilities in aluminosilicate melts at 1 to 7000 bars and 700 to 1250 °C: applications to magmas of Augustine volcano, Alaska. *American Mineralogist* **100**, 522–535.

White, R.W., Powell, R. & Clarke, G.L. (2002). The interpretation of reaction textures in Fe-rich metapelitic granulites of the Musgrave Block, central Australia: constraints from mineral equilibria calculations in the system K_2O-FeO-MgO-Al_2O_3-SiO_2-H_2O-TiO_2-Fe_2O_3. *Journal of Metamorphic Geology* **20**, 41–55.

White, R.W., Powell, R., Holland, T.J.B., Johnson, T.E. & Green, E.C.R. (2014). New mineral activity–composition relations for thermodynamic calculations in metapelitic systems. *Journal of Metamorphic Geology* **32**, 261–286.

Williams, M.L., Jercinovic, M.J., Harlov, D.E., Budzyn, B. & Hetherington, C.J. (2011). Resetting monazite ages during fluid-related alteration. *Chemical Geology* **283**, 218–225.

Witham, F., Blundy, J., Kohn, S.C., Lesne, P., Dixon, J., Churakov, S.V. & Botcharnikov, R. (2012). SolEx: A model for mixed COHSCl-volatile solubilities and exsolved gas compositions in basalt. *Computers & Geosciences* **45**, 87–97.

Yakymchuk, C. Kirkland, C.L. & Clark, C. (2018). Th/U ratios in metamorphic zircon. *Journal of Metamorphic Geology* **36**, 715–737.

Yang, Q.Y. & Santosh, M. (2015). Zircon U-Pb geochronology and Lu-Hf isotopes from the Kolar greenstone belt, Dharwar craton, India: implications for crustal evolution in an ocean-trench-continental transect. *Journal of Asian Earth Sciences* **113**, 797–811.

Zellmer, G.F., Edmonds, M. & Straub, S.M. (2015). Volatiles in subduction zone magmatism. In: Zellmer, G.F., Edmonds, M. & Straub, S.M. (eds) *The Role of Volatiles in the Genesis, Evolution and Eruption of Arc Magmas*. Geological Society, London, Special Publications **410**, 1–17.

FIGURE CAPTIONS

Figure 1: Regional geology and tectonic framework of southern India (after, Geological Survey of India, 1993; Drury & Holt, 1980; Ishwar-Kumar *et al.*, 2013). A box outlines the Shevaroy Block. The 'isotopic boundary ' is taken from Plavsa *et al.* (2012, 2014).

Acronyms: KSZ- Kumta shear zone, McSZ- Mercara shear zone, ChSZ- Chitradurga shear zone, MKSZ- Mettur-Kolar shear zone, NSZ- Nallamalai shear zone, MSZ- Moyar shear zone, SASZ- Salem-Attur shear zone, BSZ- Bhavani shear zone, CaSZ- Cauvery shear zone, PCSZ- Palghat-Cauvery shear zone, KKPT SZ- Karur-Kambam-Painavu-Trichur shear zone, SSZ – Suruli shear zone, ASZ- Achankovil shear zone.

Figure 2a: Zircon sample locations from the study area and structural lineaments overlain on the geological map (modified after Geological Survey of India, 1993, 2001, 2005; Ishwar-Kumar *et al.*, 2013). Structural lineaments were extracted from Landsat ETM$^+$ satellite imagery and ASTER digital elevation model. The blue triangles mark the locations of previously published U-Pb zircon ages. A = 2557 Ma igneous age; B = 2553 Ma igneous age; C = 2532 Ma igneous age; D = 2528 Ma; E = 2538 Ma igneous age, 2473 Ma metamorphic age; F = 2529 Ma igneous age, 2482 Ma metamorphic age; G = 2647 Ma igneous age, 2442 Ma metamorphic age; H = 2536 Ma igneous age, 2477 Ma metamorphic age; I = 2532 Ma igneous age, 2484 Ma metamorphic age; J = 2543 Ma igneous age, 2508 Ma metamorphic age; K = 2548 Ma igneous age, 2515 Ma metamorphic age; L = 2575 Ma igneous age, 2483 Ma metamorphic age; M = 2544 Ma igneous age, 2517 Ma metamorphic age; N = 803 Ma igneous age; O = 821 Ma igneous age; P = 2758, 2657 Ma igneous age; Q = 2530 Ma igneous age; R = 2545 Ma igneous age; S = 2714 Ma igneous age, 2536 metamorphic age; T = 2559 Ma igneous age, 2493 Ma metamorphic age; U = 2553 Ma igneous age, 2511 Ma metamorphic age; V = 2511 Ma igneous age, 2475 Ma metamorphic age; W = 2518 Ma igneous age, 2476 Ma metamorphic age. The magmatic and metamorphic ages, method, sample details and publications references are listed in Electronic Supplementary Appendix 1b. Acronyms: Pyx-Pyroxene; Mt-Magnetite; Fch-Fuchsite; Ep-Epidote; Hbl-Hornblende; Bt-Biotite.

Figure 2b: Simplified map with lithology legend same as in Figure **2a**, which defines the boundaries (dashed line) between the Southern Granulite Facies Zone (SGF), the Central Granulite Facies Zone (CGF), and the Northern Amphibolite Facies Zone (NAF). Zircon sample locations are marked.

Figure 3: Classification of the rock types listed in Table 1 from which the zircon separates used in this study were taken plotted on the feldspar ternary (cf. O'Connor, 1965; see also fig. 8 in Hansen *et al.*, 1995). Whole rock data is taken from Electronic Supplementary Appendix 7a.

Figure 4: Plot of whole-rock SiO_2 (**a**); Zr (**b**); Rb (**c**); REE (**d**); Th (**e**); and U (**f**) as a function of distance along a traverse going southwards from the northernmost sample, i.e. 95 J3 H5, (cf. Fig. 2). Trace element data is taken from Table 2. Whole rock data is taken from Electronic Supplementary Appendix 7a. Dotted lines designate the approximate boundaries between the higher-grade, southern granulite-facies zone (SGF), the lower-grade, central granulite-facies zone (CGF), and the northern amphibolite-facies zone (NAF).

Figure 5: Pseudo-section plots for sample 93 F9 F8 for $X_{NaCl} = 0.4$, $X_{CO2} = 0.1$ (**a**); $X_{CO2} = 0.8$ (**b**); $X_{NaCl} = 0.5$, $X_{CO2} = 0.1$ (**c**); and $X_{CO2} = 0.9$ (**d**). Temperature-pressure, pseudo-section plots (700–1000 °C; 200–1200 MPa) were created using the Holland & Powell (2011) mineral chemical database (hp11ver.dat) implemented in the PerpleX (version 6.7.9) software of Connolly (2005). See text for further explanation.

Figure 6: BSE and CL image examples of zircon separates (**a – f**) and *in situ* zircons (**g, h**) from the NAF, Shevaroy Block traverse (cf. Tables 1 & 3; Fig. 2). The sample number corresponding to the sample number in Table 3 is given after the letter designating the image (see also Table 1 and Fig. 2a). In the SHRIMP analytical spot label, the first line designates the spot number. The letter associated with the spot number designates igneous (I), xenocrystic (X), high U metamorphic rim (E), and low U metamorphic rim (D) (cf. Table 3). The second line designates the age, the third line the amount of U measured, and the fourth line the Th/U ratio (cf. Table 3).

Figure 7: BSE and CL image examples of zircon separates (**a – f**) and *in situ* zircons (**g, h**) from the CGF, Shevaroy Block traverse (cf. Tables 1 & 3; Fig. 2). The sample number corresponding to the sample number in Table 3 is given after the letter designating the image (see also Table 1 and Fig. 2a). In the SHRIMP analytical spot label, the first line designates the spot number. The letter associated with the spot number designates igneous (I), xenocrystic (X), sector zoned (S), and low U metamorphic rim (D) (cf. Table 3). The second line designates the age, the third line the amount of U measured, and the fourth line the Th/U ratio (cf. Table 3).

Figure 8: BSE and CL image examples of zircon separates (**a – f**) and *in situ* zircons (**g – i**) from the SGF with the exception of those from sample 20, which is from the southern edge of the CGF

(cf. Tables 1 & 3; Fig. 2). The sample number corresponding to the sample number in Table 3 is given after the letter designating the image (see also Table 1 and Fig. 2a). In the SHRIMP analytical spot label, the first line designates the spot number. The letter associated with the spot number designates igneous (I), sector zoned (S), and low U metamorphic rim (D) (cf. Table 3). The second line designates the age, the third line the amount of U measured, and the fourth line the Th/U ratio (cf. Table 3).

Figure 9: Concordia Tera-Wasserburg plots for zircons from the 29 samples along the Shevaroy Block traverse (see also Fig. 2a and Tables 1 & 3). Sample labels in Figure 2 and the Tables are designated after each of the simplified sample numbers. Label definition and colour code are given in the figure legend. Open ellipses refer to age data not used in the age estimate (see Electronic Supplementary Appendix 4). The dashed horizontal lines refer to the weighted mean age estimates for generations of zircon growth and for titanite growth, as summarized, in Table 5. Xenocrystic analyses (yellow symbols) plotted in the Th vs. U plot are not plotted on the concordia for samples 4, 9, and 11.

Figure 10: Plot of zircon ages with error bars as a function of location along a stylized depiction of the Shevaroy Block traverse (see Tables 1 & 5 and Fig. 2b). Label definition and colour code are given in the figure legend. Reference to U-enriched/U-undepleted/U-depleted zircon is relative to magmatic zircon in each sample, and not to the data set as a whole (cf. U vs. Th plots in Fig. 9). Sketches of zircon grains show the different responses of magmatic zircon (red) to metamorphism in the Northern Amphibolite Facies (NAF) zone (top), versus metamorphism in the Central Granulite Facies (CGF) and Southern Granulite Facies (SGF) zones (bottom).

Figure 11: Plot of whole-rock and zircon U and Th abundances and Th/U as a function of distance and metamorphic grade from granulite- (SGF and CGF) to amphibolite-facies (NAF) along with a depiction of the Shevaroy Block traverse (Fig. 2b), which indicates the corresponding sample location of each point in the three plots. Circles around the symbol for whole rock analyses indicate that the sample contains either discrete, independent monazite grains, or titanite rims around ilmenite and allanite grains.

Figure 12: Scatter plot of zircon trace element (ppm) U vs. Th (**a**) and U vs. Yb (**b**). For each zircon type lines enclose the full data set whereas shaded areas enclose 67% of the data set. Chondrite (C1) normalized (McDonough & Sun, 1995) zircon REE plots of detrital/xenocrystic, magmatic, and U-enriched metamorphic areas in the zircon (**c**), detrital/xenocrystic, magmatic, and

undepleted metamorphic areas in the zircon (**d**), and detrital/xenocrystic, magmatic, and U-depleted metamorphic areas in the zircon (**e**).

Figure 1

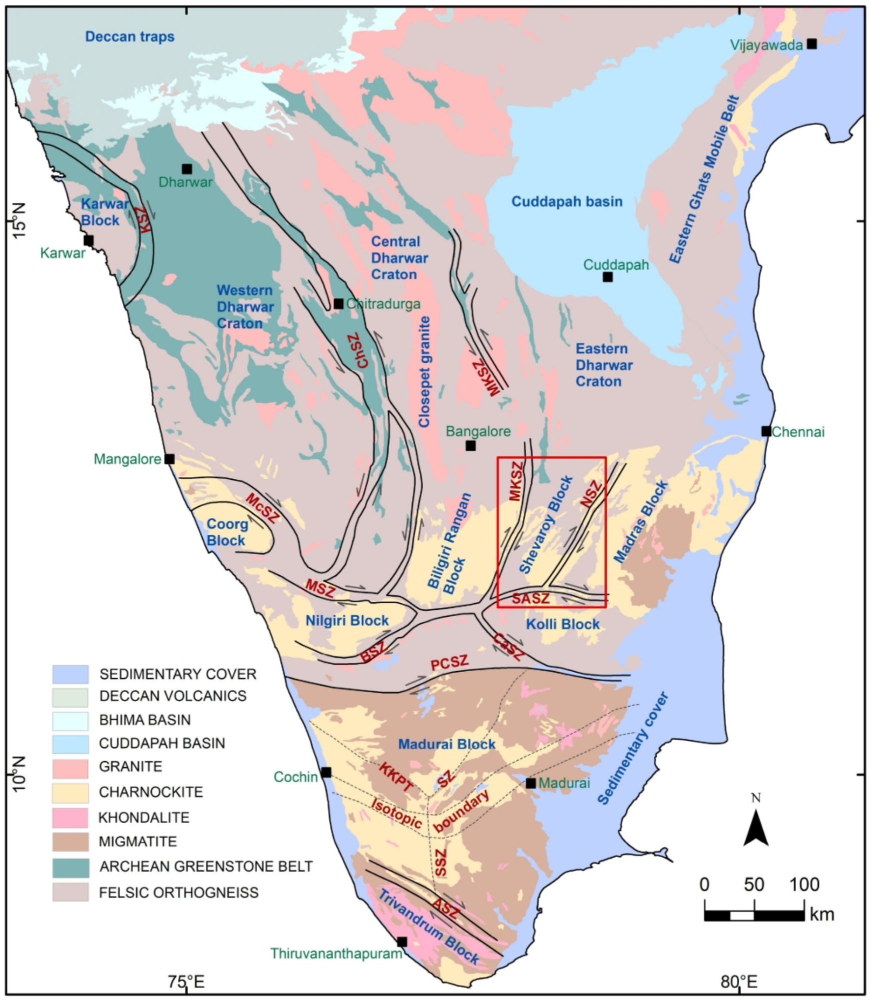

Figure 1: Regional geology and tectonic framework of southern India (after, Geological Survey of India, 1993; Drury & Holt, 1980; Ishwar-Kumar et al., 2013). A box outlines the Shevaroy Block. The ‘isotopic boundary ‘ is taken from Plavsa et al. (2012, 2014).
Acronyms: KSZ- Kumta shear zone, McSZ- Mercara shear zone, ChSZ- Chitradurga shear zone, MKSZ- Mettur-Kolar shear zone, NSZ- Nallamalai shear zone, MSZ- Moyar shear zone, SASZ- Salem-Attur shear zone, BSZ- Bhavani shear zone, CaSZ- Cauvery shear zone, PCSZ- Palghat-Cauvery shear zone, KKPT SZ- Karur-Kambam-Painavu-Trichur shear zone, SSZ – Suruli shear zone, ASZ- Achankovil shear zone.

179x236mm (300 x 300 DPI)

Figure 2

(a)

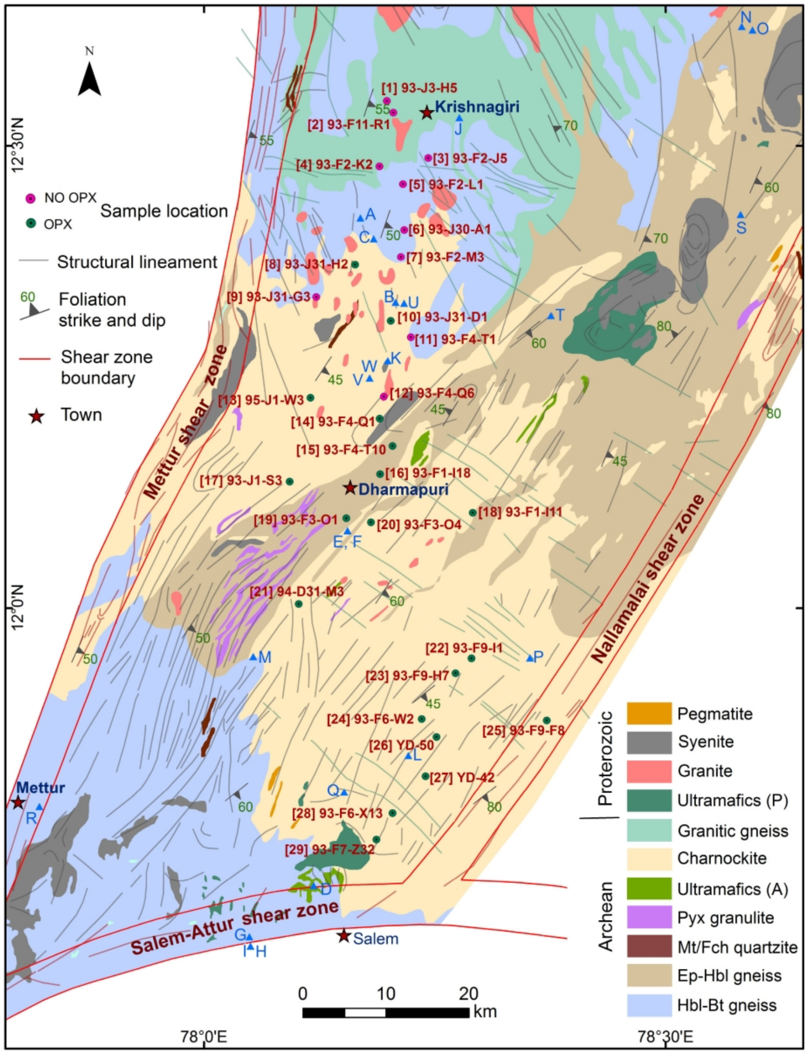

Figure 2a: Zircon sample locations from the study area and structural lineaments overlain on the geological map (modified after Geological Survey of India, 1993, 2001, 2005; Ishwar-Kumar et al., 2013). Structural lineaments were extracted from Landsat ETM+ satellite imagery and ASTER digital elevation model. The blue triangles mark the locations of previously published U-Pb zircon ages. A = 2557 Ma igneous age; B = 2553 Ma igneous age; C = 2532 Ma igneous age; D = 2528 Ma; E = 2538 Ma igneous age, 2473 Ma metamorphic age; F = 2529 Ma igneous age, 2482 Ma metamorphic age; G = 2647 Ma igneous age, 2442 Ma metamorphic age; H = 2536 Ma igneous age, 2477 Ma metamorphic age; I = 2532 Ma igneous age, 2484 Ma metamorphic age; J = 2543 Ma igneous age, 2508 Ma metamorphic age; K = 2548 Ma igneous age, 2515 Ma metamorphic age; L = 2575 Ma igneous age, 2483 Ma metamorphic age; M = 2544 Ma igneous age, 2517 Ma metamorphic age; N = 803 Ma igneous age; O = 821 Ma igneous age; P = 2758, 2657 Ma igneous age; Q = 2530 Ma igneous age; R = 2545 Ma igneous age; S = 2714 Ma igneous age, 2536 metamorphic age; T = 2559 Ma igneous age, 2493 Ma metamorphic age; U = 2553 Ma igneous age, 2511 Ma metamorphic age; V = 2511 Ma igneous age, 2475 Ma metamorphic age; W = 2518 Ma igneous age, 2476 Ma metamorphic age. The magmatic and metamorphic ages, method, sample details and publications

references are listed in Electronic Supplementary Appendix 1b. Acronyms: Pyx-Pyroxene; Mt-Magnetite; Fch-Fuchsite; Ep-Epidote; Hbl-Hornblende; Bt-Biotite.

195x251mm (300 x 300 DPI)

Figure 2

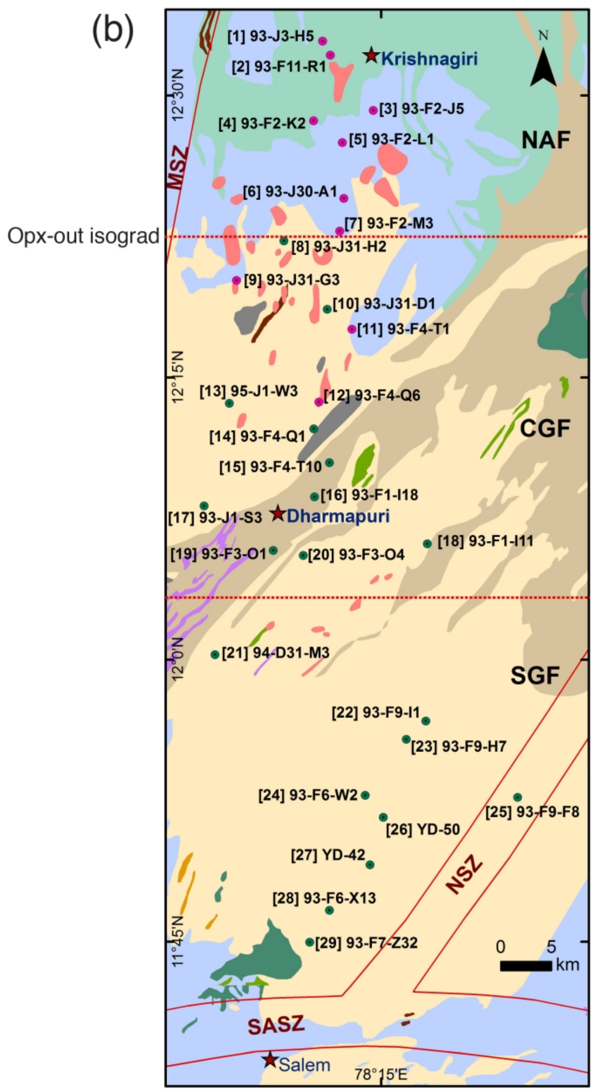

Figure 2b: Simplified map with lithology legend same as in Figure 2a, which defines the boundaries (dashed line) between the Southern Granulite Facies Zone (SGF), the Central Granulite Facies Zone (CGF), and the Northern Amphibolite Facies Zone (NAF). Zircon sample locations are marked.

159x274mm (300 x 300 DPI)

Figure 3

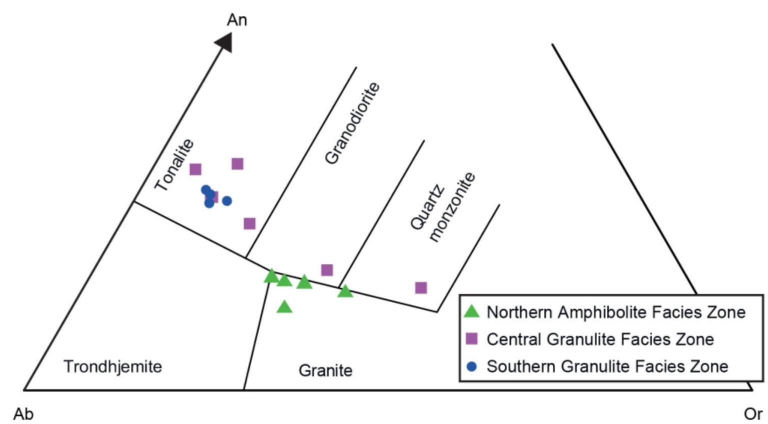

Figure 3: Classification of the rock types listed in Table 1 from which the zircon separates used in this study were taken plotted on the feldspar ternary (cf. O'Connor, 1965; see also fig. 8 in Hansen et al., 1995). Whole rock data is taken from Electronic Supplementary Appendix 7a.

165x119mm (300 x 300 DPI)

Figure 4

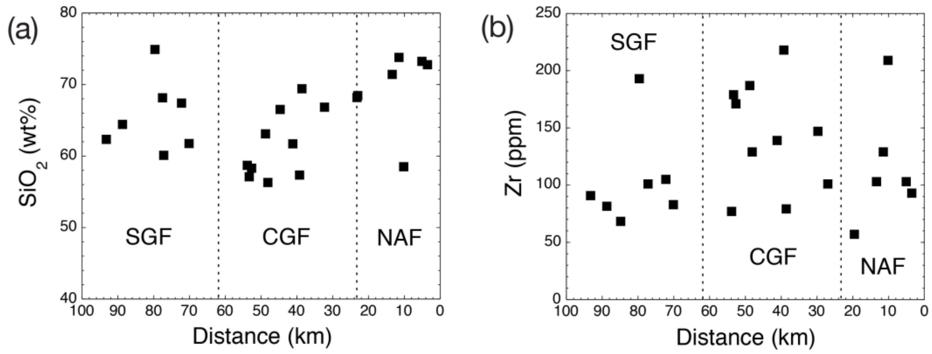

Figure 4: Plot of whole-rock SiO2 (a); Zr (b); Rb (c); REE (d); Th (e); and U (f) as a function of distance along a traverse going southwards from the northernmost sample, i.e. 95 J3 H5, (cf. Fig. 2). Trace element data is taken from Table 2. Whole rock data is taken from Electronic Supplementary Appendix 7a. Dotted lines designate the approximate boundaries between the higher-grade, southern granulite-facies zone (SGF), the lower-grade, central granulite-facies zone (CGF), and the northern amphibolite-facies zone (NAF).

279x115mm (300 x 300 DPI)

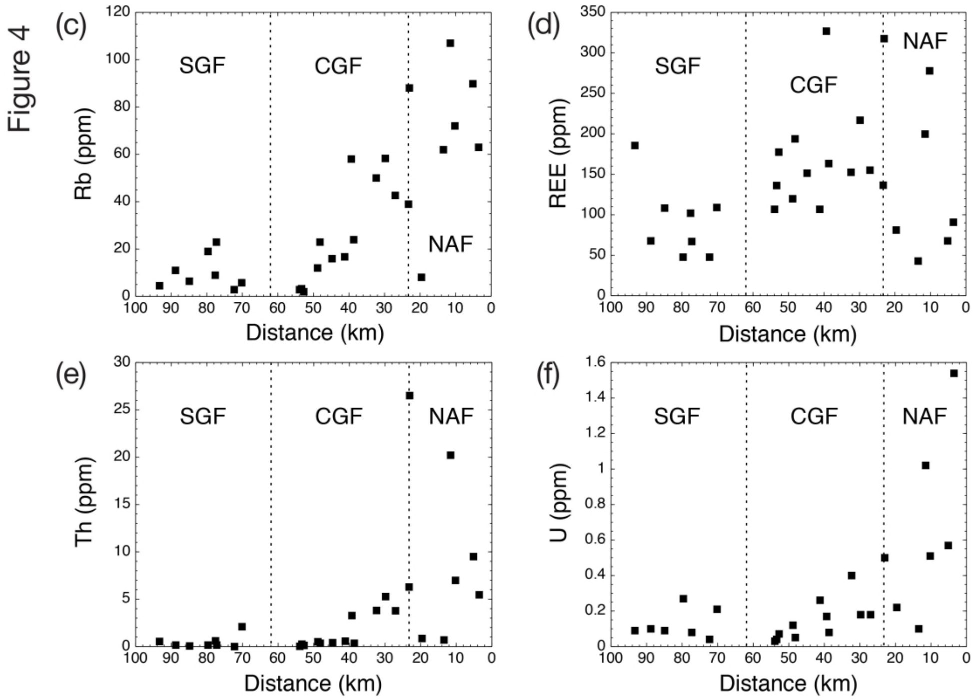

Figure 4: Plot of whole-rock SiO2 (a); Zr (b); Rb (c); REE (d); Th (e); and U (f) as a function of distance along a traverse going southwards from the northernmost sample, i.e. 95 J3 H5, (cf. Fig. 2). Trace element data is taken from Table 2. Whole rock data is taken from Electronic Supplementary Appendix 7a. Dotted lines designate the approximate boundaries between the higher-grade, southern granulite-facies zone (SGF), the lower-grade, central granulite-facies zone (CGF), and the northern amphibolite-facies zone (NAF).

281x203mm (300 x 300 DPI)

Figure 5

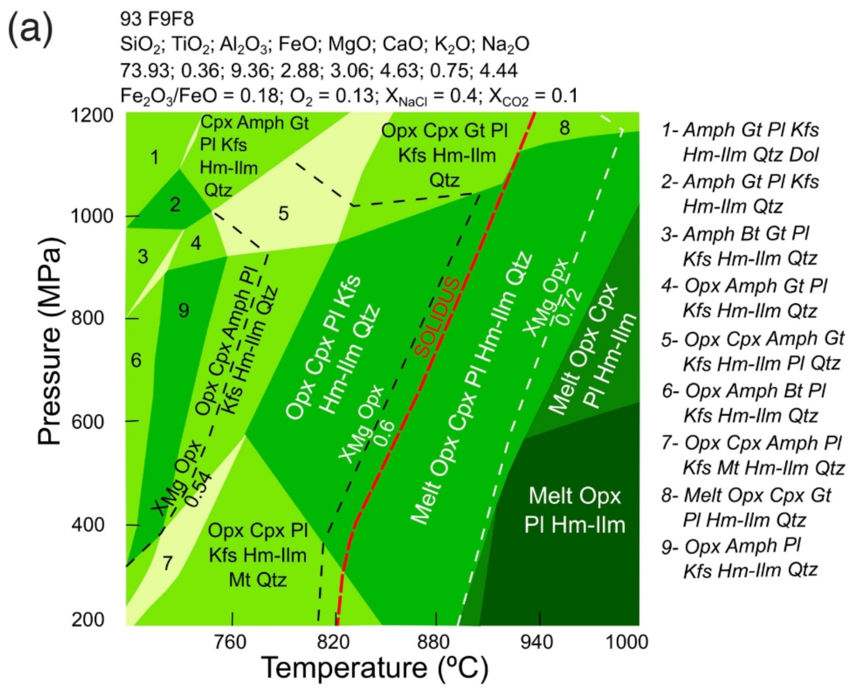

Figure 5: Pseudo-section plots for sample 93 F9 F8 for XNaCl = 0.4, XCO2 = 0.1 (a); XCO2 = 0.8 (b); XNaCl = 0.5, XCO2 = 0.1 (c); and XCO2 = 0.9 (d). Temperature-pressure, pseudo-section plots (700–1000 °C; 200–1200 MPa) were created using the Holland & Powell (2011) mineral chemical database (hp11ver.dat) implemented in the PerpleX (version 6.7.9) software of Connolly (2005). See text for further explanation.

212x163mm (300 x 300 DPI)

Figure 5

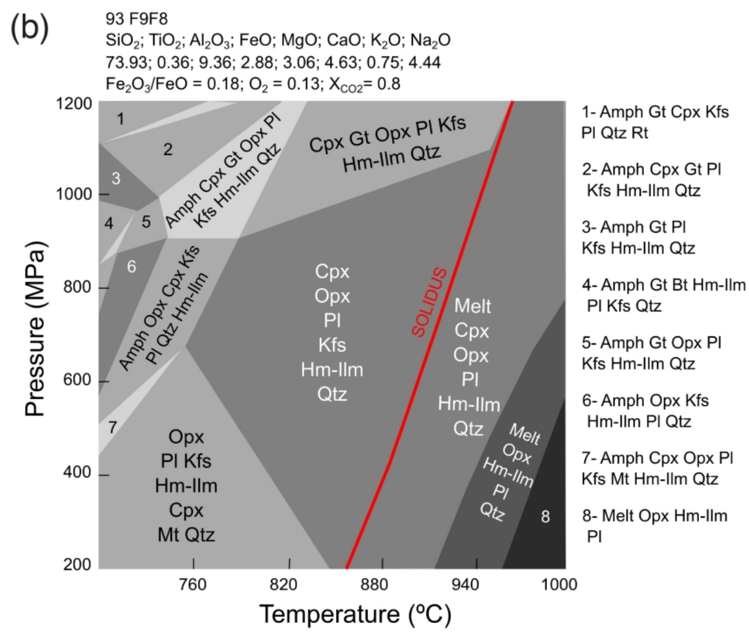

Figure 5: Pseudo-section plots for sample 93 F9 F8 for XNaCl = 0.4, XCO2 = 0.1 (a); XCO2 = 0.8 (b); XNaCl = 0.5, XCO2 = 0.1 (c); and XCO2 = 0.9 (d). Temperature-pressure, pseudo-section plots (700–1000 °C; 200–1200 MPa) were created using the Holland & Powell (2011) mineral chemical database (hp11ver.dat) implemented in the PerpleX (version 6.7.9) software of Connolly (2005). See text for further explanation.

252x176mm (300 x 300 DPI)

Figure 5

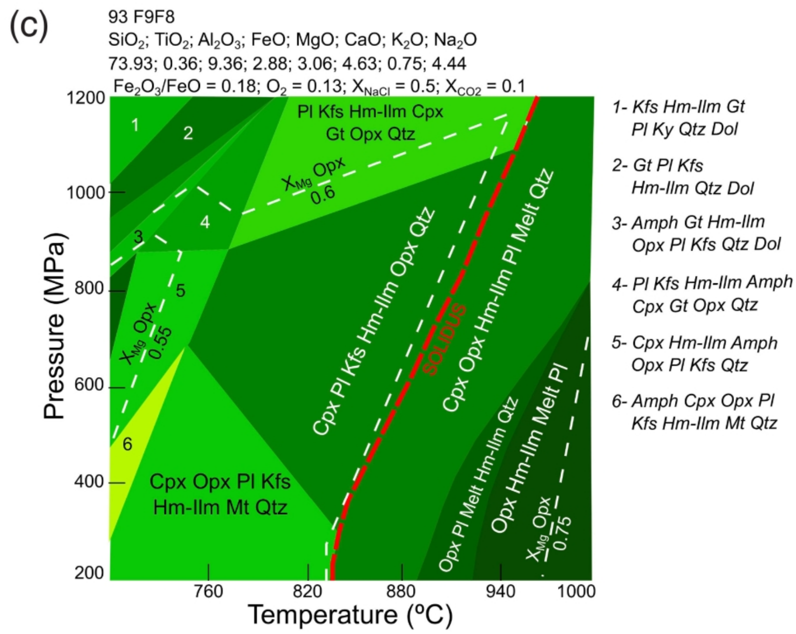

Figure 5: Pseudo-section plots for sample 93 F9 F8 for XNaCl = 0.4, XCO2 = 0.1 (a); XCO2 = 0.8 (b); XNaCl = 0.5, XCO2 = 0.1 (c); and XCO2 = 0.9 (d). Temperature-pressure, pseudo-section plots (700–1000 °C; 200–1200 MPa) were created using the Holland & Powell (2011) mineral chemical database (hp11ver.dat) implemented in the PerpleX (version 6.7.9) software of Connolly (2005). See text for further explanation.

235x170mm (300 x 300 DPI)

Figure 5

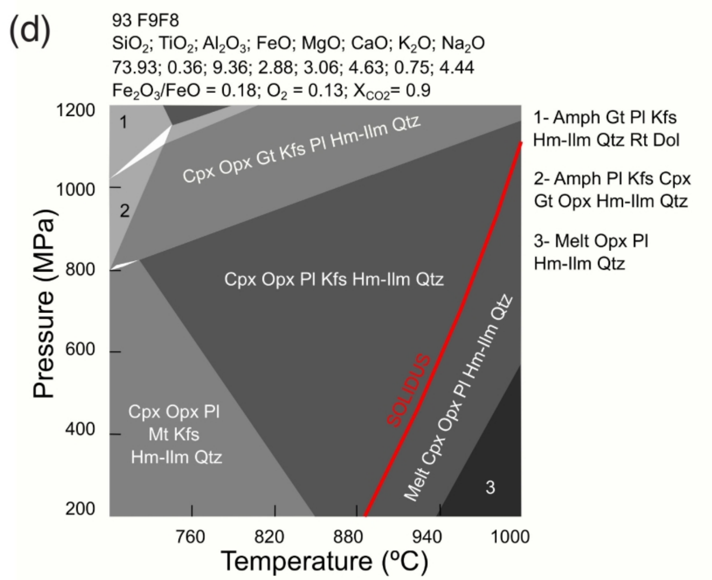

Figure 5: Pseudo-section plots for sample 93 F9 F8 for XNaCl = 0.4, XCO2 = 0.1 (a); XCO2 = 0.8 (b); XNaCl = 0.5, XCO2 = 0.1 (c); and XCO2 = 0.9 (d). Temperature-pressure, pseudo-section plots (700–1000 °C; 200–1200 MPa) were created using the Holland & Powell (2011) mineral chemical database (hp11ver.dat) implemented in the PerpleX (version 6.7.9) software of Connolly (2005). See text for further explanation.

233x163mm (300 x 300 DPI)

Figure 6

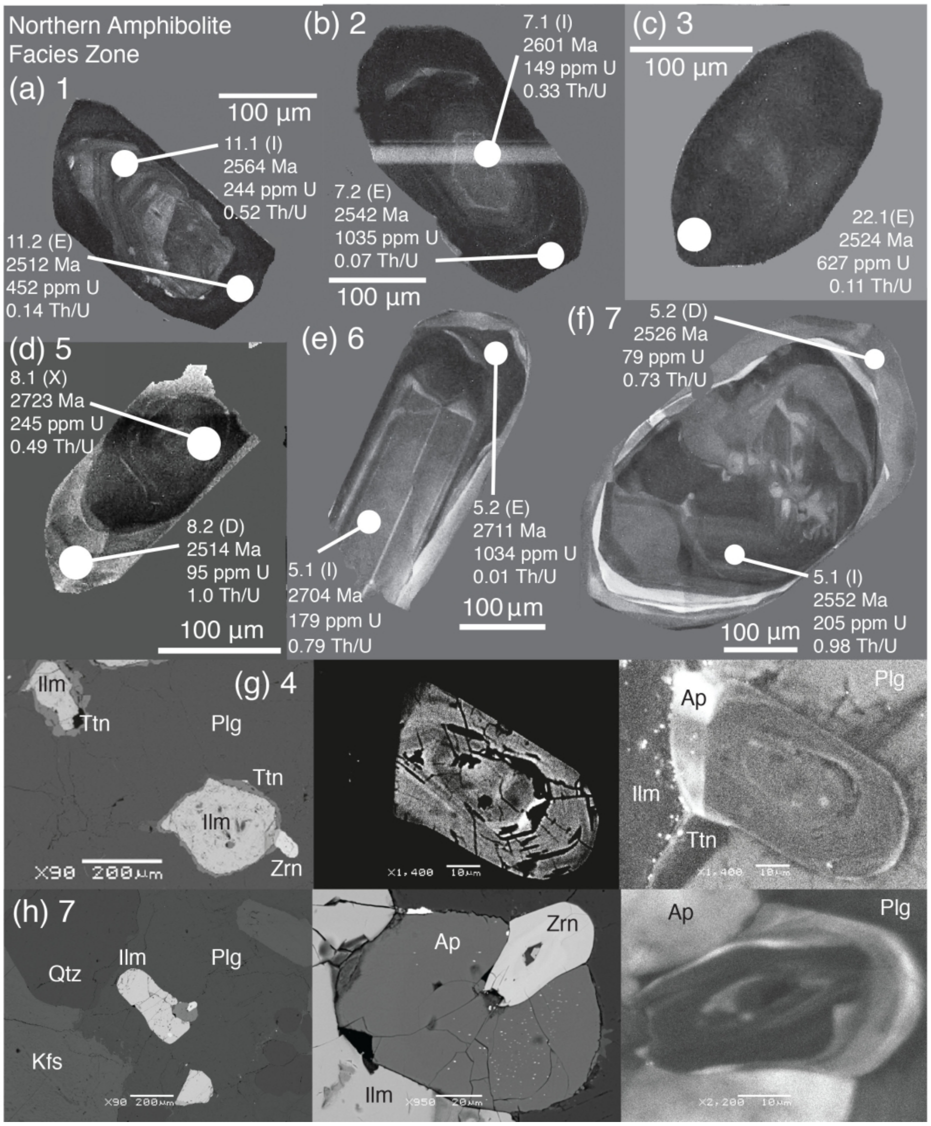

Figure 6: BSE and CL image examples of zircon separates (a – f) and in situ zircons (g, h) from the NAF, Shevaroy Block traverse (cf. Tables 1 & 3; Fig. 2). The sample number corresponding to the sample number in Table 3 is given after the letter designating the image (see also Table 1 and Fig. 2a). In the SHRIMP analytical spot label, the first line designates the spot number. The letter associated with the spot number designates igneous (I), xenocrystic (X), high U metamorphic rim (E), and low U metamorphic rim (D) (cf. Table 3). The second line designates the age, the third line the amount of U measured, and the fourth line the Th/U ratio (cf. Table 3).

209x265mm (300 x 300 DPI)

Figure 7

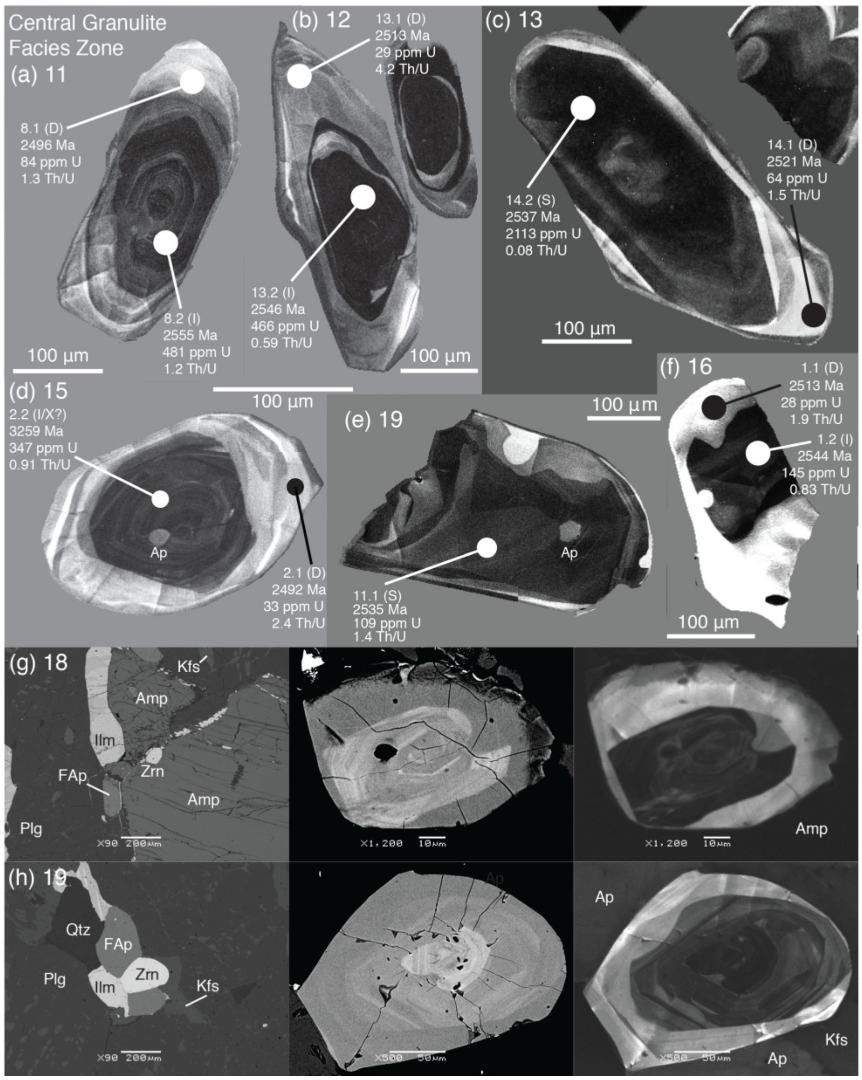

Figure 7: BSE and CL image examples of zircon separates (a – f) and in situ zircons (g, h) from the CGF, Shevaroy Block traverse (cf. Tables 1 & 3; Fig. 2). The sample number corresponding to the sample number in Table 3 is given after the letter designating the image (see also Table 1 and Fig. 2a). In the SHRIMP analytical spot label, the first line designates the spot number. The letter associated with the spot number designates igneous (I), xenocrystic (X), sector zoned (S), and low U metamorphic rim (D) (cf. Table 3). The second line designates the age, the third line the amount of U measured, and the fourth line the Th/U ratio (cf. Table 3).

203x266mm (300 x 300 DPI)

Figure 8

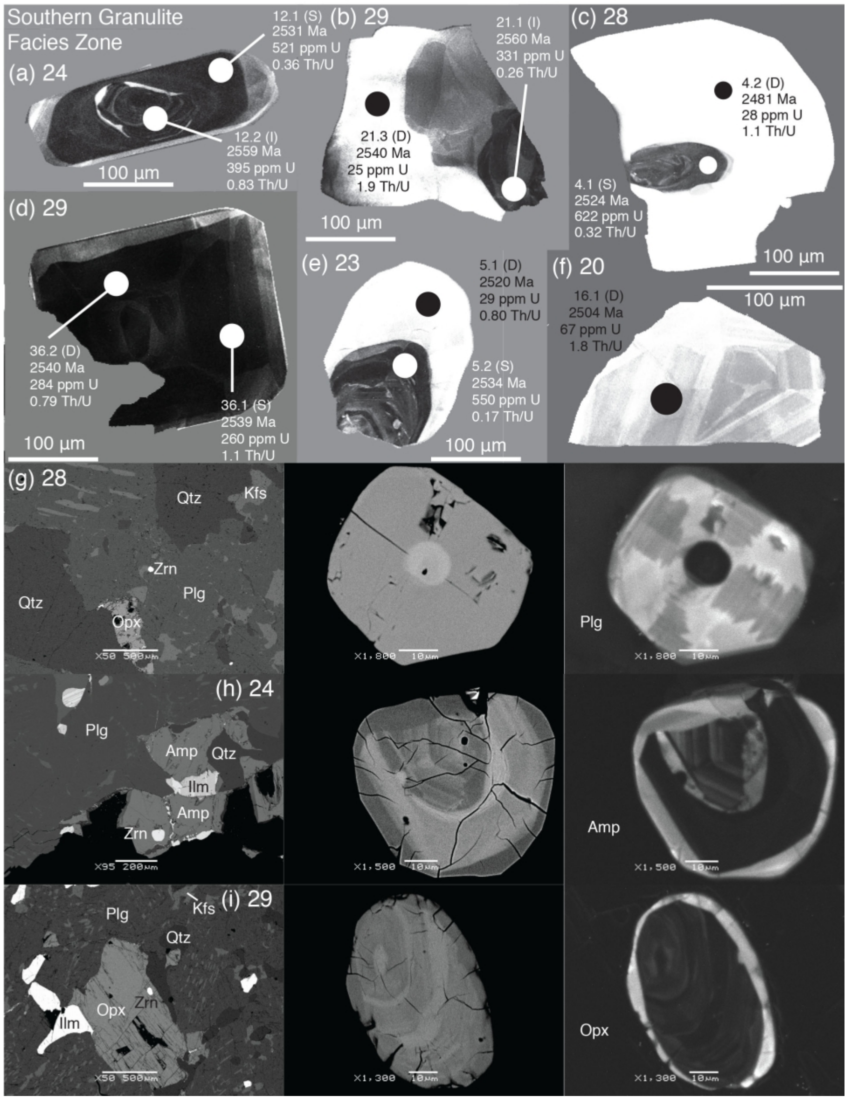

Figure 8: BSE and CL image examples of zircon separates (a – f) and in situ zircons (g – i) from the SGF with the exception of those from sample 20, which is from the southern edge of the CGF (cf. Tables 1 & 3; Fig. 2). The sample number corresponding to the sample number in Table 3 is given after the letter designating the image (see also Table 1 and Fig. 2a). In the SHRIMP analytical spot label, the first line designates the spot number. The letter associated with the spot number designates igneous (I), sector zoned (S), and low U metamorphic rim (D) (cf. Table 3). The second line designates the age, the third line the amount of U measured, and the fourth line the Th/U ratio (cf. Table 3).

197x265mm (300 x 300 DPI)

Figure 9

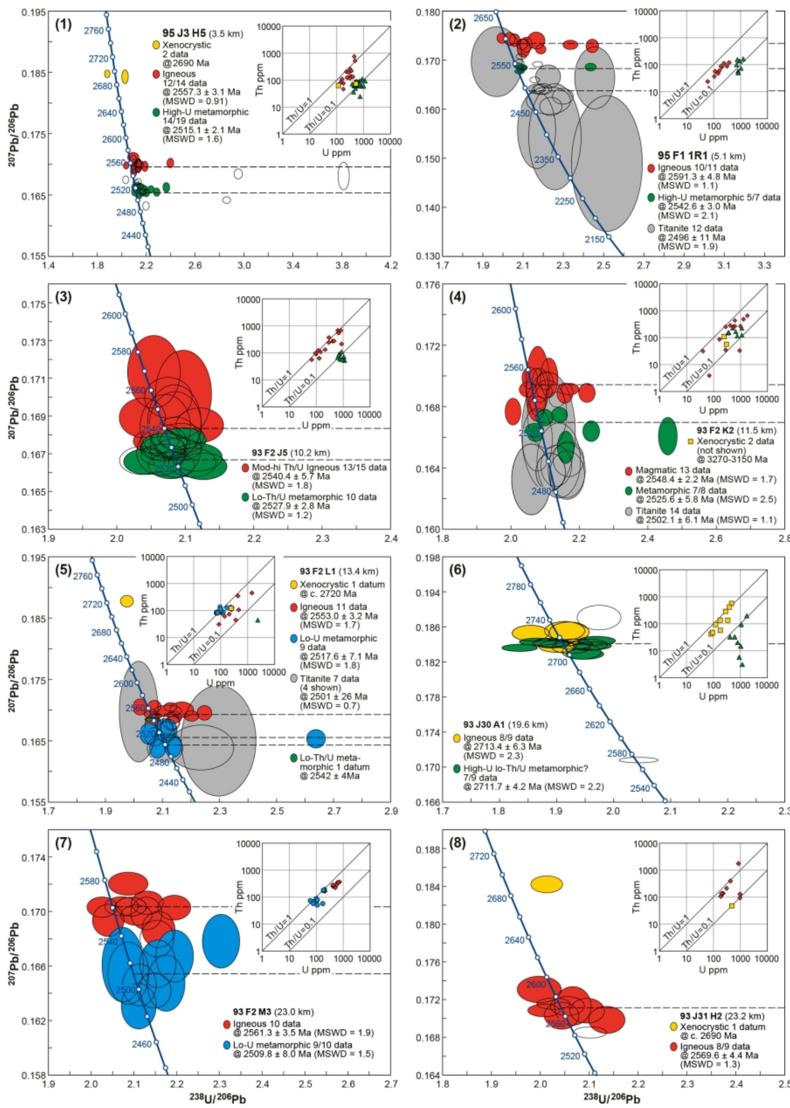

Figure 9: Concordia Tera-Wasserburg plots for zircons from the 29 samples along the Shevaroy Block traverse (see also Fig. 2a and Tables 1 & 3). Sample labels in Figure 2 and the Tables are designated after each of the simplified sample numbers. Label definition and colour code are given in the figure legend. Open ellipses refer to age data not used in the age estimate (see Electronic Supplementary Appendix 4). The dashed horizontal lines refer to the weighted mean age estimates for generations of zircon growth and for titanite growth, as summarized, in Table 5. Xenocrystic analyses (yellow symbols) plotted in the Th vs. U plot are not plotted on the concordia for samples 4, 9, and 11.

178x264mm (300 x 300 DPI)

Figure 9 (con.)

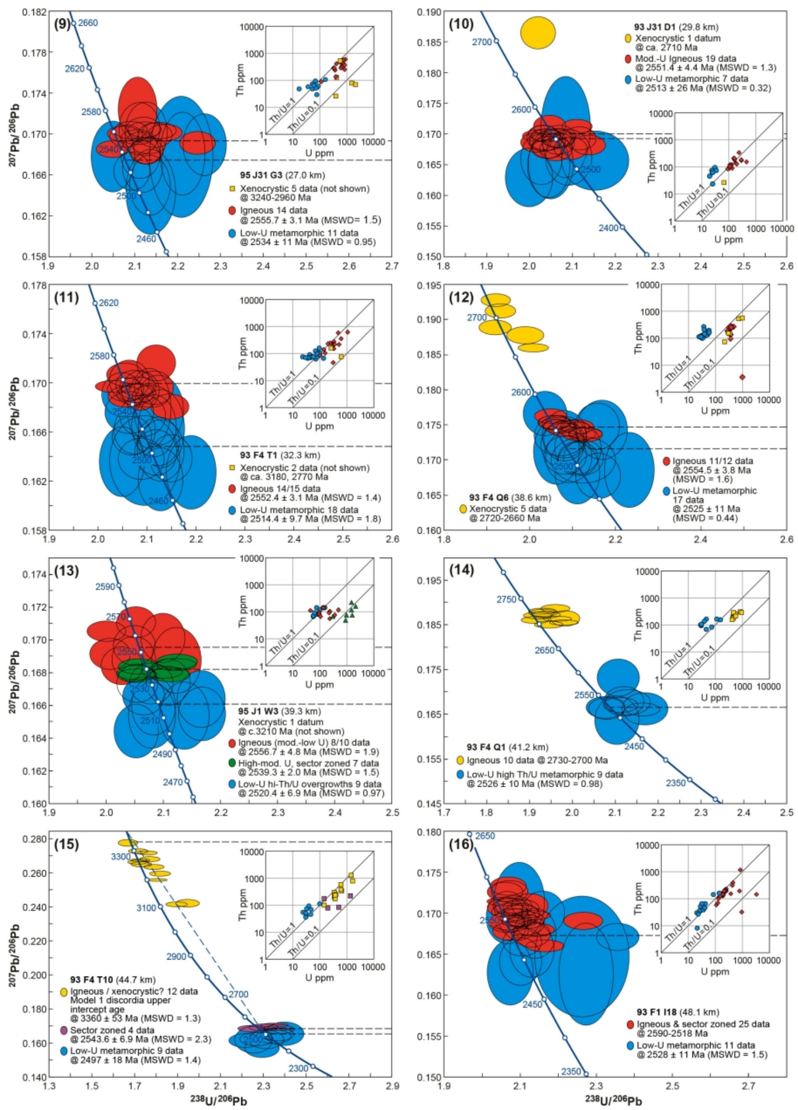

Figure 9: Concordia Tera-Wasserburg plots for zircons from the 29 samples along the Shevaroy Block traverse (see also Fig. 2a and Tables 1 & 3). Sample labels in Figure 2 and the Tables are designated after each of the simplified sample numbers. Label definition and colour code are given in the figure legend. Open ellipses refer to age data not used in the age estimate (see Electronic Supplementary Appendix 4). The dashed horizontal lines refer to the weighted mean age estimates for generations of zircon growth and for titanite growth, as summarized, in Table 5. Xenocrystic analyses (yellow symbols) plotted in the Th vs. U plot are not plotted on the concordia for samples 4, 9, and 11.

178x263mm (300 x 300 DPI)

Figure 9 (con.)

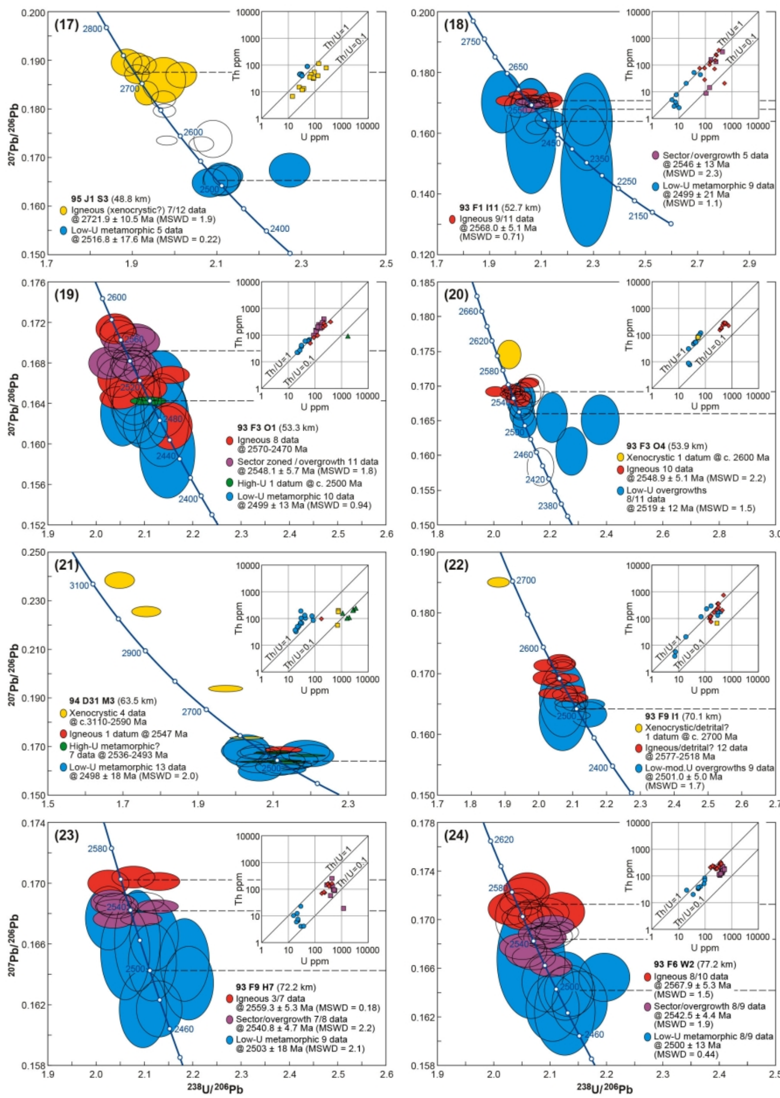

Figure 9: Concordia Tera-Wasserburg plots for zircons from the 29 samples along the Shevaroy Block traverse (see also Fig. 2a and Tables 1 & 3). Sample labels in Figure 2 and the Tables are designated after each of the simplified sample numbers. Label definition and colour code are given in the figure legend. Open ellipses refer to age data not used in the age estimate (see Electronic Supplementary Appendix 4). The dashed horizontal lines refer to the weighted mean age estimates for generations of zircon growth and for titanite growth, as summarized, in Table 5. Xenocrystic analyses (yellow symbols) plotted in the Th vs. U plot are not plotted on the concordia for samples 4, 9, and 11.

178x266mm (300 x 300 DPI)

Figure 9 (con.)

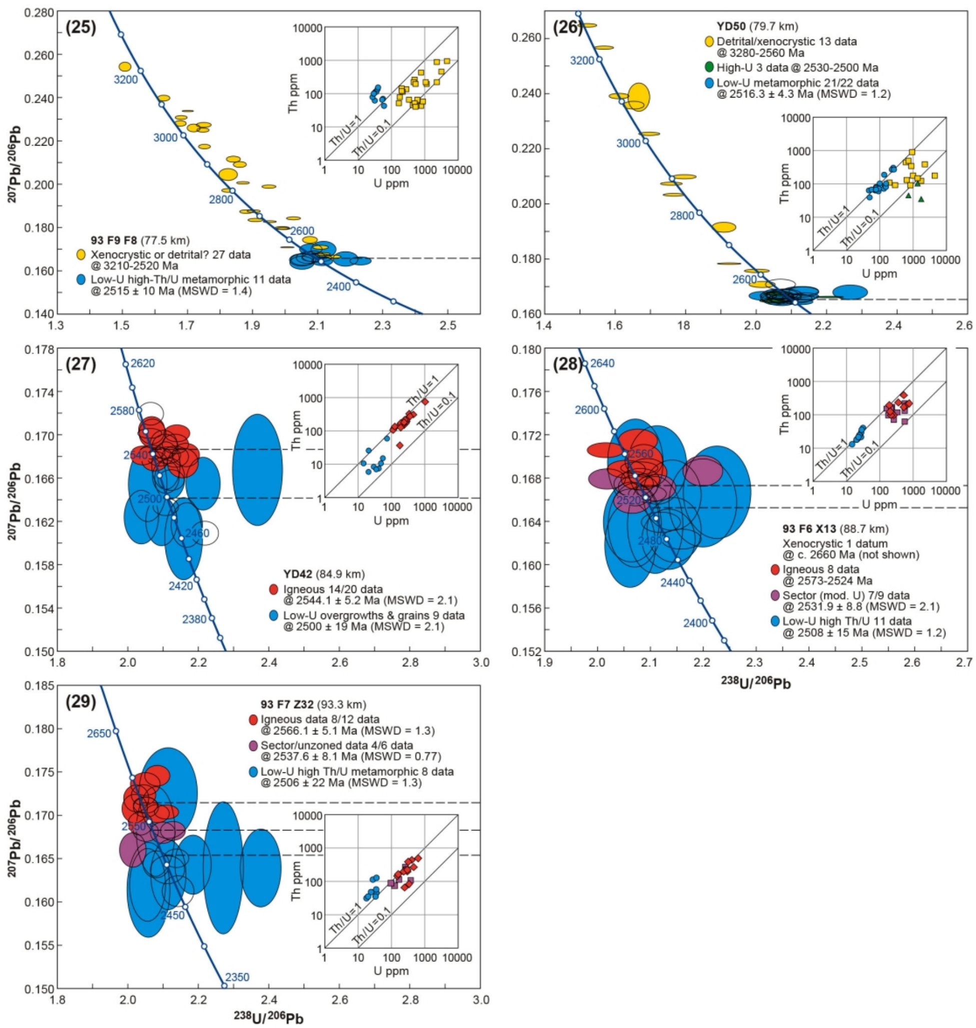

Figure 9: Concordia Tera-Wasserburg plots for zircons from the 29 samples along the Shevaroy Block traverse (see also Fig. 2a and Tables 1 & 3). Sample labels in Figure 2 and the Tables are designated after each of the simplified sample numbers. Label definition and colour code are given in the figure legend. Open ellipses refer to age data not used in the age estimate (see Electronic Supplementary Appendix 4). The dashed horizontal lines refer to the weighted mean age estimates for generations of zircon growth and for titanite growth, as summarized, in Table 5. Xenocrystic analyses (yellow symbols) plotted in the Th vs. U plot are not plotted on the concordia for samples 4, 9, and 11.

177x204mm (300 x 300 DPI)

Figure 10

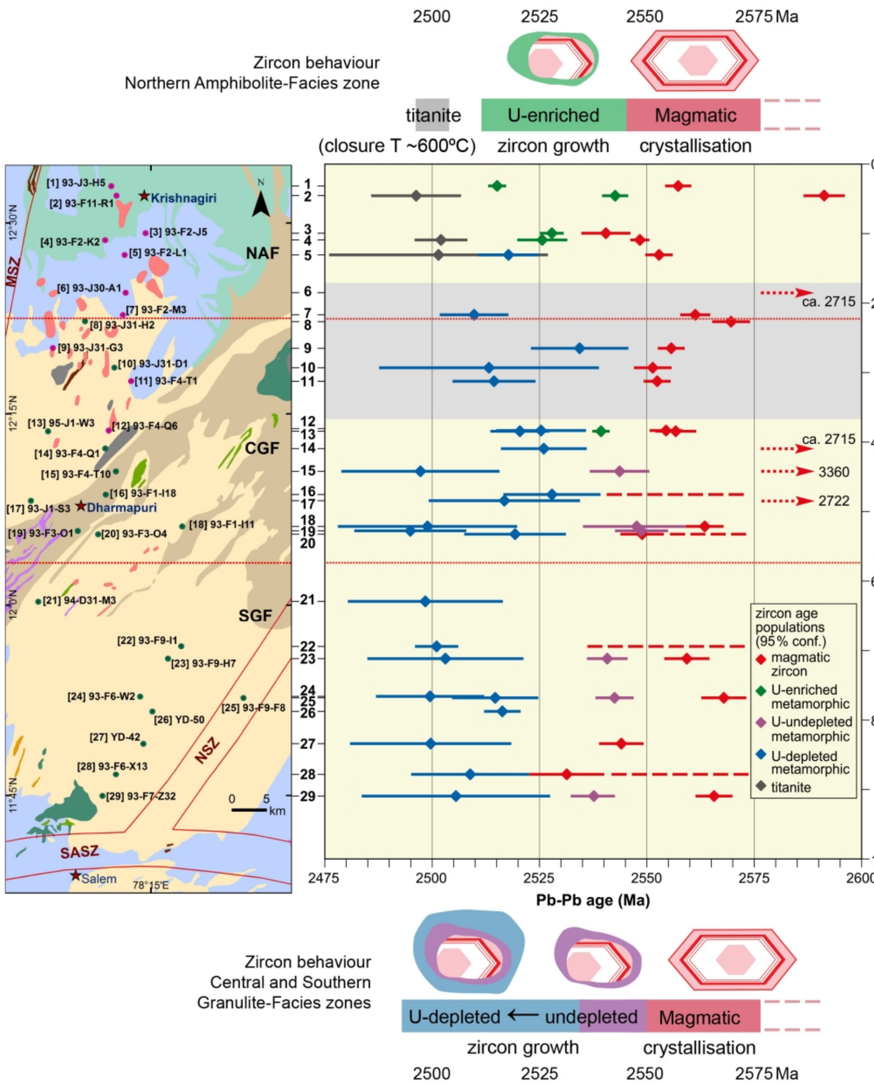

Figure 10: Plot of zircon ages with error bars as a function of location along a stylized depiction of the Shevaroy Block traverse (see Tables 1 & 5 and Fig. 2b). Label definition and colour code are given in the figure legend. Reference to U-enriched/U-undepleted/U-depleted zircon is relative to magmatic zircon in each sample, and not to the data set as a whole (cf. U vs. Th plots in Fig. 9). Sketches of zircon grains show the different responses of magmatic zircon (red) to metamorphism in the Northern Amphibolite Facies (NAF) zone (top), versus metamorphism in the Central Granulite Facies (CGF) and Southern Granulite Facies (SGF) zones (bottom).

175x224mm (300 x 300 DPI)

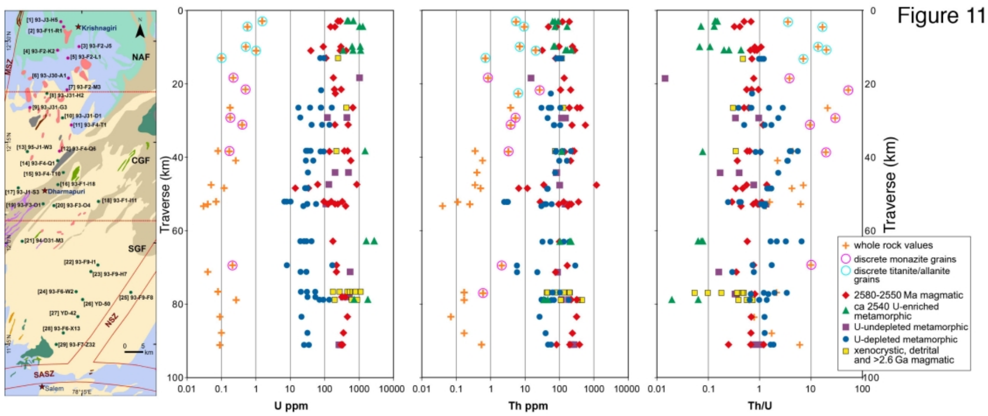

Figure 11: Plot of whole-rock and zircon U and Th abundances and Th/U as a function of distance and metamorphic grade from granulite- (SGF and CGF) to amphibolite-facies (NAF) along with a depiction of the Shevaroy Block traverse (Fig. 2b), which indicates the corresponding sample location of each point in the three plots. Circles around the symbol for whole rock analyses indicate that the sample contains either discrete, independent monazite grains, or titanite rims around ilmenite and allanite grains.

223x94mm (300 x 300 DPI)

Figure 12

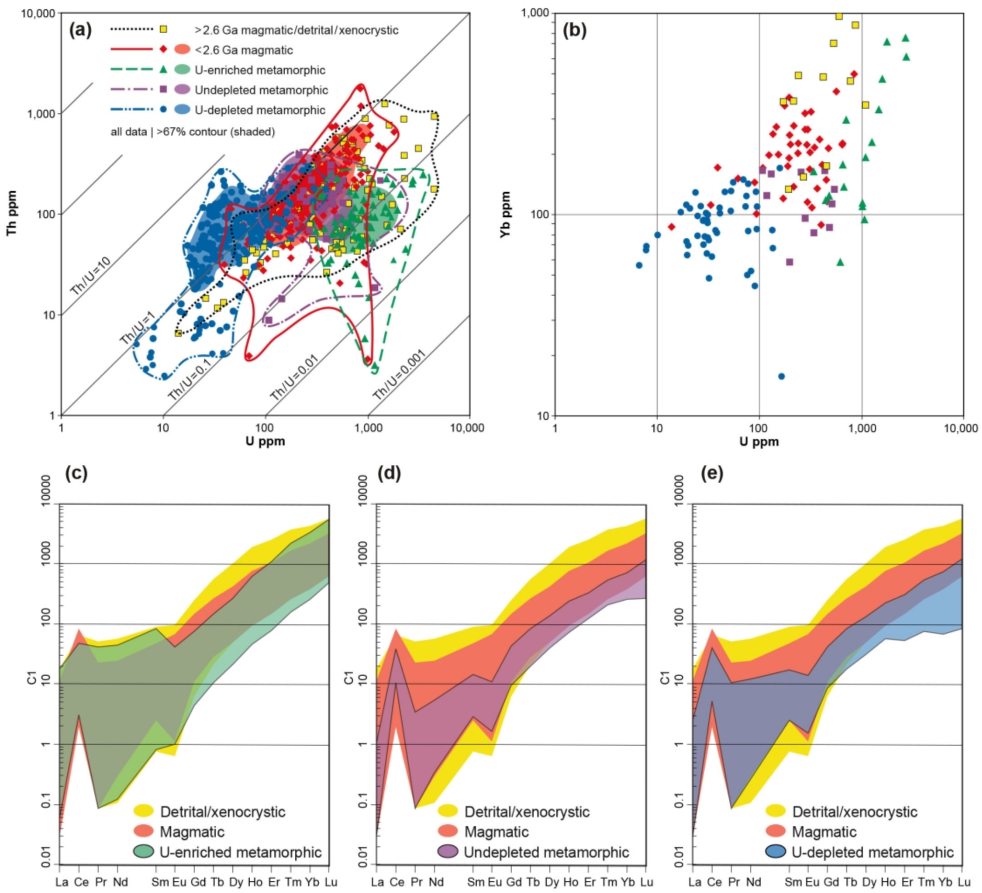

Figure 12: Scatter plot of zircon trace element (ppm) U vs. Th (a) and U vs. Yb (b). For each zircon type lines enclose the full data set whereas shaded areas enclose 67% of the data set. Chondrite (C1) normalized (McDonough & Sun, 1995) zircon REE plots of detrital/xenocrystic, magmatic, and U-enriched metamorphic areas in the zircon (c), detrital/xenocrystic, magmatic, and undepleted metamorphic areas in the zircon (d), and detrital/xenocrystic, magmatic, and U-depleted metamorphic areas in the zircon (e).

186x193mm (300 x 300 DPI)

Table 1: Mineralogy of the Shevaroy Block gneiss samples

#	HH	Sample	Zone	D (km)	Latitude	Longitude	Ep	Gt	Opx	Cpx	Amph	Bt	Kfs Blebs†	Mt	Ilm	Py	Po	Cp	Titanite	Allanite	FAp	Monazite	Zircon**
1	2	95 J3 H5	NAF	3,54	12°32'54"	78°11'53"	X				X	X	coarse		D				D, **R**		X		x, I, E
2	4	93 F11 R1	NAF	5,09	12°32'09"	78°12'18"	X				X	X		D	D				D, **R**		X		I, e
3		93 F2 J5	NAF	10,18	12°29'13"	78°14'35"					X	X		RS, V	D	D			D, R	RA	X	SIA (one example)	I, E
4	7	93 F2 K2	NAF	11,50	12°28'40"	78°11'24"					X	X	coarse	D, IL	D				D, **R**-R	D	X		I, E
5	8	93 F2 L1	NAF	13,39	12°27'30"	78°12'56"					X	X		V					D	D, RA	X*	SIA	x, I, e, D
6	11	93 J30 A1	NAF	19,58	12°24'32"	78°13'01"					X	X	fine	D, IL	Mt	Mt				RA, RM	X	D, SIA, LIA, RA	I, e?, d
7	13	93 F2 M3	NAF	23,01	12°22'47"	78°12'48"				X		X		D, V, IL, RS						RA	X	D, SIA, LIA, RA	I, e?, d
8	14	93 J31 H2	CGF	23,23	12°22'16"	78°09'49"			X	X	X	X		D, V, IL						D	X	SIA, LIA, RA	x, I, s, d
9	17	93 J31 G3	CGF	26,99	12°20'10"	78°07'18"				X		X	coarse	D, IL, RS	Mt					RA	X	SIA, LIA, RA	I, s, D
10	19	93 J31 D1	CGF	29,76	12°18'38"	78°12'08"			X	X		X	coarse, RAP	D, IL	Mt	Mt				RA	X	D, SIA, LIA, RA	x, I, s, d
11	22	93 F4 T1	CGF	32,30	12°17'34"	78°13'27"				X		X	coarse	D, V, IL	Mt	Mt, Man		Py		RA	X	D, SIA, LIA, RA	I, s, D
12	25	93 F4 Q6	CGF	38,61	12°13'42"	78°11'41"					X	X	moderate, RAP	D, IL	D, Mt, HL					RA	X	SIA, LIA, RA	x, I,s, d
13	26	95 J1 W3	CGF	39,27	12°13'38"	78°06'55"			X	X		X		D, IL	Mt	D		D, Py		RA	X	D, SIA, LIA, RA	X, I, S, d
14	27	93 F4 Q1	CGF	41,15	12°12'17"	78°11'25"			X		X	X	coarse	D, V, IL	Mt	Mt, Man				RA	X	SIA, LIA, RA	I, S, D
15	28	93 F4 T10	CGF	44,69	12°10'29"	78°12'15"			X		X	X	coarse	D, V	D, Mt, ML	Mt, Man		Py		RA (rare)	X	SIA, LIA, RA	i, S, D
16	31	93 F1 I18	CGF	48,12	12°08'40"	78°11'27"			X	X	X	X	coarse	D, RS, V	D, HL, Mt	D, Man, Mt		D, Py			X	LIA, RA	I/S?, D
17	32	95 J1 S3	CGF	48,78	12°08'11"	78°05'34"			X	X	X	X	coarse	3Ox, D, V, RS	D, Mt, HL, ML	D, Mt, Man, V				RA (rare)	X	SIA, LIA, RA	I, s?, D
18		93 F1 I11	CGF	52,66	12°06'10"	78°17'28"			X	X	X	X	fine, RAP	D, RS, V	D, HL, Mt	D, Mt, Ilm				RA	X	SIA, LIA, RA	I, S, D
19		93 F3 O1	CGF	53,32	12°05'49"	78°09'15"			X	X	X	X	moderate, RAP	D, RS, V	D, HL, Mt	D, Mt		Py		RA	X	LIA, RA	i, e, S, D
20		93 F3 O4	CGF	53,87	12°05'33"	78°10'51"			X	X		X	moderate, RAP	no thin section						RA	X	LIA, RA	x, I, s, D
21		94 D31 M3	SGF	63,50	12°00'16"	78°06'09"			X	X	X	X	moderate, RAP	D, RS, V	D, HL, Mt	D, Mt, Man, V, Cp		Py		RA	X	LIA, RA	x, I, e, D
22	36	93 F9 I1	SGF	70,13	11°56'44"	78°17'23"	X	X	X			X	moderate	D, V	D	D, V, Po, Mt	D, Cp, Py	Py, Po			X	D*, SIA, RA	P, s, D
23		93 F9 H7	SGF	72,23	11°55'46"	78°16'21"			X	X		X	coarse, RAP	D, V, RS	D, HL, Mt	D, V, Man					X	LIA, SIA, RA	i, S, D
24		93 F6 W2	SGF	77,21	11°52'47"	78°14'09"			X		X	X	coarse, RAP	D,V	D	D, Man	D	Po		RA	X	LIA, SIA, RA	i, S, D
25	39	93 F9 F8	SGF	77,54	11°52'41"	78°22'17"			X		X	X	moderate	V	D	D,V, Man		Po		RA	X	D*, SIA, RA	P?, s, D
26	41	YD 50	SGF	79,65	11°51'37"	78°15'07"			X			X		RS	D, HL	D, Man	D	Py, Po			X	SIA	p?, e, D
27	43	YD 42	SGF	84,85	11°49'02"	78°14'24"			X			X	coarse, RAP	D, V, RS	D, HL	D, Mt, V, Man				RA	X	LIA, RA	i, s, D
28	44	93 F6 X13	SGF	88,72	11°46'40"	78°12'15"			X		X		coarse, RAP	D	D	D, Man	D	Po		RA	X	LIA, RA	i, S, D
29	48	93 F7 Z32	SGF	93,25	11°44'58"	78°11'12"			X		X		coarse, RAP	D	D, HL	D				RA	X	SIA, LIA	i, s, D

HH = Hansen & Harlov (2007) sample number.

Mineral Abbreviations
Opx = Orthopyroxene; Cpx = Clinopyroxene; Gt = Garnet; Amph = Amphibole; Bt = Biotite; Ep - epidote; Kfs - K-feldspar; FAp - fluorapatite; Mt = Magnetite; Ilm = Ilmenite; Py = Pyrite; Po = pyrrhotite; Cp = Chalcopyrite.
† - Kfs blebs are primarily found along plagioclase-quartz grain boundaries. RAP - replacement antiperthite.

Phosphates and Allanite
* - a sparse scattering of small monazite inclusions are found in one fluorapatite grain. ‡ - fluorapatite grains are magmatically zoned. D - Discrete grain; D* - one or two small discrete Th-poor grains.
SIA - numerous small Mnz inclusions in fluorapatite. LIA - large Mnz inclusions in fluorapatite; RA - rims fluorapatite; RM - rims monazite grain.

Zircon
** - zircon types: uppercase - dominant type; lowercase: minor component. X - xenocrystic; P - detrital; I - igneous (euhedral / oscillatory zoned); E - enriched (low-CL) metamorphic; S - sector zoned / graduated / unzoned; D - depleted (high-CL) metamorphic.

Oxides and Sulfides
D = discrete euhedral to anhedral grains; V = veins; Mt = associated with magnetite. For titanite - **R** = thick rims around ilmenite; R = thin rims around ilmenite.
For oxides - 3Ox = three oxide grains consisting of ilmenite grains with laths of magnetite and hematite lamellae in the ilmenite; RS = magnetite rimming pyroxenes and amphiboles;
HL = hematite lamellae in ilmenite; IL = ilmenite laths in magnetite; ML = magnetite laths in ilmenite. For the sulfides: Py = associated with pyrite; Man = magnetite mantle around pyrite.

Table 2: Whole rock trace element analyses (ppm) from the Shevaroy Block gneisses

#	Sample	Zone	D (km)	Latitude	Longitude	Rb	Sr	Zr	Nb	Cs	Ba	Hf	Ta	Pb	Th	U	Y	La	Ce	Pr	Nd	Sm	Eu	Gd	Tb	Dy	Ho	Er	Tm	Yb	Lu	Sum REE
1	95 J3 H5	NAF	3,54	12°32'54"	78°11'53"	63,0		93				2,20		26,0	5,46	1,54		20,8	42,1	3,80	15,9	2,52	0,65	2,08	0,24	1,14	0,21	0,64	0,09	0,62	0,09	90,9
2	93 F11 R1*	NAF	5,09	12°32'09"	78°12'18"	89,8	377	103	2,90	0,25	722	2,91	0,10	18,7	9,50	0,57	1,96	18,9	32,1	3,13	9,84	1,21	0,86	0,62	0,07	0,38	0,07	0,22	0,03	0,21	0,03	67,7
3	93 F2 J5*	NAF	10,18	12°29'13"	78°14'35"	72,0		209	14,0	0,20	667	6,10		15,0	7,00	0,51	38,0	49,2	108	13,98	64,6	12,1	2,10	10,1	1,36	6,93	1,25	3,69	0,60	3,48	0,49	278
4	93 F2 K2	NAF	11,50	12°28'40"	78°11'24"	107		129				3,40		39,0	20,2	1,02		57,9	96,0	8,53	28,7	3,04	0,77	2,97	0,17	0,74	0,13	0,38	0,04	0,29	0,05	200
5	93 F2 L1	NAF	13,39	12°27'30"	78°12'56"	62,0		103				3,00		14,0	0,70	0,10		13,0	20,0	1,72	5,50	0,70	0,77	0,40	0,10	0,20	0,10	0,10	0,05	0,10	0,03	42,8
6	93 J30 A1	NAF	19,58	12°24'32"	78°13'01"	8,10		57				1,60		12,0	0,84	0,22		14,7	32,9	3,56	15,7	3,29	1,18	3,02	0,45	2,44	0,49	1,43	0,21	1,37	0,20	80,9
7	93 F2 M3	NAF	23,01	12°22'47"	78°12'48"	88,0									26,5	0,50		100	161		48,0	5,61	1,98		0,40					0,58	0,06	318
8	93 J31 H2	CGF	23,23	12°22'16"	78°09'49"	39,0									6,30			36,8	68,0		26,0	3,75	1,23		0,40					0,45	0,06	137
9	93 J31 G3*	CGF	26,99	12°20'10"	78°07'18"	42,7	646	101	3,92	0,07	511	2,37	0,08	10,6	3,77	0,18	5,42	42,9	71,9	7,11	23,8	3,22	1,36	2,11	0,24	1,21	0,22	0,49	0,06	0,36	0,05	155
10	93 J31 D1*	CGF	29,76	12°18'38"	78°12'08"	58,3	552	147	3,05	0,03	607	3,44	0,05	10,0	5,27	0,18	11,1	54,5	97,8	10,4	37,4	5,78	1,44	4,02	0,49	2,45	0,43	1,06	0,13	0,78	0,11	217
11	93 F4 T1	CGF	32,30	12°17'34"	78°13'27"	50,0									3,80	0,40		42,5	75,0		28,0	4,06	1,64		0,50					0,58	0,09	152
12	93 F4 Q6*	CGF	38,61	12°13'42"	78°11'41"	24,0	1258	79,20	2,19	<0.005	1143	1,95	0,08	13,4	0,35	0,08	6,67	40,4	73,7	8,01	29,6	4,37	1,49	2,66	0,30	1,36	0,23	0,63	0,08	0,48	0,06	163
13	95 J1 W3	CGF	39,27	12°13'38"	78°06'55"	58,0		218				5,10		18,0	3,28	0,17		74,9	135	15,6	66,5	10,9	2,10	9,69	1,10	5,08	0,88	2,64	0,36	1,83	0,25	327
14	93 F4 Q1*	CGF	41,15	12°12'17"	78°11'25"	16,7	406	139	3,08	0,02	372	3,53	0,11	8,17	0,58	0,26	5,79	28,0	48,7	4,92	16,9	2,48	0,96	1,77	0,23	1,17	0,21	0,63	0,08	0,53	0,08	107
15	93 F4 T10	CGF	44,69	12°10'29"	78°12'15"	16,0									0,40			38,7	72,0		32,0	5,28	1,43		0,60					1,04	0,14	151
16	93 F1 I18*	CGF	48,12	12°08'40"	78°11'27"	23,0	592	129	6,20	0,01	572			8,80	0,35	0,05	29,0	33,7	79,2	10,5	40,6	8,14	1,67	7,05	0,95	5,18	0,98	2,72	0,38	2,47	0,35	194
17	95 J1 S3	CGF	48,78	12°08'11"	78°05'34"	12,0		187				4,60		11,0	0,51	0,12		28,9	53,6	5,39	21,9	3,18	0,99	2,80	0,27	1,23	0,22	0,55	0,08	0,45	0,08	120
18	93 F1 I11	CGF	52,66	12°06'10"	78°17'28"	2,00		171				3,70		10,0	0,11	0,07		38,4	75,7	8,26	36,0	5,78	1,65	5,06	0,58	2,75	0,50	1,46	0,18	1,08	0,15	178
19	93 F3 O1*	CGF	53,32	12°05'49"	78°09'15"	3,20	598	179	5,60	<0.005	395			13,0	0,25	0,04	23,0	25,4	54,0	6,92	27,3	5,81	1,59	5,32	0,72	3,91	0,73	1,99	0,27	1,81	0,26	136
20	93 F3 O4*	CGF	53,87	12°05'33"	78°10'51"	2,90	584	77	6,10	0,37	332			9,40	0,04	0,03	12,0	25,4	46,3	5,27	19,2	2,91	1,19	2,41	0,30	1,50	0,29	0,82	0,12	0,84	0,13	107
21	94 D31 M3	SGF	63,50	12°00'16"	78°06'09"																											
22	93 F9 I1*	SGF	70,13	11°56'44"	78°17'23"	5,76	283	82,9	5,05	<0.005	350	2,17	0,24	12,0	2,10	0,21	21,8	25,0	44,1	4,61	16,9	3,14	1,26	3,42	0,59	3,82	0,80	2,39	0,34	2,25	0,33	109
23	93 F9 H7*	SGF	72,23	11°55'46"	78°16'21"	2,90	592	105	1,80	<0.005	361			6,60	<0.005	0,04	7,00	13,1	21,1	2,23	7,19	1,02	0,89	0,82	0,10	0,45	0,08	0,23	0,04	0,23	0,04	47,5
24	93 F6 W2*	SGF	77,21	11°52'47"	78°14'09"	23,0	478	101	3,20	0,01	762			8,60	0,17	0,08	7,00	19,6	30,6	3,08	9,28	1,20	1,01	0,91	0,11	0,52	0,10	0,29	0,04	0,32	0,05	67,1
25	93 F9 F8	SGF	77,54	11°52'41"	78°22'17"	9,00									0,60			29,2	49,0		19,0	2,55	1,36		0,30					0,56	0,10	102
26	YD 50*	SGF	79,65	11°51'37"	78°15'07"	19,0	361	193	2,70	0,03	400			8,60	0,17	0,27	5,00	15,5	21,2	2,00	5,61	0,64	0,91	0,50	0,06	0,36	0,08	0,29	0,05	0,40	0,07	47,7
27	YD 42*	SGF	84,85	11°49'02"	78°14'24"	6,37	637	68,3	5,00	<0.005	639	1,64	0,11	6,95	0,07	0,09	11,1	21,6	43,5	5,44	22,8	4,44	1,47	3,44	0,43	2,33	0,41	1,13	0,15	0,90	0,13	108
28	93 F6 X13*	SGF	88,72	11°46'40"	78°12'15"	11,0	616	81,5	3,68	<0.005	647	1,89	0,09	7,75	0,17	0,10	3,84	18,1	29,9	3,10	11,0	1,60	1,10	1,17	0,14	0,71	0,15	0,40	0,05	0,39	0,06	67,9
29	93 F7 Z32*	SGF	93,25	11°44'58"	78°11'12"	4,47	984	90,8	4,67	<0.005	646	2,00	0,13	7,36	0,54	0,09	12,3	40,4	80,2	9,41	37,1	6,34	1,83	4,36	0,53	2,62	0,46	1,15	0,15	0,90	0,13	186

* - rock samples analysed according to the method set out in Dulski (2001). Blank - element not analysed for.

Table 3: Representative SHRIMP trace element data for zircon from the Shevaroy Block gneisses

#	Sample	Sector	D(km)	Grain spot .spot	U (ppm)	Th (ppm)	Th/U	$^{207}Pb^*/^{206}Pb^*$ age (Ma)		Disc. (%)	Hf (ppm)	Y	La	Ce	Pr	Nd	Sm	Eu	Gd	Tb	Dy	Ho	Er	Tm	Yb	Lu	Description
												(Y+REE) (ppm)															
1	95 J3 H5	NAF	3,54	11,1	244	122	0,52	2563,5	± 5,8	1	8942	665	0,00	21,6	0,01	0,47	1,56	0,59	9,38	3,53	43,9	17,5	85,8	20,6	224	62,3	Oscillatory and normal faceted zoned cores and grains (magmatic)
				11,2	452	63	0,14	2511,7	± 4,5	2	8728	230	0,20	10,1	0,12	0,73	0,45	0,15	1,77	0,75	11,0	5,09	30,3	9,25	117	36,0	CL-dark overgrowths and replacement textures (metamorphic)
2	93 F11 R1	NAF	5,09	7,1	149	48	0,33	2600,5	± 8,5	1	6723	756	2,06	18,4	2,22	14,8	8,40	2,29	13,5	3,90	45,8	19,4	100	25,2	270	74,4	Oscillatory and normal faceted zoned cores and grains (magmatic zircon)
				7,2	1035	75	0,07	2542	± 3,2	1	10778	348	1,95	17,5	1,62	9,30	4,67	1,21	6,87	2,07	23,1	8,69	41,2	10,3	114	30,3	CL-dark overgrowths and replacement textures (metamorphic)
3	93 F2 J5	NAF	10,18	3,1	91	97	1,10	2571	± 12	1	6291	618	1,61	46,5	1,02	6,82	5,20	1,36	14,8	4,45	47,7	16,6	70,6	15,1	143	33,5	Oscillatory and normal faceted zoned cores and grains (magmatic zircon)
				22,1	627	68	0,11	2523,5	± 5,1	1	7533	146	0,00	9,40	0,00	0,08	0,17	0,09	1,24	0,52	7,45	3,35	18,1	4,81	57,9	16,8	CL-dark overgrowths and replacement textures (metamorphic)
4	93 F2 K2	NAF	11,50	13,2	418	276	0,68	2557	± 4,6	0	8496	547	2,70	48,4	1,95	10,7	5,91	1,05	11,6	3,46	38,4	14,6	70,0	16,5	175	47,0	Oscillatory and normal faceted zoned cores and grains (magmatic zircon)
				13,1	345	150	0,45	2511,7	± 7,1	2	8709	490	6,19	43,0	4,81	29,1	17,8	2,25	21,2	4,58	39,5	13,0	60,8	15,0	163	41,9	CL-dark overgrowths and replacement textures (metamorphic)
5	93 F2 L1	NAF	13,39	16,1	1424	447	0,32	2548,2	± 2,7	1																	Oscillatory and normal faceted zoned cores and grains (magmatic zircon)
				16,2	96	115	1,24	2538	± 10	2	8624	346	0,85	27,0	1,24	7,97	3,64	1,09	6,43	2,09	24,4	9,21	44,0	10,3	109	27,4	CL-bright sector, simple and unzoned overgrowths and grains (metamorphic)
6	93 J30 A1	NAF	19,58	5,1	179	137	0,79	2703,7	± 5,8	1	6961	1308	0,08	14,8	0,48	6,50	8,53	2,87	31,6	9,79	108	38,9	153	36,3	345	80,3	Oscillatory and normal faceted zoned cores and grains (magmatic zircon)
				5,2	1034	15	0,01	2710,6	± 3,1	2	13722	216	3,88	13,8	1,29	4,73	0,63	0,29	1,89	0,81	11,1	5,41	29,5	9,10	111	33,1	CL-dark overgrowths and replacement textures (metamorphic)
7	93 F2 M3	CGF	23,01	5,2	79	56	0,73	2526	± 13	4	9791	389	0,01	22,6	0,00	0,17	0,96	0,21	4,63	2,13	27,2	11,4	59,2	14,0	141	33,1	CL-bright sector, simple and unzoned overgrowths and grains (metamorphic)
				5,1	205	194	0,98	2551,7	± 7,7	-1	7042	806	0,03	50,9	0,28	4,46	5,29	1,44	17,1	5,23	61,3	23,7	106	23,2	221	51,6	Oscillatory and normal faceted zoned cores and grains (magmatic zircon)
8	93 J31 H2	CGF	23,23	6,1	203	140	0,71	2587,8	± 9,0	-1																	Oscillatory and normal faceted zoned cores and grains (magmatic zircon)
9	93 J31 G3	CGF	26,99	7,1	38	57	1,57	2501	± 28	1	7045	344	0,00	24,4	0,03	0,30	0,90	0,19	4,86	1,89	23,5	8,83	40,0	8,74	83,0	19,7	CL-bright sector, simple and unzoned overgrowths and grains (metamorphic)
				30,1	660	403	0,63	2543,3	± 5,4	-1	8232	697	3,85	57,0	2,69	16,0	7,65	3,62	14,3	4,23	49,4	18,9	88,5	21,0	224	57,9	Oscillatory and normal faceted zoned cores and grains (magmatic zircon)
10	93 J31 D1	CGF	29,76	3,2	25	61	2,56	2520	± 31	0																	CL-bright sector, simple and unzoned overgrowths and grains (metamorphic)
				3,1	443	150	0,35	2555,1	± 5,7	-2	8970	535	0,34	35,0	0,33	2,35	1,82	0,46	7,42	2,76	35,5	14,1	66,6	15,7	164	40,2	Sector zoned, gradual and unzoned overgrowths and grains
11	93 F4 T1	CGF	32,30	7,1	292	186	0,66	2552	± 6,3	0																	Oscillatory and normal faceted zoned cores and grains (magmatic zircon)
				8,2	481	566	1,21	2554,7	± 5,0	1	6429	884	0,47	51,3	1,03	7,79	7,18	2,50	18,2	5,62	61,6	22,7	97,1	21,8	212	49,7	Oscillatory and normal faceted zoned cores and grains (magmatic zircon)
				7,2	137	69	0,52	2531	± 11	0	7686	257	0,02	12,2	0,01	0,17	0,52	0,18	3,14	1,01	12,6	5,37	26,1	6,74	67,7	18,1	CL-bright sector, simple and unzoned overgrowths and grains (metamorphic)
				8,1	84	105	1,29	2496	± 13	1	6372	198	0,03	14,3	0,03	0,47	0,58	0,18	2,43	0,86	11,0	4,53	20,7	5,15	52,1	12,7	CL-bright sector, simple and unzoned overgrowths and grains (metamorphic)
12	93 F4 Q6	CGF	38,61	7,1	39	214	5,69	2515	± 18	0	7906	282	0,00	35,3	0,04	0,94	1,53	0,22	6,16	1,90	20,6	7,07	31,9	7,62	80,7	20,1	CL-bright sector, simple and unzoned overgrowths and grains (metamorphic)
				7,2	218	75	0,35	2678,6	± 7,3	2	7558	1218	0,36	12,2	0,66	5,16	5,01	1,14	19,2	7,44	96,0	37,7	172	38,1	367	83,1	Texturally discordant cores (xenocrystic)
13	95 J1 W3	CGF	39,27	2,2	94	78	0,86	2531,9	± 9,3	1	10104	454	0,02	35,7	0,13	1,18	1,36	0,28	7,45	2,49	29,1	11,8	51,8	13,0	129	29,3	CL-bright sector, simple and unzoned overgrowths and grains (metamorphic)
				9,1	101	118	1,21	2517	± 12	0																	CL-bright sector, simple and unzoned overgrowths and grains (metamorphic)
				9,2	76	79	1,08	2502	± 11	-2	9875	415	0,03	30,3	0,04	0,66	1,07	0,23	6,44	2,38	29,2	10,9	53,6	12,0	123	26,9	CL-bright sector, simple and unzoned overgrowths and grains (metamorphic)
				2,1	138	141	1,06	2554,1	± 7,9	0	7520	947	0,03	35,3	0,22	3,64	4,55	1,41	17,4	5,84	72,1	25,8	113	26,5	249	56,3	Oscillatory and normal faceted zoned cores and grains (magmatic zircon)
				9,3	1495	116	0,08	2537,9	± 2,5	1	11511	781	0,03	10,9	0,03	0,63	1,07	0,48	7,73	3,06	41,6	19,2	101	28,6	330	87,6	CL-dark overgrowths and replacement textures (metamorphic)
14	93 F4 Q1	CGF	41,15	3,2	28	98	3,57	2519	± 24	3	9368	332	0,12	28,6	0,18	0,47	1,62	0,47	4,92	2,19	25,7	9,24	43,1	9,27	92,7	21,9	CL-bright sector, simple and unzoned overgrowths and grains (metamorphic)
				20,1	47	164	3,64	2523	± 16	0	9527	443	0,04	35,2	0,05	1,44	1,29	0,16	8,20	2,89	34,3	13,1	64,6	12,9	129	27,8	CL-bright sector, simple and unzoned overgrowths and grains (metamorphic)
				3,1	575	211	0,38	2725,3	± 4,0	1	8662	1131	0,19	14,6	0,37	1,97	2,54	0,69	13,9	5,38	76,7	31,2	170	39,1	405	98,2	Oscillatory and normal faceted zoned cores and grains (magmatic zircon)
15	93 F4 T10	CGF	44,69	2,1	33	75	2,37	2492	± 27	1	3691	332	0,04	19,5	0,03	0,87	1,21	0,19	4,26	1,63	19,0	5,68	27,5	5,17	48	7,51	CL-bright sector, simple and unzoned overgrowths and grains (metamorphic)
				2,2	347	307	0,91	3258,6	± 5,9	0																	Texturally discordant cores (xenocrystic)
16	93 F1 I18	CGF	48,12	38,1	33	66	2,09	2553	± 21	0																	CL-bright sector, simple and unzoned overgrowths and grains (metamorphic)
				56,1	858	1181	1,42	2547	± 3,5	1	6624	2033	0,14	64,9	0,43	5,98	9,35	2,18	38,7	12,99	150	55,4	241	51,8	495	115	Oscillatory and normal faceted zoned cores and grains (magmatic zircon)
17	95 J1 S3	CGF	48,78	4,2	27	46	1,74	2515	± 22	1	7767	405	0,00	15,7	0,03	0,51	1,19	0,20	5,58	2,22	27,2	10,7	48,6	11,3	109	26,7	CL-bright sector, simple and unzoned overgrowths and grains (metamorphic)
				4,1	63	35	0,58	2737	± 13	1	7214	532	0,05	7,93	0,05	0,61	0,91	0,09	5,61	2,42	32,9	13,9	66,1	15,1	150	36,0	Oscillatory and normal faceted zoned cores and grains (magmatic zircon)
18	93 F1 I11	CGF	52,66	31,1	38	52	1,39	2502	± 19	1																	CL-bright sector, simple and unzoned overgrowths and grains (metamorphic)
				13,2	156	132	0,88	2561,5	± 8,4	0	5954	700	0,03	25,7	0,15	2,39	3,59	1,13	12,9	3,91	44,0	17,3	78,1	18,5	197	47,4	Oscillatory and normal faceted zoned cores and grains (magmatic zircon)
19	93 F3 O1	CGF	53,32	1,1	31	41	1,35	2517	± 20	-1	7251	330	0,01	12,9	0,06	0,71	1,14	0,26	5,02	1,90	23,5	8,85	40,4	9,27	93,2	22,9	CL-bright sector, simple and unzoned overgrowths and grains (metamorphic)
				3,1	31	37	1,24	2497	± 26	-1	7231	231	0,00	12,2	0,03	0,43	0,86	0,19	4,05	1,45	16,7	6,28	28,3	6,35	63,7	15,1	CL-bright sector, simple and unzoned overgrowths and grains (metamorphic)

				28,1	126	94	0,77	2571,7	± 9,6	0	6807	621	0,06	23,8	0,13	1,63	2,41	0,75	9,99	3,45	41,7	16,3	79,1	18,8	196	50,1	Oscillatory and normal faceted zoned cores and grains (magmatic zircon)
20	93 F3 O4	CGF	53,87	16,1	67	117	1,82	2504	± 14	0																	CL-bright sector, simple and unzoned overgrowths and grains (metamorphic)
				17,1	54	89	1,69	2518	± 14	0																	CL-bright sector, simple and unzoned overgrowths and grains (metamorphic)
				3,1	553	286	0,54	2554,3	± 4,1	0																	Oscillatory and normal faceted zoned cores and grains (magmatic zircon)
				7,1	365	171	0,48	2539,1	± 5,1	0																	Oscillatory and normal faceted zoned cores and grains (magmatic zircon)
21	94 D31 M3	SGF	63,50	23,1	41	134	3,34	2537	± 19	0	7055	486	0,01	20,6	0,08	1,33	2,26	0,41	9,01	3,17	35,6	13,1	54,6	11,4	107	25,5	CL-bright sector, simple and unzoned overgrowths and grains (metamorphic)
				20,1	2728	199	0,08	2501,6	± 2,2	1	9064	1581	0,05	13,9	0,02	0,30	0,93	0,09	8,11	4,72	79,6	37,9	219	63,3	750	194	Oscillatory and normal faceted zoned cores and grains (magmatic zircon)
22	93 F9 I1	SGF	70,13	19,1	8	6	0,75	2515	± 41	-1	7418	266	0,02	21,7	0,06	0,91	1,55	0,23	5,43	1,66	19,0	7,35	31,9	6,83	69,2	15,3	CL-bright sector, simple and unzoned overgrowths and grains (metamorphic)
				6,1	220	168	0,79	2570,6	± 6,4	-1	7814	756	0,02	33,7	0,08	0,49	1,67	0,87	10,6	3,56	47,8	19,7	96,4	25,3	274	72,2	Oscillatory and normal faceted zoned cores and grains (magmatic zircon)
23	93 F9 H7	SGF	72,23	5,1	29	23	0,80	2520	± 22	0	7285	334	0,00	15,9	0,02	0,42	0,99	0,19	5,01	1,82	22,2	8,49	39,7	9,14	93,0	23,1	CL-bright sector, simple and unzoned overgrowths and grains (metamorphic)
				5,2	550	88	0,17	2534	± 2,9	1	7869	439	0,30	11,3	0,23	1,54	1,48	0,66	6,63	2,45	28,8	11,2	52,6	12,4	133	33,4	Sector zoned, gradual and unzoned overgrowths and grains
24	93 F6 W2	SGF	77,21	2,1	20	30	1,52	2525	± 33	-1	7259	262	0,00	9,83	0,03	0,65	1,04	0,22	4,89	1,70	19,6	7,17	32,5	7,15	69,9	16,8	CL-bright sector, simple and unzoned overgrowths and grains (metamorphic)
				12,2	395	318	0,83	2558,6	± 6,2	0	6956	679	0,41	30,4	0,29	2,54	2,73	1,06	10,2	3,52	42,9	17,1	85,1	21,1	234	65,1	Oscillatory and normal faceted zoned cores and grains (magmatic zircon)
				12,1	521	184	0,36	2531,3	± 8,4	-1	7517	317	0,01	15,5	0,02	0,32	0,63	0,26	3,68	1,50	19,5	7,96	40,1	10,1	112	30,1	Sector zoned, gradual and unzoned overgrowths and grains
25	93 F9 F8	SGF	77,54	10,2	460	45	0,10	2596,5	± 9,7	2	8843	348	0,02	2,52	0,01	0,07	0,16	0,05	1,76	1,02	17,4	8,87	53,4	14,9	174	51,4	Oscillatory and normal faceted zoned cores and grains (detrital zircon)
				10,1	53	64	1,24	2515	± 13	0	7931	350	0,00	22,5	0,02	0,38	0,99	0,20	5,14	1,92	23,9	9,14	43,1	10,2	103	25,9	CL-bright sector, simple and unzoned overgrowths and grains (metamorphic)
26	YD 50	SGF	79,65	14,2	195	109	0,58	2563,6	± 6,9	-1	8637	635	0,00	7,66	0,02	0,75	2,27	0,38	12,6	4,60	53,2	18,7	77,4	15,2	134	29,0	Oscillatory and normal faceted zoned cores and grains (detrital zircon)
				14,1	92	59	0,66	2517	± 10	0	8586	261	0,00	6,70	0,01	0,37	1,08	0,15	6,40	2,14	22,9	7,44	27,2	5,10	44,0	9,20	CL-bright sector, simple and unzoned overgrowths and grains (metamorphic)
27	YD 42	SGF	84,85	11,1	21	26	1,28	2460	± 26	0	8177	357	0,02	20,5	0,04	0,71	1,11	0,28	6,27	2,14	24,0	9,61	46,5	10,5	107	21,8	CL-bright sector, simple and unzoned overgrowths and grains (metamorphic)
				4,1	458	314	0,71	2542	± 4,3	0	8779	463	0,20	29,8	0,12	1,40	1,82	0,61	8,57	2,64	32,1	12,4	60,2	14,0	148	36,5	Oscillatory and normal faceted zoned cores and grains (magmatic zircon)
28	93 F6 X13	SGF	88,72	4,2	28	29	1,07	2481	± 19	0																	CL-bright sector, simple and unzoned overgrowths and grains (metamorphic)
				4,1	622	194	0,32	2524,2	± 5,2	0																	Oscillatory and normal faceted zoned cores and grains (magmatic zircon)
29	93 F7 Z32	SGF	93,25	21,3	25	47	1,91	2540	± 34	0	6905	282	0,00	22,5	0,03	0,54	1,18	0,30	4,84	1,60	18,9	6,98	32,9	7,63	77,9	19,4	CL-bright sector, simple and unzoned overgrowths and grains (metamorphic)
				21,1	331	82	0,26	2560,3	± 6,8	1	7442	295	0,10	13,7	0,15	1,06	1,21	0,57	4,05	1,47	17,6	7,12	36,5	9,33	108	29,2	Sector zoned, gradual and unzoned grains and overgrowths

Disc. = discordance; * = radiogenic Pb corrected for common Pb; isotopic ratios are percent at 1 sigma; age errors are absolute at 1 sigma.
$^{207}Pb/^{206}Pb$ spot ages on OG1 were within 95% confidence intervals of the reference age.

Table 4: SHRIMP age data for titanite from the Shevaroy Block gneisses

Grain spot	U (ppm)	Th (ppm)	Th/U	^{206}Pb* (ppm)	^{206}Pbc (%)	^{238}U/^{206}Pb		(%)	^{207}Pb/^{206}Pb		(%)	^{238}U/^{206}Pb*		(%)	Pb*		(%)	Pb* age (Ma)		abs.	Disc. (%)
Sample 2: 95 F11 R1, NAF 5.09 km, mount DH02, session 3																					
1,1	7	214	32,5	2,54	8,4	2,302	±	4,5	0,2253	±	1,5	2,51	±	4,6	0,1491	±	6,1	2336	±	105	8
2,1	43	147	3,55	16,8	1,4	2,192	±	3,2	0,1742	±	0,79	2,222	±	3,2	0,1620	±	1,1	2476	±	19	3
3,1	20	183	9,40	8,39	4,9	2,057	±	2,8	0,2000	±	1,5	2,163	±	2,9	0,1560	±	3,3	2412	±	56	-2
4,1	97	198	2,12	36,4	0,5	2,282	±	1,5	0,16755	±	0,53	2,294	±	1,5	0,1628	±	0,66	2485	±	11	7
5,1	169	435	2,65	67,5	0,4	2,154	±	1,3	0,16792	±	0,32	2,163	±	1,3	0,16430	±	0,39	2500,4	±	6,6	2
6,1	180	893	5,14	71,0	0,5	2,173	±	1,3	0,16836	±	0,33	2,184	±	1,3	0,16420	±	0,40	2499,4	±	6,8	3
7,1	26	40	1,57	9,55	3,3	2,370	±	2,6	0,1963	±	1,0	2,452	±	2,7	0,1666	±	2,5	2523	±	42	14
8,1	70	82	1,21	27,1	1,1	2,211	±	1,6	0,17025	±	0,53	2,235	±	1,6	0,1608	±	0,76	2464	±	13	3
9,1	9	14	1,58	3,85	7,7	2,083	±	3,7	0,2235	±	1,3	2,255	±	3,8	0,1545	±	4,6	2397	±	79	1
10,1	156	317	2,11	61,2	0,5	2,183	±	1,3	0,16880	±	0,35	2,195	±	1,3	0,16430	±	0,44	2500,4	±	7,4	3
11,1	49	83	1,75	19,2	1,2	2,195	±	1,8	0,17737	±	0,62	2,221	±	1,8	0,1668	±	0,94	2526	±	16	5
12,1	14	135	9,77	6,48	3,4	1,900	±	4,2	0,1996	±	1,2	1,966	±	4,3	0,1698	±	2,7	2556	±	46	-4
Sample 4: 93 F2 K2, NAF 11.50 km, mount DH02, session 3																					
3,1	45	155	3,57	18,2	1,2	2,114	±	2,0	0,1750	±	0,67	2,139	±	2,0	0,1646	±	1,0	2503	±	16	1
4,1	56	267	4,91	23,2	1,2	2,080	±	1,8	0,17807	±	0,57	2,105	±	1,8	0,1676	±	0,87	2534	±	15	1
5,1	197	683	3,58	78,4	0,4	2,158	±	1,4	0,16830	±	0,38	2,167	±	1,4	0,16464	±	0,46	2503,9	±	7,7	2
6,1	27	174	6,59	11,4	2,0	2,067	±	2,4	0,1839	±	0,82	2,108	±	2,5	0,1664	±	1,5	2522	±	26	1
7,1	84	370	4,54	33,8	0,8	2,144	±	1,6	0,17145	±	0,52	2,162	±	1,6	0,1639	±	0,72	2497	±	12	2
8,1	133	420	3,27	55,2	0,7	2,063	±	1,4	0,1718	±	0,70	2,077	±	1,4	0,1659	±	0,81	2517	±	14	-1
9,1	135	404	3,08	54,9	0,5	2,120	±	1,4	0,16881	±	0,44	2,131	±	1,4	0,16420	±	0,53	2499,4	±	9,0	1
10,1	94	228	2,51	37,7	0,7	2,149	±	1,6	0,16946	±	0,48	2,163	±	1,6	0,1636	±	0,64	2493	±	11	2
Sample 5: 93 F2 L1, NAF 13.39 km, mount DH02, session 3																					
2,1	2	0	0,23	0,91	31	1,48	±	8,9	0,4514	±	2,1	2,15	±	10	0,181	±	24	2661	±	398	8
3,1	29	45	1,63	11,19	2,1	2,188	±	3,4	0,1827	±	0,82	2,236	±	3,4	0,1639	±	1,5	2496	±	25	5
8,1	34	4	0,13	14,89	1,9	1,981	±	2,2	0,1862	±	2,8	2,019	±	2,2	0,1697	±	3,2	2555	±	54	-2
10,1	51	5	0,09	20,93	1,0	2,088	±	1,9	0,1729	±	0,66	2,110	±	1,9	0,1637	±	1,0	2495	±	16	0
11,1	5	1	0,10	1,95	11	2,35	±	7,1	0,2829	±	2,9	2,65	±	7,4	0,185	±	11	2699	±	175	31
14,1	12	16	1,38	4,86	5,5	2,172	±	3,7	0,2140	±	1,3	2,298	±	3,8	0,1650	±	3,6	2508	±	61	8
16,1	3	2	0,55	1,35	13	2,16	±	8,2	0,2945	±	2,5	2,48	±	8,5	0,184	±	10	2693	±	172	23

* = radiogenic Pb corrected for common Pb; abs. = absolute; Disc. = discordance; isotopic ratios are percent at 1 sigma; age errors are absolute at 1 sigma

Table 5: Summation of the age data for zircon from the Shevaroy Block gneisses*

				Igneous zircon age (Ma)				Metamorphic ages (Ma): U-enriched (1-13), undepleted (15-29)				Metamorphic ages (Ma): U-depleted zircon				Metamorphic ages (Ma): titanite			
#	Sample	Zone	D (km)	$^{207}Pb/^{206}Pb$ age (Ma)	± 95% conf.	# analyses	MSWD	$^{207}Pb/^{206}Pb$ age (Ma)	± 95% conf.	# analyses	MSWD	$^{207}Pb/^{206}Pb$ age (Ma)	± 95% conf.	# analyses	MSWD	$^{207}Pb/^{206}Pb$ age (Ma)	± 95% conf.	# analyses	MSWD
1	95 J3 H5	NAF	3.54	2557.3	3.1	12	0.91	2515.1	2.1	14	1.6								
2	93 F11 R1	NAF	5.09	2591.3	4.8	10	1.1	2542.6	3.0	5	2.1					2496	10	12	1.9
3	93 F2 J5	NAF	10.18	2540.4	5.7	13	1.8	2527.9	2.8	10	1.2								
4	93 F2 K2	NAF	11.5	2548.4	2.2	13	1.7	2525.6	5.8	7	2.5					2502.1	6.1	14	1.1
5	93 F2 L1	NAF	13.39	2553.0	3.2	11	1.7					2517.6	7.1	9	1.8	2501	25	7	0.65
6	93 J30 A1	NAF	19.58	2713.4	6.3	8	2.2	2711.7	4.2	7	2.2								
7	93 F2 M3	NAF	23.01	2561.3	3.5	10	1.9					2509.8	8.0	9	1.5				
8	93 J31 H2	CGF	23.23	2569.6	4.4	8	1.2												
9	93 J31 G3	CGF	26.99	2555.7	3.1	14	1.5					2534	11	11	0.95				
10	93 J31 D1	CGF	29.76	2551.4	4.4	19	1.3					2513	26	7	0.32				
11	93 F4 T1	CGF	32.3	2552.4	3.1	14	1.3					2514.4	9.7	18	1.8				
12	93 F4 Q6	CGF	38.61	2554.5	3.8	11	1.6					2525	10	17	1.2				
13	95 J1 W3	CGF	39.27	2556.7	4.8	8	1.9	2539.3	2.0	7	1.5	2520.4	6.9	9	1.0				
14	93 F4 Q1	CGF	41.15									2526	10	9	1.0				
15	93 F4 T10	CGF	44.69	3360[i]	53	12	1.3	2543.6	6.9	4	2.3	2497	18	9	1.4				
16	93 F1 I18	CGF	48.12									2528	11	11	1.3				
17	95 J1 S3	CGF	48.78	2722	10	7	1.9					2517	18	5	0.22				
18	93 F1 I11	CGF	52.66	2568.0	5.1	9	0.71	2546	13.0	5	2.3	2499	21	9	1.1				
19	93 F3 O1	CGF	53.32					2548.1	5.7	11	1.8	2495	13	10	0.94				
20	93 F3 O4	CGF	53.87	2548.9	5.1	10	2.2					2519	12	8	1.5				
21	94 D31 M3	SGF	63.5									2498	18	13	2.0				
22	93 F9 I1	SGF	70.13									2501.0	5.0	9	1.7				
23	93 F9 H7	SGF	72.23	2559.3	5.3	3	0.18	2540.8	4.7	7	2.2	2503	18	9	2.1				
24	93 F6 W2	SGF	77.21	2567.9	5.3	8	1.5	2542.5	4.4	8	1.9	2500	13	8	0.4				
25	93 F9 F8	SGF	77.54									2515	10	11	1.3				
26	YD 50	SGF	79.65									2516.3	4.3	21	1.2				
27	YD 42	SGF	84.85	2544.1	5.2	14	2.1					2500	19	9	2.1				
28	93 F6 X13	SGF	88.72					2531.9	8.8	7	2.1	2508	15	11	1.2				
29	93 F7 Z32	SGF	93.25	2566.1	5.1	8	1.3	2537.6	8.1	4	0.77	2506	22	8	1.2				

*Quoted ages are weighted means of pooled analyses and from the is the mean square weighted deviation (MSWD); scattered age data are not shown; i = Model 1 upper intercept age; isotopic ratios are percent at 1 sigma

Blank = unable to get a weighted mean age from the data.